



TECHNISCHE
UNIVERSITÄT
WIEN

Vienna University of Technology

Nanofiber-based optical interface for single dye molecules in organic nanocrystals

DISSERTATION

zur Erlangung des akademischen Grades

Doktor der Naturwissenschaften

eingereicht von

David C. Papencordt

Matrikelnummer 1029618

Juchgasse 20/24, 1030 Wien

an der

Fakultät für Physik der Technischen Universität Wien

Betreuung: Prof. Dr. Arno Rauschenbeutel, E141 – Atominstitut

Diese Dissertation haben begutachtet:

(Prof. Dr. Arno
Rauschenbeutel)

(Prof. Dr. Markus Arndt)

Wien, 23.06.2015

(David C. Papencordt)



TECHNISCHE
UNIVERSITÄT
WIEN

Vienna University of Technology

Nanofiber-based optical interface for single dye molecules in organic nanocrystals

DISSERTATION

submitted in partial fulfillment of the requirements for the degree of

Doktor der Naturwissenschaften

by

David C. Papencordt

Registration Number 1029618

Juchgasse 20/24, 1030 Wien

to the Faculty of Physics
at the Vienna University of Technology

Advisor: Prof. Dr. Arno Rauschenbeutel, E141 – Atominstitut

The dissertation has been reviewed by:

(Prof. Dr. Arno
Rauschenbeutel)

(Prof. Dr. Markus Arndt)

Wien, 23.06.2015

(David C. Papencordt)

Abstract

In this thesis, the manufacturing and use of dye-doped organic crystals for nanofiber-based single molecule spectroscopy (SMS) at cryogenic temperatures is studied. Optical nanofibers with sub-wavelength diameters provide a high intensity evanescent field, which allows high excitation and emission collection efficiencies for molecules close to the fiber surface.

The nanofibers used for spectroscopic measurements in this work are produced from standard optical glass fibers via flame pulling, resulting in a sub-wavelength diameter waist of a tapered optical fiber (TOF). The light transmission characteristics of such a nanofiber depend critically on the geometrical shape of the TOF transitions: as long as the fiber taper is kept shallow, losses due to coupling from the fundamental to higher order modes are negligible and the transmission properties of the fiber are maintained. When an external object is interfaced with the TOF, the size has to be small enough that the evanescent field suffers only small disturbances and the light guiding abilities of the optical fiber are maintained.

For SMS a stable environment of the molecule is essential. Since they are highly ordered, crystals offer the most favorable host system. They can be manufactured by various methods such as sublimation or growth from solution. These methods are employed here for terrylene molecules in a p-terphenyl crystal to create small crystals with a low dopant concentration. The resulting samples are examined spectrally and with the help of a scanning electron microscope for their applicability with TOFs. After the manufacturing and deposition of proper sized doped crystals on the TOF, the samples are cooled down in a liquid helium bath cryostat to a temperature of 4.4 K, where the phonon transitions within the sample are highly reduced. All further molecule spectroscopy experiments are conducted at this temperature.

The fluorescence of the molecular ensemble is investigated and the vibronic transitions of terrylene are revealed by fluorescence excitation measurements. To address a single molecule, it has to be distinguished from the ensemble. The crystal provides some inhomogeneous broadening which allows to spectrally select a single molecule using a narrowband laser. A single molecule is clearly identified by means of its fluorescence autocorrelation function and measurements of the spectral stability show, if the molecule is suited for long time measurements. Stable molecules are investigated by fluorescence spectroscopy and fluorescence intensity autocorrelation measurements. This allows a further evaluation of the manufactured crystal samples and their usability for SMS with a TOF.

Kurzfassung

In dieser Arbeit wird die Herstellung und Verwendung von Farbstoff-dotierten organischen Kristallen für die nanofaserbasierte Einzelmolekülspektroskopie (*engl. single molecule spectroscopy*, SMS) bei kryogenen Temperaturen untersucht. Optische Nanofasern mit Durchmessern unterhalb der Wellenlänge des geführten Lichts weisen ein evaneszentes Feld hoher Intensität auf, welches hohe Anregungs- und Fluoreszenzsammeleffizienzen für Moleküle nahe der Faseroberfläche ermöglicht.

Die Nanofasern, die für die spektroskopischen Messungen in dieser Arbeit Verwendung finden, werden mittels Erhitzen und Ziehen aus optischen Glasfasern hergestellt. Die so erhaltenen verjüngten optischen Fasern (*engl. tapered optical fiber*, TOF) haben Durchmesser unterhalb der Wellenlänge des geführten Lichts. Die Lichtföhrungseigenschaften solcher Nanofasern hängen kritisch von der geometrischen Form der Verjüngungsübergänge der TOF ab: solange die Verjüngung mit einem flachen Winkel erfolgt sind Föhrungsverluste aufgrund von Kopplungen zwischen der Grundmode und höheren Moden vernachlässigbar und die Transmissionseigenschaften der Faser bleiben erhalten. Wenn ein externes Objekt an die TOF gekoppelt wird, muss dessen Größe klein genug sein, damit das evaneszente Feld nur kleine Störungen erfährt und die lichtföhrenden Eigenschaften der optischen Faser erhalten bleiben.

Eine stabile Umgebung ist bei SMS für das Molekül wesentlich. Kristalle bieten hierbei das präferierte Wirtssystem da sie eine hochgradig geordnete Struktur besitzen. Sie können auf verschieden Arten, wie Sublimation oder Wachstum aus übersättigter Lösung, hergestellt werden. Beide Methoden werden in dieser Arbeit für Terrylen-Moleküle in einem p-Terphenyl-Kristall angewandt, um möglichst kleine Kristalle mit niedriger Dotierung herzustellen. Die hergestellten Proben werden spektral und mit der Hilfe eines Rasterelektronenmikroskopes für die Eignung zur Verwendung mit TOFs untersucht. Nach der Herstellung und Deponierung von Kristallen mit entsprechender Größe auf der TOF werden die Proben in einem Flüssig-Helium-Badkryostaten auf Temperaturen von 4.4 K geköhlt, bei der die Phononenübergänge in der Probe stark reduziert sind. Alle weiteren Molekülspektroskopie-Experimente werden bei dieser Temperatur durchgeführt.

Die Fluoreszenz des molekularen Ensembles und die vibronischen Übergänge von Terrylen werden mittels Fluoreszenzanregungsmessungen untersucht. Um mit einem einzelnen Molekül zu interagieren muss es vom Ensemble unterscheidbar sein. Die durch den Kristall bewirkte inhomogene Verbreiterung ermöglicht es, einzelne Moleküle mit einem schmalbandigen Laser spektral auszuwählen. Ein einzelnes Molekül kann einwandfrei mittels seiner Fluoreszenz-Autokorrelationsfunktion identifiziert werden und Messungen der spektralen Stabilität zeigen, ob das Molekül für Langzeit-Messungen geeignet ist. Stabile Moleküle werden mit Hilfe von

Fluoreszenzspektroskopie und Fluoreszenz-Autokorrelationsmessungen untersucht. Dies erlaubt eine weitere Beurteilung der hergestellten Kristallproben und ihrer Nutzung für SMS mittels einer TOF.

Contents

1	Introduction	1
2	Spectroscopy with tapered optical fibers	5
2.1	Tapered optical fibers	6
2.1.1	Field distribution	7
2.1.2	Fabrication and quantification of tapered optical fibers	10
2.1.3	Light coupling to external objects	12
3	Spectroscopy of single organic dye molecules – Theoretical background	19
3.1	Optical properties of organic dye molecules	19
3.1.1	Transitions and energy levels in molecules	20
3.1.2	Transition probabilities in molecules	24
3.1.3	Optical Bloch equations	28
3.1.4	Line shape broadening effects	30
3.2	Spectroscopy of single molecules	33
3.2.1	Spatial and spectral selection	33
3.2.2	Further requirements for single molecule spectroscopy	35
3.2.3	Properties of a molecule as a single photon source	36
3.3	Sample systems	38
3.3.1	Terrylene as a fluorescent dopant	39
3.3.2	p-Terphenyl as a single crystal host	40
4	Experimental setup	47
4.1	Optical setup	47
4.1.1	Excitation path	47
4.1.2	Fluorescence path	49
4.2	Cryostat	50
5	Manufacturing of dye-doped crystals	55
5.1	Cold-finger sublimation	56
5.1.1	Sublimation cell	56
5.1.2	Preparing the molecule raw material	57
5.1.3	Sublimation of doped crystals on the TOF	57

5.1.4	Deposition of downsized sublimated crystals	63
5.2	Crystal growth from oversaturated solution	65
5.2.1	Different oversaturations and very low concentrations	66
5.2.2	Deposition of crystals from solution via drop-touch method	67
5.2.3	Enhanced crystal growth via fast precipitation	68
6	Spectroscopy of molecules in solid state at low temperatures	75
6.1	Ensemble spectroscopy	77
6.1.1	Identification of peaks	77
6.1.2	Anomalous peaks	80
6.1.3	Fluorescence excitation spectroscopy	82
6.1.4	Statistical finestructure	84
6.2	Single molecule experiments	85
6.2.1	Finding a single molecule in a haystack	85
6.2.2	Autocorrelation measurements	94
6.2.3	Further saturation measurements	99
7	Summary and Outlook	103
A	Light propagation in optical fibers	107
A.1	Linearly polarized modes	112
	Bibliography	115



Introduction

Over the last century, the interaction of light and matter has been one of the essential research topics in quantum physics, leading to numerous advancements in the theoretical understanding of the nature of light as well as practical technical applications. With the rising ability to control light-matter interactions even for single quantum systems, new areas of research like quantum information are generated [1]. In 2012, the Nobel prize in physics was awarded to Serge Haroche and David Wineland for their efforts in manipulating quantum systems.

During the last decades, various techniques for the controlled manipulation and detection of single quantum systems like atoms, molecules or nanocrystals have been invented and optimized: the imaging of single atoms or molecules on surfaces is possible since the invention of the scanning tunneling microscope [2] and the atomic force microscope [3] and allows sub-nanometer resolution in real space. The first optical detection of single particles was realized by storing atomic ions in an electromagnetic trap [4] and the first spectroscopical detection of a single molecule within a solid was performed by W. E. Moerner and L. Kador in 1989 by measuring the absorption signal of a single pentacene molecule [5]. This experiment was conducted at liquid-helium temperatures and was based on frequency/Stark modulation techniques. Due to the ratio of an unfavorable molecular cross section to the beam cross section, the signal-to-noise ratio was limited. Only one year later, M. Orrit and J. Bernard introduced fluorescence excitation spectroscopy as a new method for single molecule spectroscopy (SMS) [6]. Up to now, it is the preferred method due to its superior sensitivity.

Since then, SMS has been performed for many different types of molecules [7] and different environments like in solids, on surfaces or in liquids. Single molecules in solids can be used as sensitive sensors for the investigation of their local environment. Furthermore, single molecules embedded in organic crystals are well suited to take the role as an efficient single quantum emitter, since they offer a higher emitter density for a typical sample size and concentration compared to quantum dots or color centers in diamond nanocrystals [8]. Crystal embedded molecules provide a high photostability as well as a relatively high spectral stability. Their resonance frequency can be tuned by applying a static electric field and using the Stark effect [9].

The main challenge for SMS is to separate a very small signal from the noise produced by the molecule's surrounding and the optical system. To overcome this problem, many approaches were made using different techniques like confocal microscopy [10], total internal reflection microscopy [11, 12] or near-field scanning optical microscopy [13]. In 2014, the Nobel Prize in Chemistry was awarded to Eric Bertzig, Stefan W. Hell and William E. Moerner for their development of super-resolved fluorescence microscopy, which is directly connected to single molecule detection.

In recent years, optical nanofibers have proven their ability to work as an efficient interface between light and matter. They can be realized from standard optical glass fibers as the waist of a tapered optical fiber (TOF). Although a TOF has a subwavelength-diameter which leads to a strong radial confinement of the guided light field and a pronounced evanescent field surrounding the nanofiber, the light is still guided almost without losses like by a standard optical glass fiber. Due to the high evanescent field, effective light-matter coupling can be achieved by bringing a particle close to the surface of the nanofiber. In the recent years TOFs have been successfully used as optical sensors [14–16], for cold atom physics [17–19], as couplers for whispering-gallery-mode microresonators [20, 21] or nonlinear optics [22, 23]. When used for surface absorption spectroscopy, TOFs showed that they offer a sensitivity, which is orders of magnitude higher compared to free-beam absorption spectroscopy [24]. Single quantum dots [25] and single nanodiamonds [26] have already been coupled to a TOF.

In this group, spectroscopy of dye-doped organic crystals attached to the surface of the nanofiber was already performed. But due to low crystal quality, the single-molecule level could not be reached. Furthermore, the light-guiding abilities of a TOF were lost due to a large crystal size. Sustaining the transmission properties of a TOF would allow for measurements in transmission, which is a requirement e. g. for the implementation of single photon transistors [27].

In this thesis, TOF-based surface spectroscopy is extended to the single molecule level while sustaining the transmission properties of the TOF. The coupling efficiency of the TOF as a fiber-coupled interface depends on the intensity of the evanescent field TOF. Therefore, in chapter 2 the light propagation in a TOF is studied and the field distribution of the evanescent field is derived from Maxwell's equation in dependence of the radius of the TOF. As an organic sample system, terrylene-doped p-terphenyl crystals are used. The theoretical background of the general properties of crystal embedded single organic dye molecules and the special characteristics of the used sample system are studied in chapter 3. The optical setup and the cryostat to cool down TOFs with crystal samples to cryogenic temperatures is explained in chapter 4. To overcome problems originating from large crystals and low crystal quality, different methods like sublimation of doped crystals directly on the TOF or crystal growth from an oversaturated solution are investigated (chapter 5). In order to investigate the quality and the size of the manufactured crystals, the fluorescence spectra and the transmitted power are recorded during the deposition on the TOF. The shape of the crystals is examined with a scanning electron microscope. Small monocrystals produced from an oversaturated solution via fast precipitation allow a suitable light transmission through the TOF and are used for TOF-based spectroscopy at cryogenic temperatures. In chapter 6 several single terrylene molecules in different crystal samples are identified via their fluorescence intensity autocorrelation function. For spectrally stable molecules, the saturation intensity and the linewidth is determined. For some molecules, the latter is already

close to the lifetime-limited value. Finally, chapter 7 gives an overview of the whole work and the results.

Spectroscopy with tapered optical fibers

Since the development of optical glass fibers with very low losses in the 70s of the twentieth century [28], the range of applications has enormously grown. Beside the telecommunications industry, where optical fibers are used as a transmitting medium for grid-bounded ways of telecommunication, optical glass fibers are, e. g., also used in medical science (endoscopy) [29] and measurement instrumentation (spectroscopy). Last but not least, specially doped glass fibers offer the possibility to build very robust and compact fiber lasers with high beam quality and efficiency [30]. Most optical fibers are of circular geometry and consist of a core and a cladding, cf. fig. 2.1(a). Additionally, a surrounding acrylate coating or jacket is protecting against scratching, which would affect the mechanical stability of the fiber negatively. As the base material for

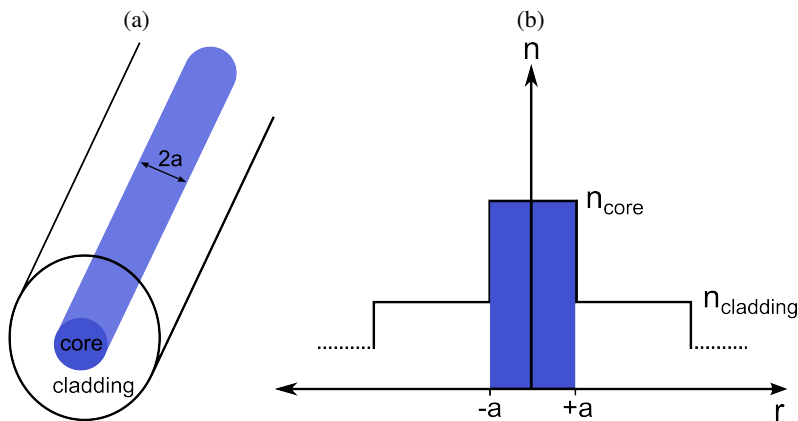


Figure 2.1: (a) Schematic structure of a step-index-fiber. (b) Refractive index profile of a step-index-fiber. For details see text.

core and cladding, mainly fused silica (SiO_2) is used. To induce a slight variation between the refractive indices of core and cladding, either one or the other is doped with a few percent of appropriate ions like germanium or fluorine. Step-index fibers, as used in this work, evince an abrupt drop of the refractive index at the border of core and cladding, cf. fig. 2.1(b). The radius a of the core depends on the wavelength the fiber is designed for and is usually a few micrometers. Typically, the outer diameter of the cladding is $125\text{ }\mu\text{m}$ and the additional coating has $245\text{ }\mu\text{m}$.

Although standard optical fibers proved their importance for many applications, they are not suited for directly coupling matter with light and simultaneously assuring the light guiding abilities of the fiber: The contact between the light within the core of the fiber and the surrounding medium outside the fiber is effectively hindered by the fiber's cladding. Although the evanescent field extends into the cladding, the cladding's thickness prevents contact with the environment. To interface the guided light inside a fiber with matter outside the fiber, one has to access the evanescent field of the guided mode. This can be achieved by so-called nanofibers. Such optical fibers are usually produced by heating and stretching of a standard optical glass fiber, e. g. via flame pulling. This results in a tapered optical fiber (TOF) with a characteristic shape and a sub-wavelength diameter waist. In a TOF, a part of the guided mode of the light spreads out into the environment. Nevertheless, the light guiding abilities of the fiber are still intact and the strong confinement of the mode, which results in high intensities of the evanescent field, allows to use a TOF as an effective way for to couple light with matter [24]. To make use of the light guiding and matter-coupling abilities of a TOF, the theory of light propagation in optical fibers has to be considered. Starting from the Maxwell equations, the derivation of the characteristic eigenvalue equation is presented in app. A. Its solutions lead to the guided modes in an optical fiber. Based on this, the properties of TOFs, including their field distribution and the prerequisites for their fabrication are discussed in this chapter. Taking into account the light guiding properties of a TOF, the coupling of light inside the TOF to objects on the fiber surface is shortly introduced.

2.1 Tapered optical fibers

After a TOF is produced from a standard optical fiber via tapering to a sub-wavelength diameter, the light is guided by total internal reflection between the surrounding medium and the core, which consists of the old cladding of the fiber (the influence of the old core is negligible). The deviation of the TOF's geometry from the untapered optical fiber leads to a change in the behavior of the guided modes. Fig. 2.2 shows the three different parts of a TOF and the corresponding change in the intensity distribution of the guided light: the unprocessed fiber at the beginning is narrowed down in the taper transition to the desired sub-wavelength diameter of the waist. Since the refractive index profile of the fiber is changing in the transition part, the guided light is transformed from the core-guided mode of the unprocessed fiber to the cladding-guided mode of the nanofiber. A TOF is symmetric, and therefore the former mode transition in the down-taper is reversed in the up-taper, following the waist to the unprocessed fiber. The mode conversion process is kept adiabatic, by keeping the angle of the taper transition shallow (not exceeding a few milliradians) [31], i. e. no coupling between the fundamental mode and higher order modes will occur. This is a prerequisite for efficiently coupling light into and out of the nanofiber. Within the waist of a TOF, the guided light is strongly confined within the core but also exhibits

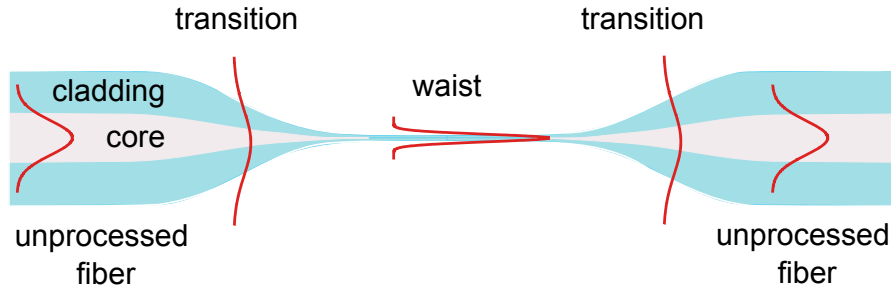


Figure 2.2: Schematic of the shape of a tapered optical fiber and the change of the intensity distribution.

an evanescent field outside the core and a strong surface intensity [32]. Matter on the surface of the waist can then interact with this strong light field. A wide range of applications makes use of this efficient interaction [33].

2.1.1 Field distribution

For interfacing the evanescent light of a TOF with matter on the surface of the waist, the field distribution of the light mode has to be known. It allows the production of nanofibers with the correct dimensions for a maximal light-matter interaction as well as the understanding of the coupling. Unlike standard optical fibers, where the transcendental eqn. A.21 can be simplified due the small differences of the refractive indices of core and cladding (cf. eqn. A.32), this approximation is not valid for nanofibers: the refractive index contrast between the original cladding, which acts as the nanofiber's core, and the surrounding medium as the new cladding is much too high ($n_{\text{core}}/n_{\text{cladding}} \approx n_{\text{core}}$). To calculate the propagation constant of a TOF and hence the field distribution, the full transcendental equation A.21 has to be considered. The small diameter of a nanofiber and the high refractive index contrast lead to a significant difference in field distributions compared to standard optical fibers [34]. It is useful to distinguish between two different polarization states of the guided light.

Quasi-linear polarization

In the case of linear polarization, the cylindrical symmetry of the problem is broken and a strong azimuthal dependence of the field, especially outside the fiber is observed. Fig. 2.3 shows two plots for the radial dependence of the intensity of the electric field of the HE_{11} mode for linear polarization parallel to the x-axis. Along the x-axis the intensity of the electrical field exhibits a discontinuity on the fiber surface, which results in a strong increase of the field, cf. fig. 2.3(a). On the other hand, along the y-axis, i. e. perpendicular to the polarization of the light, no discontinuity occurs at the fiber surface 2.3(b). The difference in the surface intensity for both directions is to emphasize: In the polarization direction, the intensity is almost five times higher than perpendicular to it. The intensity inside the fiber exhibits a bell shape, but with a faster decrease towards the fiber surface in y-direction. Outside the fiber, the decrease of the light intensity is faster in x-direction. It is notable, that the intensity on the fiber surface parallel to the

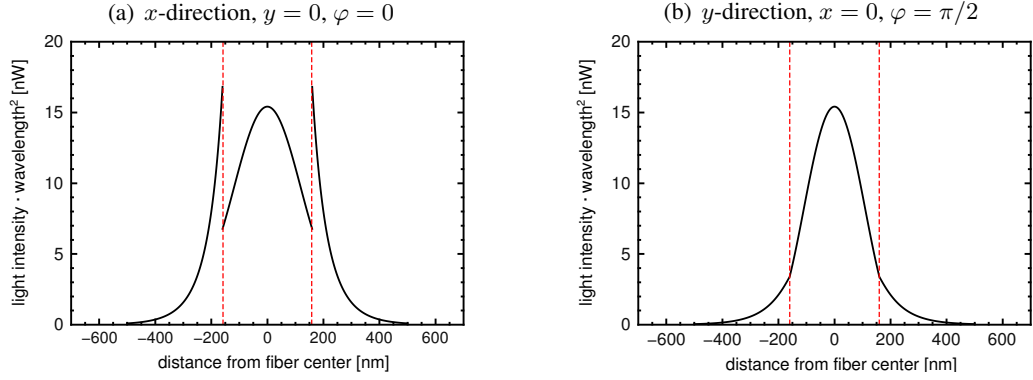


Figure 2.3: Plots of the radial dependence of the intensity of the electric field $|E|^2 = |E_r|^2 + |E_\phi|^2 + |E_z|^2$ in the fundamental mode HE_{11} with quasi-linear polarization. Parameters used: guided power = 5 nW, $\lambda = 578$ nm, $n_{\text{core}} = 1.45881$, $n_{\text{cladding}} = 1$ and $a = 160$ nm (marked with red dashed lines). Plot (a) shows the light intensity as a function of x at $y = 0$ with a polarization parallel to the x -axis ($\varphi = 0$) and (b) as a function of y at $x = 0$ with a polarization parallel to the x -axis ($\varphi = \pi/2$)

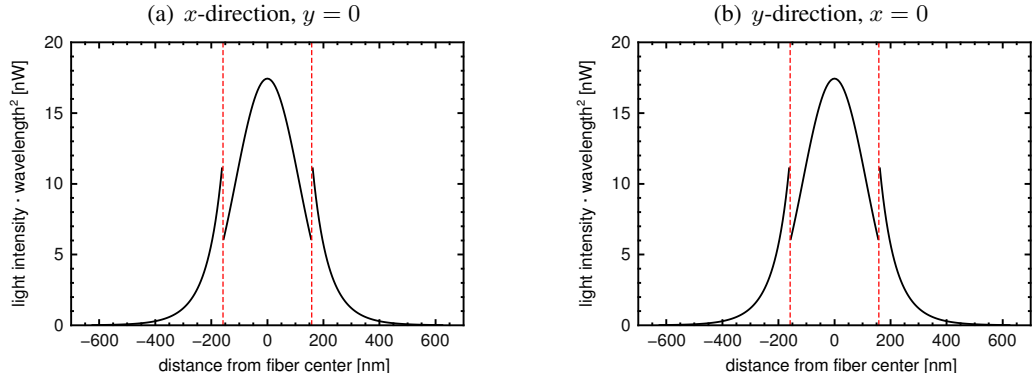


Figure 2.4: Plots of the radial dependence of the intensity of the electric field $|E|^2 = |E_r|^2 + |E_\phi|^2 + |E_z|^2$ in the fundamental mode HE_{11} with circular polarization. The parameters used are the same as for fig. 2.4. Plot (a) shows the intensity as a function of x at $y = 0$ and (b) as a function of y at $x = 0$.

polarization direction, exceeds the one within the fiber and also the one with circular polarization for the same parameters.

Circular polarization

Unpolarized light, such as white light of a halogen lamp leads to the same intensity distribution as circular polarization [34]. Fig. 2.4 shows two plots with the radial dependence of the intensity of the electric field $I = \frac{1}{2}\epsilon_0 c_0 |E|^2$ of the HE_{11} mode for circular polarization for the parameters

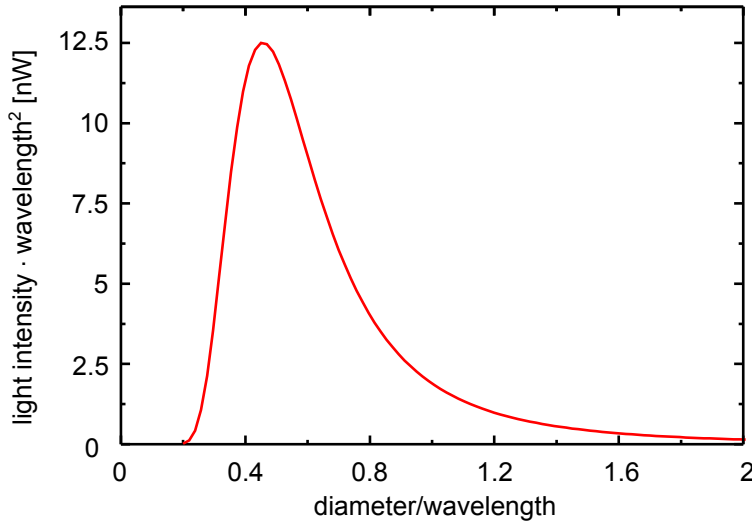


Figure 2.5: Plot of the radius dependency of the surface intensity of the electric field $|E|^2$ for the fundamental mode HE_{11} with circular polarization. It is calculated for a guided power of 5 nW and the parameters already used for the calculation of fig. 2.4.

shown. The light intensity is azimuthally independent, and therefore cylindrically symmetric. At the fiber surface, at $r = 160$ nm, a discontinuity can be observed, which results in a strong increase of the light intensity on the fiber surface. It is caused by the boundary conditions and the high contrast between the refractive indices of core and vacuum/air. Outside the TOF, the intensity of the field decays within a distance that is on the order of the wavelength.

However, since the fibers used in this work are not ideal, they can show birefringence due to external influences. This results in polarization mode dispersion and the polarization of the guided light is a mixture of circular (elliptical) and linear polarized parts. The yielding intensity distribution varies between the ones presented here.

For sensitive surface spectroscopy, the intensity on the fiber surface has to be maximized. Fig. 2.5 shows the surface intensity as a function of the diameter in units of the wavelength for the total electric field. It can be seen that the surface intensity strongly depends on the diameter of the TOF. When the diameter is increased, the light is more and more concentrated in the core and the intensity on the surface vanishes. When the diameter decreases, the intensity reaches a maximum at $d_{max} = 0.469 \cdot \lambda$. When the diameter decreases further and becomes much smaller than the wavelength of the guided light, the confinement of the mode to the core strongly diminishes and the mode spreads out to the surrounding medium, thus decreasing the surface intensity.

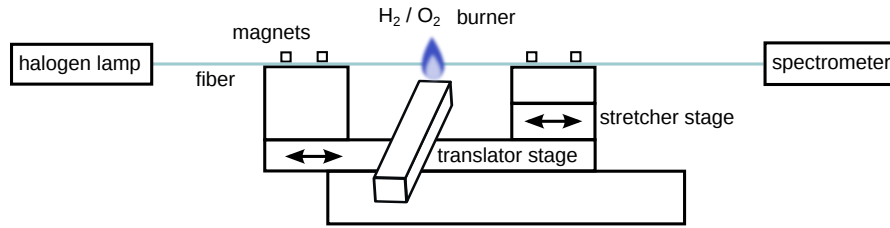


Figure 2.6: Schematic of the fiber pulling rig. A highly pure hydrogen/oxygen flame heats a standard glass fiber while it is stretched and moved by two stages. To control the transmission properties during the pulling process, a halogen lamp and a spectrometer is connected to the fiber.

2.1.2 Fabrication and quantification of tapered optical fibers

It has been shown that the propagation properties of a TOF strongly depend on the applied geometry during the pulling process [35]. Therefore, all fibers used for experiments in this work have been produced by a computer-controlled pulling rig, built by F. Warken [36]. This allows the control of the diameter of all parts of the TOF and ensures a high reproducibility. In fig. 2.6 a schematic of the fiber pulling rig can be seen. It is based on two stages that allow to stretch and move the fiber with respect to the flame, thus creating a variable hot zone, according to the "flame-brush" technique [37]. To achieve high transmission rates through the TOF it is essential to undertake the whole process in the dust-free environment of a laminar flow box. First, a standard optical glass fiber (Fibercore SM450) is stripped of the protective acrylate coating and carefully cleaned with purified acetone to remove all remainings of the coating and possible contaminations deposited during handling. After pulling, the fiber is clamped on an iron holder by two magnets 2.7(a). Mechanical damages are avoided by placing the magnets on the unstripped part of the fiber. To be held in place, the holder needs v-grooves that match the size of the diameter of the unstripped fiber. Therefore, the part which is stripped off has to be as short as possible (which is precisely 21 mm for this particular holder). The clean fiber is positioned and fixed by magnets to the v-grooves on top of the stretcher stage. The stationary hydrogen/oxygen burner offers an electronically controlled laminar gas flow and heats the glass fiber beyond its softening point at a temperature of about 1500 °C on a length of 1 mm. While the translator stage is moving the fiber back and forth with respect to the flame, the stretcher stage is elongating the fiber causing a reduction in the fiber diameter due to volume conservation. The movement of both stages is computer controlled and their trajectories allow a full control over the shape of the TOF. The calculation of the trajectories follows an analytic algorithm presented in [36]. By manually moving the stretcher stage after the fiber is pulled, it is possible to stretch the TOF to a desired tension. The clamping of the TOF on the holder has to resist the later cooling process to cryogenic temperatures. Therefore a pure mechanic mount in terms of two magnets and an iron holder was constructed, [38] cf. fig. 2.7. When positioning the magnets, care has to be taken to clamp the tapered fiber at a part, where some coating is left and to exactly match the v-groove. Once the TOF is clamped on the iron holder, it can be taken out of the pulling rig and transported to the experimental setup for further use.

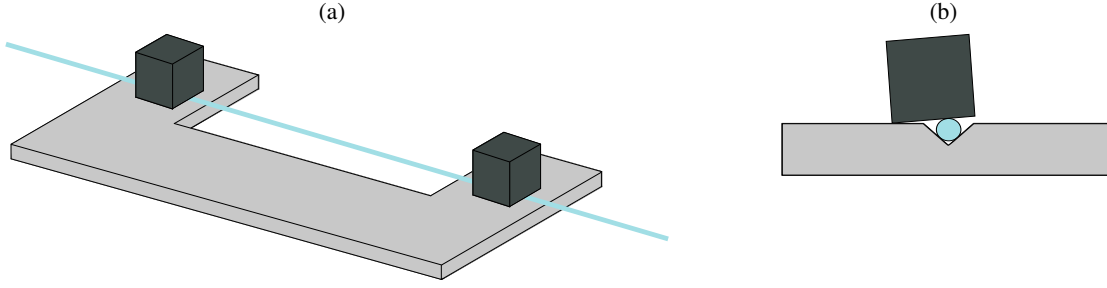


Figure 2.7: (a) Schematic of the iron fiber holder. (b) Magnets are fixing the fiber within a v-groove.

The TOFs used in this work have been designed to offer a high transmission for the wavelength ranges 575 to 582 nm (excitation wavelengths) and 620 to 650 nm (fluorescence wavelengths). Since the power loss from the fundamental mode strongly depends on the taper shape and the used wavelength, the taper transition consists of three sections with different angles, cf. fig. 2.8. The coupling between the modes HE_{11} and HE_{12} is predominant and increases strongly when their propagation constants β_1 and β_2 approach each other. The energy exchange between the two modes occurs periodically on the length scale Δl of their beat length $\Delta l = 2\pi/(\beta_1 - \beta_2)$. To keep the coupling between these two modes at a minimum, the local taper angle Ω has to be small at every position z along the taper, compared to the ratio of radius r and beat length [39]

$$\Omega(z) < \frac{r(z)}{\Delta l(z)} = \frac{r(z)}{2\pi}(\beta_1(z) - \beta_2(z)) \quad (2.1)$$

It is sufficient, to keep the taper angle shallow only for the region of the taper transition, where the two propagation constants merge [36]. For the used wavelengths and fiber type, the mode HE_{11} passes from the core to the cladding and the difference between both propagation constants becomes smallest at $r = 31 \mu\text{m}$. Therefore, for the region between $r_2 = 42 \mu\text{m}$ and $r_3 = 20 \mu\text{m}$ a rather flat local taper angle $\Omega_2 = 2 \text{ mrad}$ has been chosen. To minimize the overall length of the TOF, the adjacent taper angles are steeper with $\Omega_1 = 3 \text{ mrad}$ and $\Omega_3 = 5 \text{ mrad}$. Fig. 2.8 shows the calculated shape of the fiber profile according the trajectories used by the pulling machine for the pulling process. It has been found empirically, that for manufacturing a homogeneous waist, the pulling speed¹ v_f has to be lower than the relative velocity of the fiber with respect to the burner [36]. This limits the local taper angles $\Omega_i(r)$ to $0.30 \text{ mrad}/\mu\text{m} \cdot r$. Especially for small taper radii, this relative velocity cannot be redeemed anymore, leading to an exponential shape for radii smaller $r \approx 17 \mu\text{m}$. The inset in fig. 2.8 shows a magnification of the 3 mm long waist of the tapered fiber. The compliance between the calculated and the actual shape of a TOF produced in this way has been verified by a measurement of the local radii with the help of a scanning electron microscope by A. Stiebeiner [35] and C. Wuttke.

The length of the waist of the TOFs used in this work is 3 mm and the diameter is 320 nm resulting in a total TOF length of 63 mm. The transmission spectrum of a TOF pulled with

¹Defined by the speed $v_f/2$ the translator and the stretcher stage are each pulling the fiber.

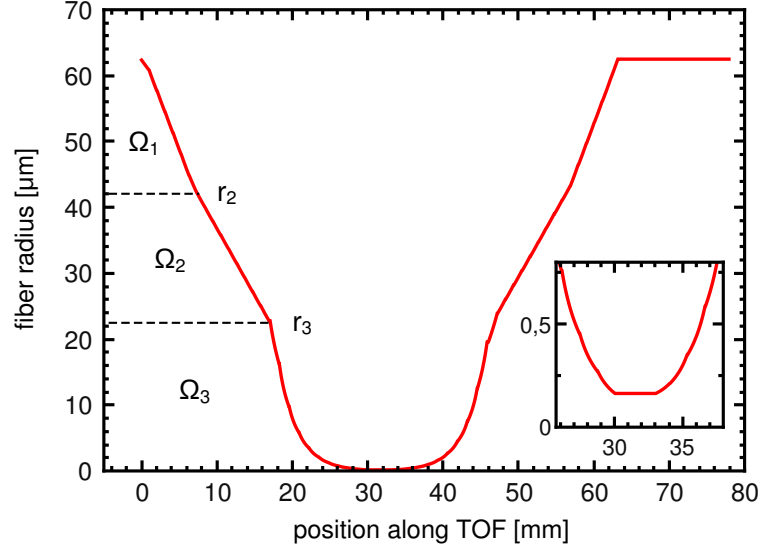


Figure 2.8: Calculated radius profile of the TOF used in this work, the local taper angles are $\Omega_1 = 3$ mrad, $\Omega_2 = 2$ mrad and $\Omega_3 = 5$ mrad starting at radii of $r_2 = 42$ μm and $r_3 = 22$ μm . The inset shows a magnification of the waist with 3 mm length.

these parameters out of a standard glass fiber (Fibercore SM450) was recorded with a halogen lamp (Avantes AvaLight-Hal-S) and a spectrometer (Avantes AvaSpec-2048-2) during the pulling process, it can be seen in fig. 2.9 and has been normalized to the transmission spectrum of the untapered fiber. The transmission is at about 95 % for all wavelengths above 570 nm. Below that wavelength, a drop to 80 % can be observed.

2.1.3 Light coupling to external objects

The light guiding abilities of a nanofiber and the pronounced evanescent field outside the TOF enable their use for spectroscopic purposes. The field shows a maximum directly at the fiber surface yielding high surface intensities. Moreover, the waist of a TOF can be several centimeters long. Thus, surface-deposited molecules or particles can be spectroscopically investigated with a very high sensitivity.

The absorbance $\eta(\lambda)$ of a sample, consisting of a number N molecules on the surface, is defined as the negative decadic logarithm of the power loss after traveling through the sample:

$$\eta(\lambda) = -\log \left(\frac{P_{\text{sig}}(\lambda)}{P_{\text{ref}}(\lambda)} \right) \approx \frac{P_{\text{abs}}(\lambda)}{\ln(10)P_{\text{ref}}(\lambda)} \quad (2.2)$$

The power loss is computed by comparing the transmitted power with the sample present, $P_{\text{sig}}(\lambda)$, and without the sample present, $P_{\text{ref}}(\lambda)$, respectively. Here, only the limit of weak absorption is considered, where the guided power of the excitation light is equal to P_{ref} at all positions along the fiber. Thus, the total absorbed power is $P_{\text{abs}}(\lambda) = P_{\text{ref}}(\lambda) - P_{\text{sig}}(\lambda) \ll P_{\text{ref}}(\lambda)$

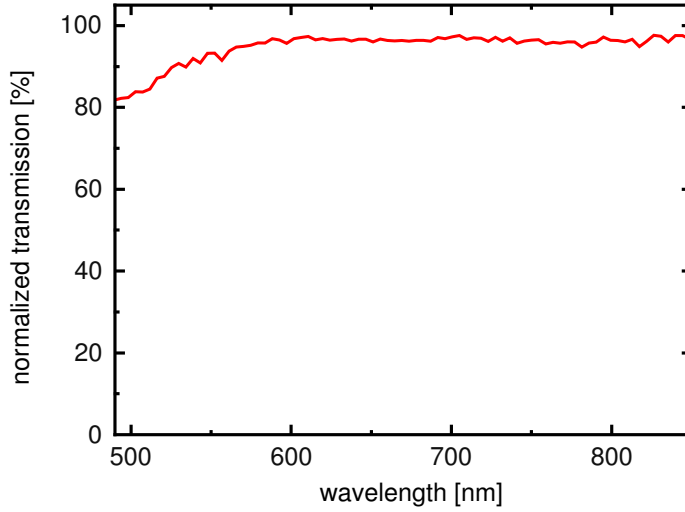


Figure 2.9: Typical transmission spectrum of the TOFs used in this work, normalized to the transmission of the untapered fiber.

and the right hand side of eqn. 2.2 is valid. Absorbance measures the overall loss of the transmission and, besides absorption, this includes scattering losses. For molecules directly adsorbed on the surface of the TOF, the amount of absorbed light depends on the wavelength dependent absorption cross section $\sigma(\lambda)$. It measures the probability for a molecule to get excited via the evanescent field (for further details on the absorption cross section see sec. 3.1.2).

The power $P_{\text{abs}}(\lambda)$ absorbed by a molecule on the waist is given by:

$$P_{\text{abs}}(\lambda) = \sigma(\lambda) \cdot I_{\text{surf}}(\lambda) \quad (2.3)$$

Here, $I_{\text{surf}}(\lambda)$ is the surface intensity of the evanescent field. The effective area of the guided mode A_{eff} is defined by [24]

$$A_{\text{eff}}(\lambda) = P_{\text{ref}}(\lambda) / I_{\text{surf}}(\lambda) \quad (2.4)$$

Thus, the absorbed power per molecule can then be expressed by

$$P_{\text{abs}}(\lambda) = \sigma(\lambda) \cdot \frac{P_{\text{ref}}(\lambda)}{A_{\text{eff}}(\lambda)} \quad (2.5)$$

Assuming² that the effective mode area is much bigger than the molecular absorption cross section ($\sigma(\lambda)/A_{\text{eff}}(\lambda) \ll 1$), this yields an absorbance of [24]

$$\eta(\lambda) \approx \frac{P_{\text{abs}}(\lambda)}{\ln 10 \cdot P_{\text{ref}}(\lambda)} \approx \frac{N\sigma(\lambda)}{\ln 10 \cdot A_{\text{eff}}(\lambda)} \quad (2.6)$$

²For very low temperatures, when the absorption cross section is strongly increased due to the narrowing of the total spectral width of absorption (cf. sec. 3.1.2), this corresponds to a rough estimation.

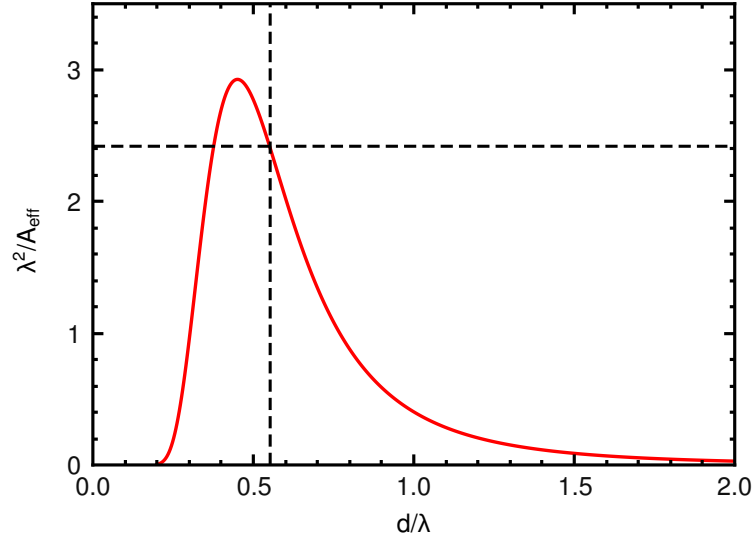


Figure 2.10: Plot of $1/A_{\text{eff}}$ in units of $1/\lambda^2$ in dependency of the fiber diameter d in units of the used wavelength λ for a typical excitation power of $P_{\text{exc}} = 5 \text{ nW}$. The dashed line marks A_{eff} for fibers of 320 nm and an excitation wavelength of 578 nm.

Compared to free-beam surface absorption spectroscopy, where the absorbance for a given surface coverage θ is $\eta_{\text{free}} = \theta\sigma(\lambda)/\ln(10)$, the sensitivity of TOF based spectroscopy is inversely proportional to the effective mode area $1/A_{\text{eff}}$. In order to maximize the sensitivity of a TOF for the spectroscopy of single molecules, $1/A_{\text{eff}}$ has to be maximized. Fig. 2.10 shows this quantity in units of $1/\lambda^2$ in dependence of the fiber diameter d in units of λ . It shows a maximum for $d = 0.45 \cdot \lambda$. For this work, fibers with a diameter of 320 nm are used with excitation wavelengths of round about 578 nm. This leads to $d/\lambda = 0.55$, which is marked with a dashed line. After a molecule on the surface of the TOF has absorbed light, its fluorescence light is emitted into all directions. For nanofiber diameters, wavelengths of about 580 nm, and the molecule described as a single dipole emitter, round about 20 % of the fluorescence can be expected to be coupled into the guided modes of the fiber, 10 % in each direction [40].

If the molecules are not directly adsorbed on the fiber surface but embedded within a crystal with a certain distance from the surface and a defined angle between the molecules' transition dipole moment and the polarization of the guided mode, the situation is slightly different. The single molecule spectroscopy in this work is based on terrylene dye molecules embedded in p-terphenyl crystals, which are deposited or grown directly on the fiber. The transition dipole moment of terrylene is oriented along the long axis of the molecule [41]. Since it has been found experimentally that the orientation of the transition dipole moment of terrylene and the c -axis of p-terphenyl varies between 2° to 4° , it can be concluded that the transition dipole is almost parallel to the c -axis [42]. P-terphenyl grows in the a - b plane as a platy crystal and the long axis of the embedded terrylene molecule can form four different angles between 99.8° and 103.6° with the a -axis of the crystal, depending on the insertion site, cf. sec. 3.3.2. The four different

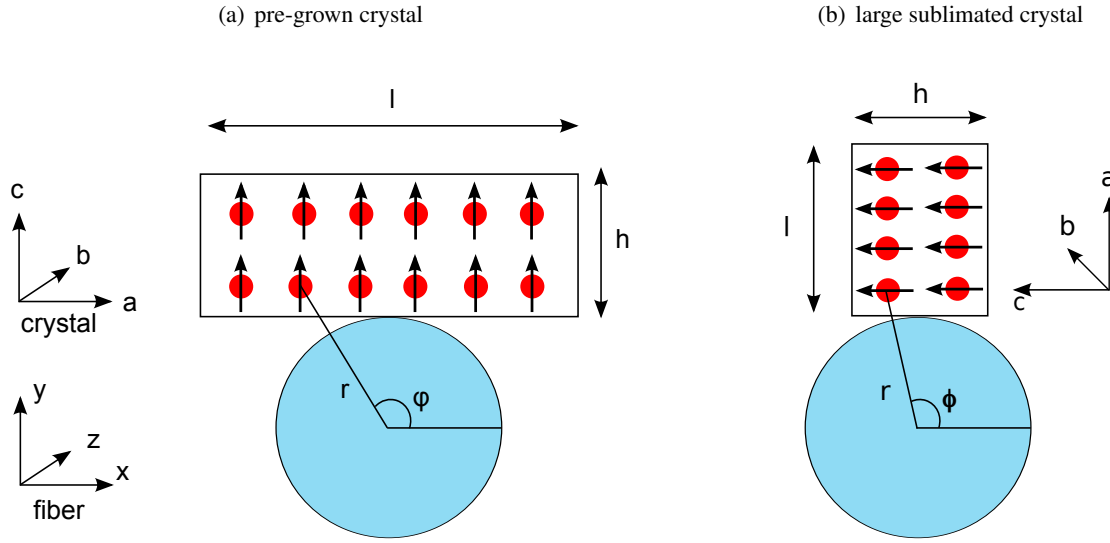


Figure 2.11: Schematic of terrylene doped p-terphenyl crystals on a TOF. The dye molecules and their transition dipole moment is depicted with red circles and small black arrows, respectively. The crystal height is denoted h and the length, which is parallel to the growth in the a - b plane is denoted l . Two different situations are shown: a pre-grown crystal deposited on a TOF at $\phi = 90^\circ$, oriented with the long side l parallel and the dipole moment perpendicular to the fiber's x -axis **(a)** and a large crystal directly grown on the TOF at $\phi = 90^\circ$ via sublimation, where the growth direction is away from the fiber and the dipole moment is parallel to the fiber's x -axis **(b)**. For details see text.

angles are usually equally distributed.

Fig. 2.11 shows a schematic of different crystal orientations on a TOF. The embedded molecule and its dipole orientation are sketched with a red circle and a black arrow, respectively. The size of the crystal is assigned with h for the thickness and l for the side length. The position of a molecule within the crystal with respect to the fiber center is determined by the distance r and the angle ϕ . Along the nanofiber it is the fiber coordinate z . Depending on the growth and deposition method of the doped crystals on the TOF, extensive investigations of the samples with a scanning electron microscope (SEM) showed (cf. ch. 5), that there are mainly two different situations: When pre-grown crystals, e. g. from an oversaturated solution (cf. sec. 5.2), are deposited on the TOF at $\phi = 90^\circ$, the crystal will orient itself with the long axis parallel to x -axis of the fiber and the transition dipole moments are pointing in the y -direction, cf. fig. 2.11(a). Crystals growing directly on the fiber surface, like during sublimation, can have different orientations. Big sublimated crystals are usually growing in the y -direction with the dipole moments in the x - z plane, cf. fig. 2.11(b). For small sublimated crystals no conclusive growth direction could be identified.

The coupling of the evanescent field to one of the crystal-embedded molecules strongly depends on the orientation of the molecule's dipole moment and the position with respect to the

fiber. Although the orientation of the dye molecules within a crystal is approximately the same – with crystal sizes of up to a few micrometers, the different positions lead to very different distances r and angles ϕ with respect to the fiber center. When a crystal-embedded molecule absorbs light, its dipole moment can only interact with the parallel components of the polarization. According to a molecule on the fiber surface and eqn. 2.3 and 2.5, the absorbed power of a crystal-embedded molecule, $P_{\text{abs}}^{\text{crys}}$, at the position \mathbf{r} , excited by linear polarized light with the wavelength λ and the polarization angle ϕ can be expressed as:

$$P_{\text{abs}}^{\text{crys}}(\lambda, \mathbf{r}, \phi, n_c) = \sigma_{\text{mol}}(\lambda) \cdot I_{\text{surf}}(\lambda, \mathbf{r}, \phi, n_c) = \sigma_{\text{mol}}(\lambda) \cdot \frac{c\epsilon_0}{2n_{\text{crys}}} \cdot |E_{\parallel}(\lambda, \mathbf{r}, \phi)|^2 \quad (2.7)$$

$$= \frac{\sigma_{\text{mol}}(\lambda)}{A_{\text{eff}}(\lambda, \mathbf{r}, \phi, n_c)} P_{\text{ref}}(\lambda) \quad (2.8)$$

Here, $\sigma_{\text{mol}}(\lambda)$ denotes the molecular absorption cross section, c the speed of light in vacuum and ϵ_0 the vacuum permittivity. The refractive index of the crystal is denoted with n_{crys} . In this work, p-terphenyl is used which forms biaxial crystals and the refractive index depends on the axis of the crystal with $n_a < n_b < n_c$. More details can be found in sec. 3.3.2. Depending on which molecule inside the crystal is excited and how the crystal is placed on the fiber, the distance r , the angle ϕ , the orientation dependent refractive index n_{crys} and the wavelength can differ. This makes it rather difficult to determine the exact absorbed power per embedded molecule but as a rough estimation, $1/A_{\text{eff}}$ is reduced by approx. 20 % for a molecule with a distance of 10 nm from the fiber surface.

Another problem is the unknown polarization state of the excitation light. For this work, only non-polarization-maintaining fiber is used, where the two possible polarization modes have the same phase velocity. Bending, imperfections and local stress can cause birefringence which leads to coupling between the two perpendicular polarized modes and a power transfer. This results in an unknown polarization state at the position of the crystal on the TOF [43]. However, if the orientation of the crystal is known, a rough estimation of the absorbed power can be given and a study of the polarization dependence could lead to a determination of the molecules position within the crystal.

The surface intensity and therefore the sensitivity of a TOF strongly depends on the diameter of the nanofiber. During the deposition process of the sample on the surface, extreme care is taken to place the sample in the middle of the waist to ensure an optimized coupling to the evanescent field. In the transition part of the TOF, the diameter increases exponentially, strongly reducing the surface intensity of the field and the sensitivity for spectroscopic applications. Therefore, misplaced samples, sample parts or sample residues after cleaning can be assumed to be negligible when it comes to their absorbance/fluorescence. If the sample is too large, a serious problem can be the disturbance of the mode conversion in the taper transition: As mentioned in sec. 2.1.2, when the fundamental mode is converted from the core to cladding modes of the TOF, any disturbance can lead to conversion to a higher order transverse mode. The latter will then experience a cut-off at the corresponding radius of the taper transition and be scattered out of the TOF. This then reduces the power of the guided light. If the sample is too large, the change in refractive index of the surrounding medium can even disturb the light-guiding capabilities of the waist. Therefore, small samples and a correct placement are a prerequisite for spectroscopy of surface adsorbed samples. If the sample interferes with the mode

conversion and/or the light guiding capabilities, an immediate drop in the transmitted power can be observed and the process can be repeated, after removing the misplaced/missized sample.

Spectroscopy of single organic dye molecules – Theoretical background

Since the first detection and spectroscopic investigation of a single molecule within a solid [5] and a solution [44], single molecule spectroscopy (SMS) has been demonstrated for many different combinations of molecules and environments. Measurements with single molecules are performed in many different scientific fields from bio-physics [45] to quantum optics [7]. This wide interest stems from the fact that SMS allows the study and manipulation of a single quantum system. It gives insight into the processes in the molecule sample, such as flipping of molecular groups and guest-host interactions or transport processes, e. g., through cell membranes. For this purpose, the understanding of the interaction between a single molecule and the surrounding medium, such as a solution or a crystal is necessary.

In this chapter, some fundamentals of single molecule spectroscopy, focused especially on crystal-embedded single dye molecules are explained. After introducing the energy levels and optical transitions in organic dye molecules, the characteristics of single molecule spectroscopy are explained. The last part covers the characteristics of the sample system used for SMS in this work.

3.1 Optical properties of organic dye molecules

An organic dye is a soluble substance, which appears to be colored because of its light absorbing behavior: When dye molecules are illuminated with light of the visible range from 400 nm to 800 nm, the latter will be partly absorbed and reflected. The absorbed light has a specific wavelength λ and its absence in the reflected light causes the human eye to perceive a specific color. Since visible light has a relatively low energy, low-energy electronic transitions are necessary. The coloring properties of dye molecules depend on their internal energy structure, caused by intramolecular interactions and interactions with the surrounding environment.

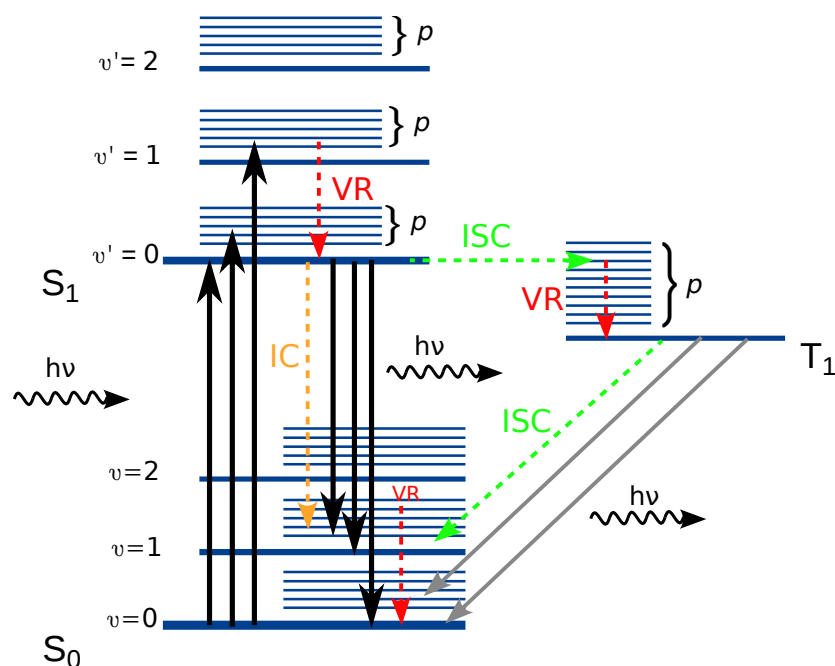


Figure 3.1: Simplified Jablonski diagram of an organic molecule, showing three electronic levels S_0 , S_1 and T_1 , their vibronic substructure (denoted with v and v') and the phonon levels (denoted with p , for clarity only in S_1 and T_1). Radiative transitions are denoted with solid arrows: black and upward (absorption), black and downward (fluorescence), gray and downward (phosphorescence). Non-radiative transitions are denoted with dashed arrows: intersystem crossing (ISC, green), vibrational relaxation (VR, red) and internal conversion (IC, orange). For details see text.

3.1.1 Transitions and energy levels in molecules

Typical dye molecules at room temperature possess many possible transitions leading to a very broad absorption and emission spectrum. Since the emitted radiation depends only on the relative position of the energy levels and the preferred transitions, it is characteristic for the investigated molecule. To visualize the transitions of a molecule, a Jablonski diagram is used. It shows the possible radiative and non-radiative relaxations between different energy levels and the possible energy levels, see fig. 3.1. The electronic ground state is denoted with S_0 . Electrons are fermions and since two identical fermions cannot occupy the same quantum state (Pauli exclusion principle), the only possible level population is paired and antiparallel. This results in a total spin of $S = 0$ and a spin projection quantum number of $m_s = 0$. Such a state is called singlet state. Higher electronic states are the singlet state S_1 and the triplet state T_1 . When a molecule is excited, the electrons do not share the same level necessarily, allowing also unpaired and parallel spins. If the population consists of two unpaired electrons, the state is called triplet state and has a total spin of $S = 1$ and therefore three possible projections $m_s = 1, 0, 1$. Higher electronic states are not shown here since for a dye molecule the excitations take place in the

visible range, and thus within these three levels. Due to many possible vibrational states of the molecule, every electronic state splits into several vibronic states of different energy, denoted with v for S_0 and v' for S_1 . As the molecules in this work are either surface adhered or built into a solid organic matrix, rotations, which would further split the energy levels, are not shown here. Furthermore, dye molecules embedded in a crystal possess phonon levels. Phonons are quantized vibrations of the surrounding solid, e. g., the crystal lattice. Phonon levels cannot be resolved since they have a broad spectral distribution.

Absorption

To excite a dye molecule via absorption of an optical photon, the energy of the excitation light has to match the discrete energy difference $\Delta E = h\nu = hc/\lambda$ between the electronic ground state and the excited state (ν : frequency, λ : wavelength of the irradiated light, c : speed of light, h : Planck constant). When a molecule within a crystal is excited by a laser, the absorbance of a photon with the energy ΔE takes place from the vibrationless electronic ground state S_0 to a specific vibrational or phonon level of the first excited electronic state S_1 , according to ΔE . Due to the surrounding crystal, vibrations are effectively damped and non-radiative transitions lead to a decay to the vibrationless ground state. As mentioned before, the triplet state T_1 has a different total spin, therefore transitions from the ground state directly to the triplet state are forbidden due to total spin conservation and the selection rule ($\Delta S = 0$).

Non-radiative transitions

In molecules, many different processes exist, which result in a non-radiative energy transfer between energy levels. Three main processes are responsible for this energy dissipation: inter-system crossing (ISC), vibrational relaxation (VR) and internal conversion (IC). A molecule is excited from the electronic ground level to a specific vibrational state of the excited electronic state according to the Franck-Condon factor (cf. sec. 3.1.2). This external perturbation brings the molecule out of thermal equilibrium. Internal vibrational relaxation, caused by interaction with the environment, transfers the vibrational energy partially to the surrounding medium within times of picoseconds and the initially excited vibrational mode is transferred to the lowest vibrational state. In the Jablonski diagram in 3.1, these processes are denoted with red dashed arrows, they can only occur within a given electronic state. If the non-radiative transition is not within an electronic level but from a higher to a lower electronic level of same spin multiplicity, it is termed internal conversion (orange arrow in fig. 3.1) and the molecular spin-state remains the same. The electronic energy is converted into vibrational energy and the excess energy is dissipated as heat. For higher electronic excited states, the overlap of the vibrational wavefunctions strongly increases, therefore making the internal conversion between them very probable as described by the Franck-Condon factor (cf. sec. 3.1.2). A non-radiative decay of the S_1 to the ground state S_0 is, due to the energy difference of both states and the small overlap of the vibrational eigenfunctions, very unlikely, but also a decay to the first excited triplet state T_1 is possible. The necessary spin-flip can be induced if the spin-orbit coupling is strong and, as required by energy conservation, the vibrational levels of the two excited states overlap. This is

vibrational relaxation	10^{-12} s to 10^{-10} s
intersystem crossing	10^{-10} s to 10^{-8} s
internal conversion	10^{-11} s to 10^{-9} s

Table 3.1: Typical times for non-radiative transitions in a molecule [46].

more likely for molecules with heavy atoms, since the spin-orbit coupling is proportional to Z^4 , where Z is the atomic number. The intersystem crossing is denoted with green arrows in fig. 3.1.

All these non-radiative processes are independent of each other. Their different transition times can be seen in tab. 3.1. Due to the transition probabilities an excitation from S_0 to a higher electronic level is followed by a typical sequence: first, a transition via vibrational relaxation within S_1 to the vibrational ground state is performed. If no photon is emitted, a further decay can occur via an internal conversion to the ground state, which is rather improbable due to the high number of phonons to be emitted [47] or via intersystem crossing to any vibrational level of T_1 . After a further internal conversion to the vibrational ground state of the triplet state, the molecule can return into the ground state by emission of a phosphorescence photon or an intersystem crossing to the ground state, followed by a vibrational relaxation to the vibrational ground state of the electronic ground state.

Emission

After the molecule underwent internal non-radiative transitions, it can decay directly from the vibrational ground state of S_1 to any of the vibrational states of the electronic ground state by emitting a photon. This emission process is called fluorescence (black downward pointing arrows in fig. 3.1) and because of the energy loss due to non-radiative decays, the emitted energy is smaller than the one absorbed before: $\Delta E_a > \Delta E_f$. This shifts the wavelength of fluorescence to longer wavelengths than the absorption wavelength. The energy of the fluorescence photon is reduced by the energy of all involved non-radiative processes: $\Delta E_f = \Delta E_a - \Delta E_{nr}$. To describe the relative proportion of the fluorescence decay of the overall decay rate, the fluorescence quantum yield is introduced:

$$\Phi_f = \frac{k_f}{k_f + k_{nr}} \quad (3.1)$$

with fluorescence and non-radiative decay rates k_f and k_{nr} . Therefore, high fluorescence quantum yields can be found for molecules with low IC and ISC rates. The ISC rate leads to the triplet quantum yield Φ_T , which characterizes the relative proportion of the transitions from T_1 to the ground state of the overall decay rate:

$$\Phi_T = \frac{k_{23}}{k_{21} + k_{23}} \quad (3.2)$$

with k_{23} as the ISC rate from S_1 to T_1 and k_{21} as the decay rate from S_1 to S_0 . The reciprocal value of the fluorescence decay rate and all non-radiative decay rates is the lifetime of the excited electronic state S_1 :

$$\tau_f = \frac{1}{k_f + k_{nr}} \quad (3.3)$$

Typically, this fluorescence lifetime is between 10^{-10} s and 10^{-7} s. If the molecule does not decay radiatively from the singlet state, but from the triplet state, this process is called phosphorescence and also ends up in any of the vibrational levels of the electronic ground state (gray downward pointing arrows in fig. 3.1). The decay to the electronic ground state from the triplet state includes a spin-flip. The triplet state has a lower energy as the first excited singlet state and therefore the energy of the emitted phosphorescence photon is smaller, than that of fluorescence: $\Delta E_f > \Delta E_p$. As the transition from a triplet to a singlet state is forbidden due to spin selection rules, the lifetime can reach up to a few seconds.

Optical lineshapes of dyes in organic crystals

When dye molecules are embedded in a host, phonon states yield a large number of additional energy levels and possible transitions. For the lineshape of such a guest-molecule, these phonons and their energies have to be taken into account. Analogously to the harmonic oscillator, the energy of a vibrational state with the angular frequency ω_{ph} and n phonons is $E_n = (n + 1/2)\hbar\omega_{\text{ph}}$. The mean occupation number $\langle n \rangle$ of a state at the temperature T is determined by Bose-Einstein statistics [48]:

$$\langle n \rangle = \frac{1}{\exp(\hbar\omega_{\text{ph}}/k_B T) - 1} \quad (3.4)$$

The mean occupation number $\langle n \rangle$ and therefore the number of possible transitions in which phonons are involved is strongly dependent on the temperature. For high temperatures, the large number of these additional transitions leads to a very broad absorption and emission spectrum, represented by the so-called phonon sideband. When $T \rightarrow 0$ K, the number of phonons is strongly reduced and the spectrum is dominated by a narrow band which consists of the pure electronic transitions to the vibronic levels. It is called the zero-phonon line (ZPL) and is centered at a frequency ν_0 , which is the same for absorption and emission. Such a combination of ZPL and phonon sideband exists for every transition from the electronic ground state to the corresponding vibrational levels, e. g. the absorption $S_0^0 \rightarrow S_1^0$ is named 0-0 transition. Accordingly, $S_0^0 \rightarrow S_1^1$ is the 0-1 transition. Fig. 3.2 schematically shows the shape of an absorption profile of a molecule within a matrix at low temperatures of a selected transition. The ZPL has the shape of a Lorentzian. The elastic scattering of a crystal phonon at the molecule can cause a shift of the energy levels, leading to a change in the phase of the dipole oscillation. At low temperatures, this dephasing effect is negligible and the width $\delta\nu$ corresponds to the natural linewidth of the transition of the molecule, which is typically 10 - 100 MHz. The phonon sideband is a superposition of all participating phonon transitions. Since the number of these phonon transitions is a number of discrete and independent events, the phonon sideband yields a Poissonian distribution. At high temperatures, when the number of phonons is strongly increased, the shape is approximately a Gaussian. With a width of round about 1 THz [49], the phonon wing is much broader than the ZPL. The shift between ν_0 , the center of the ZPL, and the center of the phonon wing corresponds to the energy shift of the pure electronic transition and the phonon levels. It is usually between 0.5 THz and 6 THz [49]. For high temperatures, when the number of phonons is increased, the ZPL is broadened via dephasing and overlapped by the broadened phonon sideband. Due to non-radiative transitions, for absorption, the the phonon sideband is located on

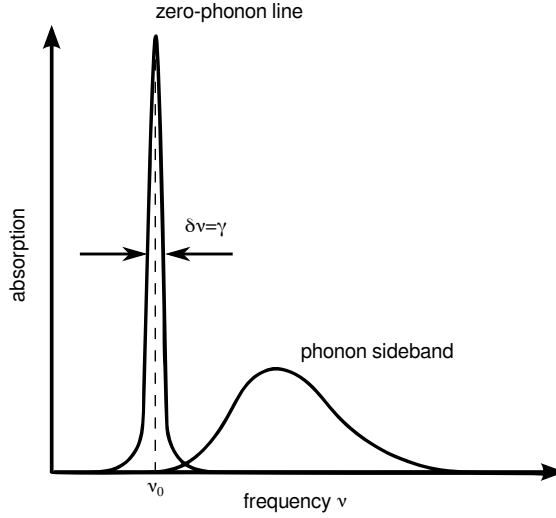


Figure 3.2: Schematic of an absorption profile of a selected transition in a single molecule embedded in host matrix at low temperatures. It consists of a phonon sideband and a zero-phonon line with a Lorentzian shape centered at ν_0 and the width $\delta\nu$.

the high energy side of the ZPL, while for emission, it is located on the low energy side. The intensity of the zero phonon transition with respect to the phonon transitions, is expressed with the Debye-Waller factor:

$$\alpha_{\text{DW}} = \frac{I_{\text{ZPL}}}{I_{\text{ZPL}} + I_{\text{PSB}}} \quad (3.5)$$

with I_{ZPL} and I_{PSB} as the integral intensities of the zero-phonon line and the phonon sideband.

3.1.2 Transition probabilities in molecules

At low temperatures, when the number of phonons is strongly reduced and the spectrum is dominated by the ZPL, the transition probabilities can be treated approximately by a two-level system.

Einstein coefficients

When the transition probability between two states E_i and E_k is different from zero, a transition $E_i \leftrightarrow E_k$ can be observed and radiation is absorbed or emitted.

If the molecule is within an electromagnetic field with the spectral energy density $\rho(\nu) = n(\nu)h\nu$, with $n(\nu)$ as the spectral number density of photons, the probability for the molecule to absorb a photon per second and to pass from an energetic lower to a higher state $|i\rangle \rightarrow |k\rangle$ is

$$P_{ik} = B_{ik} \cdot \rho(\nu) \quad (3.6)$$

The constant B_{ik} is called Einstein coefficient for induced absorption and it is only dependent on the specific transition $|i\rangle \rightarrow |k\rangle$ of the molecule. The energy of absorbed photons has to match the energy difference between both states, hence $h\nu = (E_k - E_i)$.

An excited molecule can loose its excitation energy via spontaneous emission of a photon. This process is independent of an external electromagnetic field and the according probability for the transition from the level of higher energy $|k\rangle$ to the level of lower energy $|i\rangle$ via the emission of a photon with the energy $h\nu = (E_k - E_i)$ is

$$P_{ki}^{\text{spontan}} = A_{ki} \quad (3.7)$$

Here, the constant A_{ki} is the Einstein coefficient of spontaneous emission. The average emitted power during the spontaneous emission follows directly as the product of probability and energy of the emitted photon:

$$\langle \tilde{P} \rangle = A_{ik} \cdot h \cdot \nu_{ik} \quad (3.8)$$

When the radiation field forces a molecule to decay from the excited state $|k\rangle$ to the ground state $|i\rangle$ via the emission of a photon, the probability of this induced emission is

$$P_{ki} = B_{ki} \cdot \rho(\nu) \quad (3.9)$$

with B_{ki} as the Einstein coefficient of the induced emission. Induced emission is an important process for the occurrence of Rabi oscillations, which can be observed for the emission characteristics of a molecule for short times (cf. sec. 3.2.3). If the fluorescence is emitted via the transition from the S_1 state, the fluorescence decay rate corresponds to the Einstein coefficient:

$$k_f = \tau_f^{-1} = P_{21} = A_{21} \quad (3.10)$$

Another way of characterizing an absorption process is the intensity loss of an electromagnetic wave with the initial intensity I_0 , traveling through a medium along the z-axis. It is described by the Lambert-Beer law:

$$dI = -\alpha(\nu) I dz \Rightarrow I(z, \nu) = I_0(\nu) \cdot \exp[-\alpha(\nu) \cdot z] \quad (3.11)$$

The frequency dependent absorption coefficient is denoted $\alpha(\nu)$ and describes the strength of the attenuation of the light beam passing the medium. It is proportional to the number density \bar{n} of absorbing molecules N in the sample volume V :

$$\alpha(\nu) = \bar{n} \cdot \sigma(\nu) \quad (3.12)$$

This defines the absorption cross section $\sigma(\nu)$ as the effective area of a molecule that a photon needs to impinge on in order to be absorbed. At very low temperatures, when the optical absorption profile becomes the narrow ZPL, the absorption cross section of a single molecule on resonance approaches the fundamental value of

$$\sigma_{\text{ZPL}} = \frac{3\lambda^2}{2\pi} \quad (3.13)$$

with the excitation wavelength λ . While the typical absorption cross section of a dye molecule at room temperature with $\lambda = 500 \text{ nm}$ is approx. $\sigma = 4 \times 10^{-16} \text{ cm}^2$, this increases for the fundamental limit to approx. $\sigma_{\text{ZPL}} = 1 \times 10^{-13} \text{ cm}^2$. For spectroscopy with a TOF the situation

is slightly different and the effective mode area A_{eff} of the fiber mode has to be taken into account (cf. sec. 2.1.3).

In practical applications, usually the frequency dependence of an absorption or emission process has to be taken into account. To relate the Einstein coefficient for absorption B_{ik} , which was defined for an energy density which is constant over the frequency range, to the absorption cross section $\sigma(\nu)$, the coefficient has to be expressed for a monochromatic, directed wave. This leads to the cross section $\sigma_{ik}(\nu)$ per molecule for a transition $|i\rangle \rightarrow |k\rangle$ [50]:

$$\int \sigma_{ik}(\nu) \cdot d\nu = \frac{2\pi\nu\hbar}{c} B_{ik} \quad (3.14)$$

The integration is carried out over all frequencies of the spectral profile of the absorption line.

Franck-Condon principle and transition dipole moment

For a full understanding of the optical properties of dye molecules, the energy structure of molecules has to be considered. This leads to a very complex many-body problem, containing the nuclei and the electrons. The resulting Schrödinger equation has no analytical solution and even a numerical solution is outstandingly difficult. Therefore, the problem is solved using the so-called Born-Oppenheimer approximation [51]. The mass of the nuclei is much bigger than the mass of the electrons. This leads to a much greater velocity of the electrons compared to the nuclei which means that electronic dynamics are instantaneous compared to movements of the nuclei. The movement of the nuclei is therefore so small compared to that of the electrons that it is supposed to be fixed during electronic transitions. The total wavefunction of the molecule $\Psi(\mathbf{r}, \mathbf{R})$, which is dependent on the positions of the electrons \mathbf{r} and the positions of the nuclei \mathbf{R} , can thus be written as a product of nuclear (thus also including vibrational and rotational components) and electronic parts:

$$\Psi(\mathbf{r}, \mathbf{R}) = \phi_{\text{electrons}}(\mathbf{r}) \cdot \chi_{\text{nuclei}}(\mathbf{R}) \quad (3.15)$$

This separation allows the separate treatment of both wavefunctions. By assuming a fixed position for all nuclei, the Schrödinger equations of the electrons can be solved for this nuclear positions. This process is repeated for all possible nuclear positions, which maps out the energy of the molecule with respect to the nuclear constellation. The energies E can be plotted in dependence of the coordinates of the nuclei \mathbf{R} , resulting in the potential energy surface of the molecule. The potential energy surface represents the energy which is necessary to move the nuclei within the molecule. The minimum of a potential energy surface represents the equilibrium nuclear constellation. Fig. 3.3 shows a schematic of the potential energy surfaces for the electronic ground state S_0 and the first excited state S_1 as a function of the nuclear coordinates \mathbf{R} . Possible vibrational states are given and denoted with ν for the ground state and ν' for the first excited state. For each vibrational state, the vibrational wavefunction for the nuclei coordinate $\chi(\mathbf{R})$ is sketched.

The organic molecules used in this work are typically embedded in a host crystal which leads to additional phonon levels. The phonon interactions can be included in the nuclear parts within the Born-Oppenheimer approximation, leading to additional states in the vibrational level

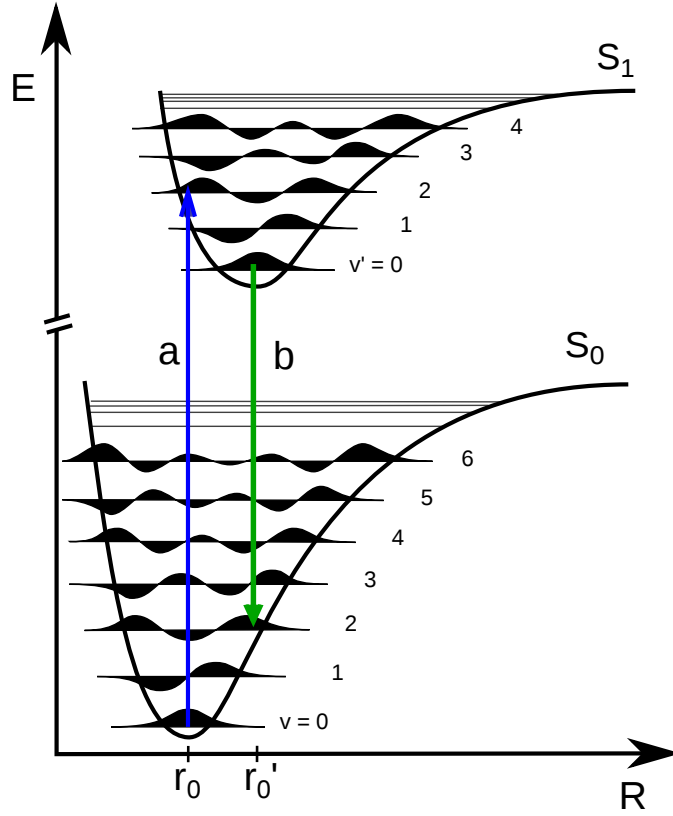


Figure 3.3: Schematic plot of the potential energy surfaces for the electronic ground state S_0 and the first excited state S_1 as a function of the nuclear coordinates \mathbf{R} . For each vibrational level, the vibrational wavefunction $\chi(\mathbf{R})$ is given. Both arrows denote a radiative transition in the molecule: (a) absorption and (b) emission.

structure. These levels are not shown in fig. 3.3. From the vibrational wavefunction $\chi(\mathbf{R})$, the probability density $\rho(\mathbf{R}) = |\chi(\mathbf{R})|^2$ can be determined. For large ν and ν' , $\rho(\mathbf{R})$ only gets large close to the potential energy surface. These are the classical turning points of the oscillation of the molecule.

A molecule can be approximated as an electromagnetic dipole, which absorbs and emits electromagnetic radiation. For every dipole, an electric dipole operator \hat{d} can be defined, which characterizes the strength of these two effects. Besides the electrons with the position vector \mathbf{r}_i , also the nuclei with the charge Ze and the position vectors \mathbf{R}_j add to the dipole operator:

$$\hat{d} = -e \sum_i \mathbf{r}_i + Z_1 e \mathbf{R}_1 + Z_2 e \mathbf{R}_2 + \dots = \hat{d}_{el} + \hat{d}_N \quad (3.16)$$

The coupling strength of a transition between two energy levels $E_i \rightarrow E_k$ is defined by the matrix element of the dipole operator [52]:

$$\mathbf{D}_{ik} = \int \Psi_i^* \hat{d} \Psi_k d\mathbf{r} \cdot d\mathbf{R} \quad (3.17)$$

The integration $d\mathbf{r}$ is carried over the configuration space of the electrons, $d\mathbf{R}$ over the nuclear coordinates of the molecule. The average power, emitted by a dipole in all directions during such transition is defined as [52]

$$\langle \tilde{P}_{ik} \rangle = \frac{4}{3} \frac{\omega_{ik}^4}{4\pi\epsilon_0 c^3} |\mathbf{D}_{ik}|^2 \quad (3.18)$$

Here, the angular frequency of the transition is denoted $\omega_{ik} = 2\pi\nu_{ik}$. To simplify the transition dipole moment, the Born-Oppenheimer approximation can be used and the wavefunctions of \mathbf{D}_{ik} can be separated into electronic and vibrational parts. Since only transitions between different electronic levels are of interest, it can be shown [52] that the intensity of a transition is

$$I_{ik} \propto |\mathbf{D}_{ik}^{el}|^2 \cdot FC(\nu_i, \nu_k) \cdot HL(J_i, J_k) \quad (3.19)$$

Hence, the intensity of a spectral line of a transition is determined by three factors: the electronic part of the matrix element $|\mathbf{D}_{ik}^{el}|^2$ assigns the probability for an electronic transition between the two states. The second factor is the so-called Franck-Condon factor $FC(\nu_i, \nu_k) = |\langle \chi_k | \chi_i \rangle|^2$. The Franck-Condon factor predicts which transitions between vibrational levels of the two electronic states are most probable: since the coordinate of the nuclei is not changing during the transition (cf. Born-Oppenheimer approximation), vertical transitions can be assumed between both potential energy surfaces of fig. 3.3. A transition is more probable, the larger the overlap between the vibrational function in the ground state and the excited state is. In fig. 3.3, these two most probable transitions are denoted with the arrows. The last factor is the so-called Hönl-London factor, which determines the spatial distribution of the emitted radiation [50].

3.1.3 Optical Bloch equations

When a dye molecule is coherently excited via laser light, the photophysical dynamics of the molecule consist of two components: a coherent coupling between the electronic ground state (S_0 , abbreviated $|1\rangle$) and the first electronic excited state (S_1 , abbreviated $|2\rangle$), driven by the coherent laser and coupling to incoherent transitions, causing radiative and non-radiative transitions between the electronic levels. A crystal-embedded dye molecule can be treated like a purely electronic three level systems with T_1 (abbreviated $|3\rangle$). This is possible since all vibrational states are damped and decay within picoseconds but the transitions between the electronic levels take place within nanoseconds, thus much slower. Therefore, all photophysical processes can be treated as transitions between the purely electronic levels, without taking into account the splitting to vibronic sub-levels. The time dependent wave function for such a three level system is

$$|\psi(t)\rangle = c_1(t)|1\rangle + c_2(t)|2\rangle + c_3(t)|3\rangle \quad (3.20)$$

where the amplitude coefficients are denoted with $c_i(t)$. By defining the density operator [53]

$$\hat{\rho} = |\psi(t)\rangle\langle\psi(t)| \quad (3.21)$$

the 3×3 density matrix can be deduced. It contains the maximum possible information which can be deduced from the system and describes the current state of the molecule. The density matrix elements are

$$\rho_{ij} = \langle i | \hat{\rho} | j \rangle = \langle i | \psi(t) \rangle \langle \psi(t) | j \rangle = c_i(t) c_j^*(t) \quad (3.22)$$

While the diagonal elements ρ_{ii} are the probabilities to find the molecule in the specified state (with $\rho_{ii} = |c_i|^2$ as the probability for state $|i\rangle$), the off-diagonal elements ρ_{ij} are the probabilities to find the system in a coherent superposition of two states. The excitation with an external field, e. g. laser causes a disturbance which leads to a time evolution of the system, hence for the density operator. From the time dependent Schrödinger equation the Liouville-von Neumann equation can be deduced, which describes the time evolution of the density operator [53]:

$$\dot{\hat{\rho}} = \frac{1}{i\hbar}[\hat{H}, \hat{\rho}] \quad (3.23)$$

with \hbar as Planck's reduced constant. The total Hamiltonian is given by $\hat{H} = \hat{H}_E + \hat{H}_I + \hat{H}_R$, where \hat{H}_E is the stationary Hamiltonian of the unperturbed three level system and the Hamiltonian for the interaction between excitation light and molecule $\hat{H}_I = -\hat{d}\mathbf{E}_L$. Here, \hat{d} is the dipole operator of the molecule and \mathbf{E}_L the electric field amplitude of the laser light which includes the polarization. The Hamiltonian for all other relaxation processes \hat{H}_R takes into account spontaneous emission and all other perturbing effects, which cause the excited state to depopulate. With the electric dipole and rotating-wave approximation, thus assuming that the molecule is large compared with the wavelength of the excitation light and neglecting all processes which are counter-rotating to absorption and emission (i. e. all emitted photons during absorption and all absorbed photons during emission), the optical Bloch equations for a three level system can be derived as equations of motion for the elements of the density matrix [54]

$$\dot{\rho}_{11} = k_{21}\rho_{22} + k_{31}\rho_{33} + i\Omega/2(\rho_{21} - \rho_{12}) \quad (3.24)$$

$$\dot{\rho}_{22} = -(k_{21} + k_{23})\rho_{22} + i\Omega/2(\rho_{12} - \rho_{21}) \quad (3.25)$$

$$\dot{\rho}_{33} = k_{23}\rho_{22} - k_{31}\rho_{33} \quad (3.26)$$

$$\dot{\rho}_{12} = -i\Omega/2\rho_{11} + i\Omega/2\rho_{22} + (i\Delta - \Gamma_2)\rho_{12} \quad (3.27)$$

These equations fully describe the behavior of a three level system which interacts with a coherent light field and no coherent coupling between the singlet and triplet state exists ($\rho_{13} = \rho_{23} = 0$). The sum of the diagonal elements of the density matrix is one: $\text{Tr}(\hat{\rho}) = \rho_{11} + \rho_{22} + \rho_{33} = 1$. The incoherent transition rates are denoted with k_{ij} and $\Delta = \omega_0 - \omega$ is the detuning of the excitation laser frequency ω with respect to the resonance frequency of the molecule ω_0 . The dephasing rate of the S_0 - S_1 coherence is denoted with $\Gamma_2 = 1/2T_1 + 1/T_2^*$ and consists of the lifetime of the excited state T_1 and the pure dephasing time T_2^* , compare eqn. 3.31. The interaction between the oscillating electric field of the laser and the states of the molecule is defined by the Rabi frequency Ω :

$$\Omega = \frac{|\mathbf{D}_{21} \cdot \mathbf{E}_L|}{\hbar} \quad (3.28)$$

with $\mathbf{D}_{21} = \langle 2|\hat{d}|1\rangle$ as the matrix element of the dipole operator. By solving the Bloch equations for different conditions, different situations for the molecule can be treated and can be found in detail elsewhere [55]. When the laser is switched on for $t = 0$, for $t \rightarrow 0$ (transient solution) the time dependent population of the first excited state S_1 can be derived and for $t \rightarrow \infty$ (steady state solution) line shape and saturation effects can be calculated. Some of it will be treated in the next sections.

3.1.4 Line shape broadening effects

When light is emitted by a molecule with a resonance transition frequency ν_{ik} , the frequency is not strictly monochromatic but distributed around a center frequency ν_0 of the transition. The distribution is expressed via the line shape function $g(\nu)$. Depending on the molecule and the environment, there can be several broadening effects, resulting in different line shape functions.

Homogeneous line shape broadening

The homogeneous broadening covers all broadening mechanisms which are the same for every molecule of the same kind within a sample. Like a classical electromagnetic source of radiation, an excited molecule loses its excitation energy exponentially via radiation. The loss of energy via spontaneous emission of an excited molecule can be described by the model of a damped harmonic oscillator with the eigenfrequency ω_0 and the damping constant γ . Because of the decreasing amplitude of the oscillation, the angular frequency ω of the emitted radiation is not monochromatic. The frequency spectrum of the emitted electromagnetic wave can be obtained by a Fourier transformation and corresponds to a Lorentzian distribution [50]:

$$g(\omega) = \frac{1}{2\pi} \frac{\gamma}{(\omega - \omega_0)^2 + (\gamma/2)^2} \quad (3.29)$$

The maximum of the Lorentzian lineshape is located at the angular frequency $\omega = \omega_0$. From eqn. 3.10 it is known, that the lifetime of a state $\tau_i = 1/A_i$ is determined via the Einstein coefficient of spontaneous emission. Therefore, the classical damping constant γ can be replaced by the transition probability A_i . Since γ relates to the width of the Lorentz lineshape $\Delta\omega = 2\pi\Delta\nu$ via the Fourier transformation, this leads to

$$\Delta\nu = \frac{\Delta\omega}{2\pi} = \frac{A_i}{2\pi} = \frac{1}{2\pi \cdot \tau_i} \quad (3.30)$$

for a transition from an excited state E_i to the ground state E_0 . This defines the natural linewidth $\Delta\nu$ of a transition, it is the full width at half maximum (FWHM) of the Lorentzian distribution. The natural linewidth is a fundamental lower limit for the width of a spectral line. This is due to the Heisenberg uncertainty principle: a state with a limited lifetime τ has an energy uncertainty $\Delta E = \hbar/\tau$. This leads directly to an uncertainty for the transition frequency $\Delta\nu = \Delta E/h$ and hence to eqn. 3.30. For molecules, coupled with the environment, like organic molecules embedded in a host matrix, further homogeneous broadening effects exist, mainly due to phonon interactions. Although the coupling to the host phonons provide additional decay channels for an excited molecule, which would result in a reduced lifetime of the excited state, a relaxation from the excited state to the ground state only via phonons is rather improbable due to the large energy difference between both states and the huge required number of phonon levels [47]. Nevertheless, the elastic scattering of a crystal phonon by the molecule can cause a shift of the energy levels, leading to a change in the phase of the dipole oscillation. This dephasing effect causes a temperature dependent broadening which adds to the homogeneous linewidth [56]:

$$\Delta\nu(T) = \frac{1}{2\pi \cdot T_1} + \frac{1}{\pi \cdot T_2^*(T)} \quad (3.31)$$

Here, $T_1 = \tau$ is the lifetime of the excited state. The pure dephasing time is denoted with T_2^* and it is strongly dependent on the temperature. Moreover, it follows an Arrhenius-type equation, which describes the temperature dependence of a chemical reaction [57]:

$$T_2^*(T) = T_2^*(\infty) \cdot \frac{1}{\exp(-E_a/k_B T)} \quad (3.32)$$

The activation energy is denoted by E_a and the Boltzmann constant by k_B . The pure phase relaxation time $T_2^*(\infty)$ is a measure of the the phonon coupling. If $T \rightarrow 0$ K, the number of phonons is highly reduced and the dephasing can be neglected.

Beside lifetime broadening and temperature dependent line broadening, power broadening can also occur. Since the transition probability has a Lorentzian lineshape itself, the saturation of the transition is stronger in the center of the lineshape than on the wings. Therefore, power broadening leads to a compression of the absorption profile and a line broadening. To calculate the influence of the excitation power on the homogeneous linewidth, the steady state solution of the optical Bloch equations 3.24 - 3.27 ($\rho_{11} = \rho_{22} = \rho_{33} = \rho_{12} = 0$) has to be found. The power dependent excitation linewidth for a single molecule has a Lorentzian lineshape and is [56]:

$$\Delta\nu(I) = \Delta\nu_0 \sqrt{1 + \frac{I}{I_S}} \quad (3.33)$$

with $\Delta\nu_0$ as the natural linewidth. The excitation intensity is denoted by I and the saturation intensity of the molecule on transition is denoted by I_S [56]:

$$I_S = \frac{\epsilon c \hbar^2 (k_{21} + k_{23})}{|\mathbf{D}_{21}|^2 (2 + k_{23}/k_{31}) T_2} \quad (3.34)$$

with \mathbf{D}_{21} as the matrix element of the dipole operator and the dephasing rate $1/T_2 = 1/2T_1 + 1/T_2^*$. The saturation intensity I_S is defined such that when $I = I_S$ on resonance, one quarter of the molecules will be excited in the steady state. When the triplet state is ignored, the difference in the population of ground state and excited state can be expressed by [58]

$$n_1 - n_2 = \frac{n}{1 + \frac{I}{I_S}} \quad (3.35)$$

with n as the total number density of molecules and n_i as the number density of the molecules in the energy state E_i . By applying the steady-state solution for the optical Bloch equations for the excited state, the population inversion is found to be [58]

$$\rho_{11} - \rho_{22} = \frac{1}{1 + 2\Omega^2/\Gamma_2^2} \quad (3.36)$$

By comparing eqn. 3.35 and eqn. 3.36, an expression for the saturation intensity I_S can be found in terms of the Rabi frequency Ω [58]:

$$\frac{I}{I_S} = \frac{2\Omega^2}{\Gamma_2^2} \quad (3.37)$$

The fluorescence emission rate R for a single molecule is also dependent on the excitation intensity and can be derived as [56]:

$$R(I) = R_{\infty} \frac{I/I_S}{1 + I/I_S} \quad (3.38)$$

Here, R_{∞} is the fully saturated emission rate [56]

$$R_{\infty} = \frac{(k_{21} + k_{23})\Phi_f}{2 + k_{23}/k_{31}} \quad (3.39)$$

with Φ_f as the fluorescence quantum yield (cf. eqn. 3.1).

Inhomogeneous line shape broadening

The effect of inhomogeneous broadening covers all broadening mechanisms which are different for every molecule within a sample. For crystal-embedded molecules this is caused by guest-host interactions. In host materials, the local environment for every embedded molecule can vary due to imperfections like structural defects or local tension, caused by external perturbations of the crystal structure or by the embedded molecule itself, cf. fig. 3.4(a). These perturbations can cause varying electric fields or field gradients or varying strain fields at the position of every embedded molecule [59]. Without these perturbations, each of the guest molecules would have a homogeneously broadened Lorentzian lineshape. Since for every guest molecule the external effects are different in cause and strength, they cause a shift of the transition frequency around the center frequency ν_0 with respect to the unperturbed molecular transition and the absorption band of the molecular ensemble is a superposition of these Lorentzian lineshapes and therefore broader. Such an inhomogeneously broadened absorption line is schematically shown in fig. 3.4(b). The overall line profile of this inhomogeneously broadened lines can have different shapes depending on the environment the molecules are embedded in. When the transition frequencies are distributed over a large spectral range, like in polymers, where the embedded molecules are unsorted and therefore a higher degree of structural disorder is present, the inhomogeneous lineshape has a Gaussian shape and is usually very broad ($\Delta\nu > 1000$ GHz [49]). Crystals however, offer a highly ordered lattice with a limited number of orientations for the guest molecules. This strongly reduces the possible interactions and the inhomogeneous linewidth ($\Delta\nu = 1 - 100$ GHz [49]).

For a full determination of the shape of an inhomogeneously broadened line, the defect concentration has to be taken into account. A low concentration of defects induces a Lorentzian lineshape [59, 60]. If the defect concentration is slightly higher, the different configurations of nearby defects causes the lineshape to show a so-called "satellite structure" [60]. For a very large defect density with at least half the sites occupied by defects, the lineshape becomes Gaussian [60].

In contrast to homogeneous broadening, inhomogeneous broadening does not depend on temperature. At low temperatures ($T < 20$ K) [61], inhomogeneous broadening is the dominating effect for the width of an absorption band, at higher temperatures it is the homogeneous broadening.

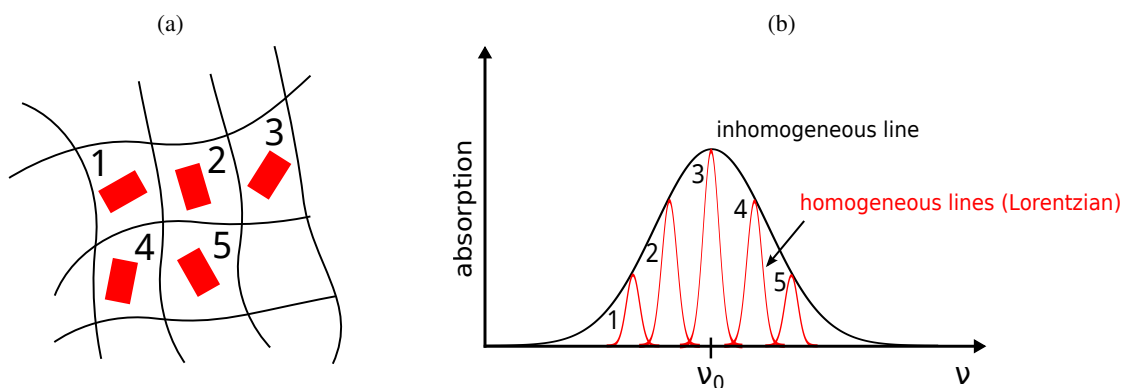


Figure 3.4: Schematic of the origin of inhomogeneous broadening for molecules embedded in a host-crystal. **(a)** shows molecules (red, numbered) embedded in a matrix in different local environments, due to imperfections of the material. **(b)** shows the resulting inhomogeneous broadened absorption line (black), formed as a superposition of the Lorentzian homogeneous profiles of the molecules (red, numbered accordingly). The inhomogeneous line is distributed around the center frequency ν_0 .

3.2 Spectroscopy of single molecules

Conventional molecule absorption and fluorescence measurements deal with the investigation of molecular ensembles. Therefore, all gathered information is always the superposition of all participating single emitters. The properties of a single molecule cannot be deduced from this average result. E. g. from a constant fluorescence rate of an ensemble, the conclusion that every participating emitter also shows a constant emission rate is not valid, e. g., particular molecules can show blinking, an occasional fluorescence emission.

The investigation of single molecules facilitates to overcome this limitation and allows to directly examine the special characteristics of only one emitter. Single molecule spectroscopy (SMS) reveals precise information on the interaction between the radiation field of the excitation light and one molecule, which represents an easy accessible single quantum system and allows insights into the interactions between the surrounding and the single emitter.

To perform spectroscopic single molecule experiments, two requirements have to be fulfilled: only one molecule in the volume is under study and the emitted light has to be distinguishable from the experimental noise. While the first demand can be fulfilled relatively easy via spatial or spectral selection, the second one requires the choice of the right sample system and a careful preparation of the experimental setup.

3.2.1 Spatial and spectral selection

For the investigation of a single molecule, it is essential to make sure that only one molecule is excited. This means that the sample volume which is illuminated with light of a certain wavelength must only contain one absorbing dye molecule. This can be reached in two different

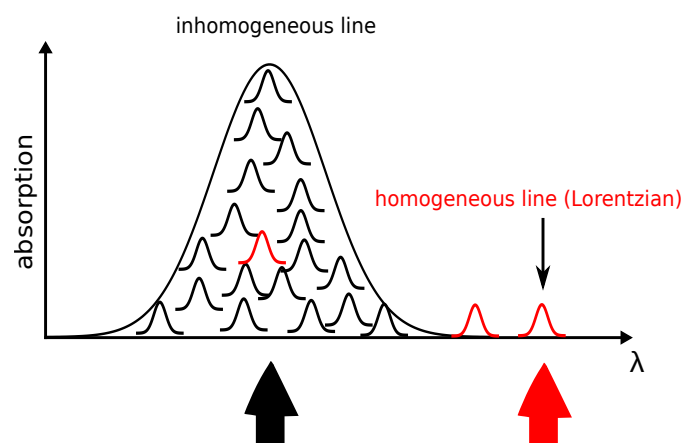


Figure 3.5: Schematic of the principle of spectral selection. At low temperatures, the inhomogeneous line is the superposition of homogeneous profiles of the excited single molecules. Due to the overlap of absorption lines, close to the center no single molecule can be excited (broad black arrow). If the laser frequency is detuned to the wing of the inhomogeneous line, single molecules can be excited, since they do not overlap (broad red arrow).

ways: for spatial selection, the number of absorbers irradiated by the excitation light is reduced to one, either by lowering the concentration within the sample, by reducing the sample volume or by focusing the excitation laser beam onto a small volume of the sample. To take advantage of spatial selection for experiments with a confocal microscope, doping concentrations down to 10^{-9} mol/mol and sample thicknesses of $\sim 1 \mu\text{m}$ down to 80 nm were used in single molecule experiments [42] [62].

However, if SMS is performed with nanofibers and the molecular sample is excited via the fiber, spatial selection is not possible, since all molecules with the same excitation frequency on the TOF will be excited and the reduction to only one single dye molecule within the sample is in a actual fact impossible. As mentioned in sec. 3.1.4, crystal-embedded molecules show inhomogeneous broadening due to guest-host interactions. Differences in the local environment for every molecule cause a shift of the transition frequency around the center frequency ν_0 . At low temperatures, the absorption band of the molecular ensemble is the superposition of these homogeneous lifetime-limited lineshapes, generating an inhomogeneous line. The distribution of the transition frequencies is not homogeneous, yielding larger distances between the shifted frequencies in the wings of the inhomogeneous line. If the width of such a shifted absorption line is less than the distance to the next shifted line, a single molecule transition can be resolved, which can then be addressed with a narrowband laser. This procedure is called spectral selection and is schematically shown in fig. 3.5.

However, the inhomogeneous broadened absorption line is only as smooth as depicted as in the figure when a very large number of molecules is present. Since it is a superposition of homogeneous lines with widths up to 1000 times narrower than the inhomogeneous line, the real shape shows reproducible fluctuations during a laser scan, depending on the average number of absorbers \bar{N}_H in the probed volume with center frequencies within one homogeneous width of

the excitation frequency. This “spectral noise” which is present on the absorption line, is called statistical fine structure (SFS) [63] and its absolute height scales with $\sqrt{\bar{N}_H}$ (for $\bar{N}_H \gg 1$). Since the observation of SFS precedes the single molecule detection, it is often used as a “test signal” to optimize the experimental setup [64]. Thus, the matrix material has to be chosen in a way, that it offers a slight inhomogeneity for the embedded dopants, resulting in an acceptable inhomogeneous broadening.

3.2.2 Further requirements for single molecule spectroscopy

To fulfill the two basic conditions for SMS, several further requirements have to be met. They concern the design of the experiment and the choice and preparation of the sample. The requirements listed here are universally valid for different guest/host systems and experimental methods, but focus particularly on SMS with TOFs. These requirements represent the optimum conditions for SMS, allowing a high resolution experiment with the best possible signal-to-noise ratio.

sample system The use of a matrix for the molecule allows one to take advantage of inhomogeneous broadening and to increase the photostability of the molecule dramatically. Since the dopants are immobile, it offers a fixed orientation for the dipole moment of the molecule. The dye molecule and the host matrix have to be chosen in a way that doping is possible. For a crystalline host, the sizes and structure of both molecule types should allow the proper growth of doped crystals. The dye molecules have to offer special optical properties: A high absorption cross section for the used wavelength increases the probability to excite the molecule. A dye with a high fluorescence quantum yield yields an intense ZPL. A high fluorescence yield can only be fulfilled if the ISC rates to the metastable triplet state are low. A narrow ZPL can be obtained by a system, where the lifetime of the first excited state S_1 is relatively long. When the transition of the lowest electronic transition is placed in the mid-visible, standard tunable single-frequency dye laser can be used.

sample preparation A high sample quality, especially crystal quality is decisive for a low electron-phonon coupling between the dopant and the matrix. The latter reduces the width of the ZPL and can have a positive influence on the photostability of the dye molecule. Keeping the sample small with low dopant concentrations allows one to spatially select single molecules. Small samples are particularly important for spectroscopy with TOFs, since they only minimally effect the light guiding ability of the TOFs. However, too small crystals have a negative effect on the photostability of the dye and the crystal quality in general.

experimental design A tunable narrow-band excitation laser allows efficient spectral selection. To maximize the signal-to-noise ratio, the fluorescence light has to be collected efficiently from the single molecule and guided with low losses to a sensitive detector with low dark counts. Since the emitted fluorescence from the molecules is collected with the TOF, the wavelength of the fluorescence light should be significantly different from the excitation wavelength so that the latter can be suppressed by appropriate spectral filtering. Keeping the excitation intensity below the saturation intensity avoids power broadening and the

generation of noise by scattered light. The possibility to cool down the whole sample to cryogenic temperatures leads to small homogeneous linewidths.

3.2.3 Properties of a molecule as a single photon source

Fluorescence intensity autocorrelation

The ultimate identification of a single molecule as a single quantum emitter involves the investigation of the statistical behavior of its emitted light. All intra- and intermolecular dynamics are reflected by the time distribution of the emitted light. For an analysis of the light emission statistics of a single molecule, the emitted stream of photons and its fluctuations have to be carefully recorded. This yields the fluorescence intensity autocorrelation for two light fields [65]

$$g^{(2)}(\tau) = \frac{\langle I(t) \cdot I(t + \tau) \rangle}{\langle I(t) \rangle^2} \quad (3.40)$$

with

$$\langle I(t) \cdot I(t + \tau) \rangle = \lim_{T \rightarrow \infty} \frac{1}{T} \int_0^T I(t) I(t + \tau) dt \quad (3.41)$$

where t is the point in time when the intensity $I(t)$ is measured. An autocorrelation function measures if a variable at the time t has an influence on the variable at a later time $t + \tau$. For the description of the photon statistics of a single molecule, the number of emitted photons $n(t)$ per detection interval Δt corresponds to the intensity $I(t)$. The probability to detect a pair of photons emitted by the molecule in time intervals $[t, t + dt]$ and $[t + \tau, t + \tau + d\tau]$ is proportional to the probability $P(S_1, t)$ and the conditional probability $P(S_1, t + \tau | S_0, t)$ that the excited singlet state S_1 is populated at the time t and at the time $t + \tau$, respectively. Here, conditional probability means, the probability for the molecule to be found in S_1 at time $t + \tau$ after it was in S_0 at time t . When the first emitted photon is detected, the molecule is projected into the ground state S_0 and the occupation probability of state S_1 at time τ becomes $P(S_1, t + \tau)$. All photons are emitted from S_1 and after an emission, the molecule can be found in S_0 . Thus, the expression for $g^{(2)}(\tau)$ becomes

$$g^{(2)}(\tau) = \frac{P(S_1, t) P(S_1, t + \tau | S_0, t)}{P(S_1, t)^2} = \frac{P(S_1, t + \tau | S_0, t)}{P(S_1, t)} \quad (3.42)$$

The occupation probability can be expressed with the help of the matrix element ρ_{22} of the optical Bloch equations (cf. eqn. 3.25) and the fluorescence intensity correlation becomes [66]:

$$g^{(2)}(\tau) = \frac{\rho_{22}(\tau)}{\rho_{22}(\infty)} \quad (3.43)$$

The optical Bloch equation for a 3-level system can be solved analytically using a Laplace transformation and the population of the excited state $|2\rangle$ is obtained [54]:

$$\rho_{22}(\tau) = \frac{\Omega^2}{2} \left[\frac{k_{31}\Gamma_2}{\lambda_1\lambda_2\lambda_3\lambda_4} + \sum_{i=1}^4 \frac{(\lambda_i + k_{31})(\lambda_i + \Gamma_2)}{\lambda_i(\lambda_i - \lambda_j)(\lambda_i - \lambda_k)(\lambda_i - \lambda_l)} \exp(\lambda_i \tau) \right] \quad (3.44)$$

with λ_i as the roots of a fourth degree equation, which is not given here and can be found in literature [54]. For single molecules in a solid, one can distinguish between two different cases for short and long separation times τ :

short times, $\tau \rightarrow 0$ A molecule performs radiative transitions between its electronic levels. Therefore it can only emit one photon at a time and it has to be excited again before a further photon can be emitted. This nonclassical phenomenon is called antibunching and the correlation for successive photons has a minimum for $\tau = 0$. Since antibunching only occurs for a single quantum emitter and is covered by averaging effects even for a small ensemble of single emitters, it is a direct proof of working with a single molecule. For short times τ when the triplet state is negligible, the function $g^{(2)}(\tau)$ can be approximated by the expression [67]

$$g^{(2)}(\tau) = 1 - B \exp\left(-\frac{(\Gamma_2 + k_{21})\tau}{2}\right) \left[\left(\frac{\Gamma_2 + k_{21}}{2\Omega}\right) \sin(\Omega\tau) + \cos(\Omega\tau) \right] \quad (3.45)$$

with $\Gamma_2 = 1/T_2 = 1/2T_1 + 1/T_2^*$ as the dephasing rate, $k_{21} = 1/T_1$ as the fluorescence rate and the on-resonance Rabi frequency Ω . Possible stray light results in $g^{(2)}(0)$ different from zero, which is accounted by the additional factor B in the equation. The autocorrelation function $g^{(2)}(\tau)$ shows a correlation dip, as expected for antibunching. At low temperatures, when pure dephasing can be neglected and for low excitation intensities ($\Omega \ll \Gamma_2$) eqn. 3.45 reduces to [67]

$$g^{(2)}(\tau) = 1 - B \exp(-3/4 \cdot k_{21}\tau) \left[\left(\frac{\Gamma_2 + k_{21}}{2\Omega}\right) \sin(\Omega\tau) + \cos(\Omega\tau) \right] \quad (3.46)$$

and the width of the correlation dip where the function dropped to $1/e$ is approx. the lifetime of the excited state S_1 . Near the antibunching, eqn. 3.45 shows Rabi oscillations which are damped with the dephasing rate Γ_2 .

long times, $\tau \gg T_1$ For long times τ much bigger than the lifetime T_1 , the triplet state cannot be neglected any more. After the Rabi oscillations are damped, a decay of the normalized correlation function follows and $g^{(2)}(\tau)$ reaches one. The decay is caused by triplet transitions: Although very rare, once a transition from S_1 to T_1 is performed, no further fluorescence can be observed as long as the triplet state is populated. After decaying back to the ground state S_0 via the emission of a phosphorescence photon, the molecule can be excited again. This results in bunches of fluorescence photons when the molecule is cycling through the singlet states $S_0 \rightarrow S_1 \rightarrow S_0$, separated by dark intervals when the triplet state is occupied. The triplet lifetime $\tau_T = 1/k_{31}$ is the average duration of a dark interval. This temporal behavior of a single molecule photon emission is schematically shown in fig. 3.6. For times τ within a bunch the probability for a further photon is higher than outside the bunch, thus leading to $g^{(2)}(\tau) > 1$. The triplet state T_1 consists of two unpaired electrons and even without an external magnetic field, their magnetic dipole-dipole interaction leads to a split of the triplet state into three spin sublevels T_x , T_y and T_z (zero field splitting) [68]. For molecules with D_{2h} - symmetry¹ like terrylene, which is

¹Arises from mirroring the dihedral group in the horizontal plane.

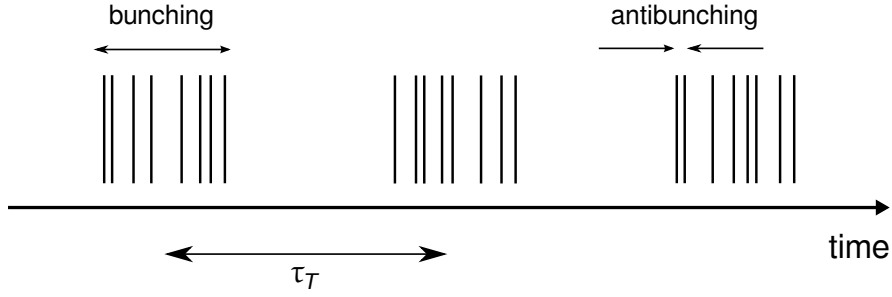


Figure 3.6: Schematic of the photon statistics of a single molecule. The emitted photons are plotted as vertical bars against the time. The separation between two bunches of photons is the triplet lifetime τ_T . For details see text.

used in this work (cf. sec. 3.3), the spins in the sublevels are polarized perpendicular to the spin axes, which coincide with the symmetry axes of the molecule, e. g. the spin of T_x is polarized in the y - z plane. Furthermore, for planar aromatic hydrocarbons both in-plane levels T_x and T_y have similar decay rates, while the one of T_z is significantly different. For a single terrylene molecule in p-terphenyl, like used in this work, for temperatures above 17.5 K the normalized correlation function decays exponentially and at 5 K a bi-exponential decay with typical time constants of $\lambda_1 = 490$ MHz and $\lambda_2 = 3075$ MHz can be found [69]:

$$g^{(2)}(\tau) = 1 + C_1 \exp(-\lambda_1 \tau) + C_2 \exp(-\lambda_2 \tau) \quad (3.47)$$

with the decay rates λ_1 , λ_2 and contrasts C_1 , C_2 . The short-lived component of this decay is associated with an unresolved combination of spin sublevels T_x and T_y and a long-lived component attributed to the sublevel T_z [70]. The decay rate λ depends weakly on the intensity of the excitation light I but strongly on the depopulation rate of the triplet state k_{31} [69, 71].

Experimentally, the fluorescence autocorrelation is measured by dividing the photon stream emitted by a single molecule by a 50 : 50 beam splitter and guiding both streams to two photon counters. The counters record each photon and the time of arrival and the separation times can be calculated later. The use of two photon counters allows to overcome the dead time of each counter. Fluorescence antibunching has been first observed with sodium atoms [72]. The first single molecule antibunching was realized for pentacene in p-terphenyl crystal by Moerner et al. [73].

3.3 Sample systems

During the last decades, several different systems of guest-dye and host-matrices were investigated. For many of them, high-resolution, low-temperature SMS has been performed. In sec. 3.2.2, the requirements for single molecule spectroscopy were listed. For the guest molecule, investigations so far concentrated on large aromatic hydrocarbons (AHCs) with the lowest

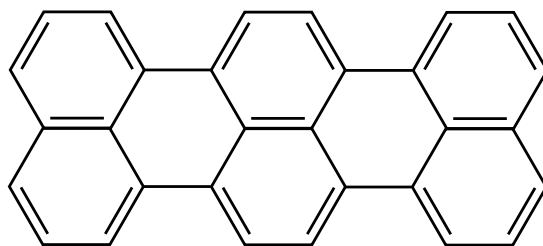


Figure 3.7: Structure formula of terrylene.

electronic transition in the visible spectrum of light, easily reachable for tunable dye lasers. The host-matrices can be divided into three groups, namely single crystals (e. g. p-terphenyl, naphthalene, anthracene), polymers (e. g. polyethylene, polystyrene, polymethyl methacrylate) and Shpolskii matrices (e. g. hexadecane, tetradecane, nonane). Shpolskii matrices are frozen solutions of n-alkanes, which are solvents for the dopant at room temperature but crystallize at low temperatures [74]. In general, crystal hosts offer the most stable environment for embedded molecules and spontaneous spectral diffusion is rare, depending only on defects in the host structure. For low temperatures ($T \leq 2$ K) when dephasing is negligible (cf. sec.3.1.4) the linewidth is only lifetime limited. Polymers as amorphous hosts show fast changes in the local structure which leads to spontaneous as well as light driven line shifts. Furthermore, even at low temperatures, linewidths of embedded dyes don't reach the narrowness of the other host systems and vary from molecule to molecule [75, 76]. For Shpolskii matrices, in some cases a light driven shifting has been observed. Altogether, crystals are the favored host system for SMS [47]. In this work, terrylene is used as a dye and p-terphenyl as a host molecule. This combination is well known and a vast number of measurements has been performed, e. g., on pressure effects [77], the travelling of terrylene molecules along cracks within the crystal [78], fluorescence lifetime measurements [79], optical switching [80], Stark-shift measurements [9], persistent hole burning [81] and the observation of quantum jumps [82].

3.3.1 Terrylene as a fluorescent dopant

The dye terrylene ($C_{30}H_{16}$) is, as part of the rylen-dyes, an aromatic hydrocarbon. It consists of three naphthalene molecules and the structure can be seen in fig. 3.7. The size of the molecule is 1.36×0.67 nm² [42]. In Shpolskii matrices, the transition dipole moment of the lowest singlet electronic transition and the vibronic bands has found to be oriented along the long molecular axis [83].

The quantum yield Φ_f has not been directly measured for terrylene, but for tetra-tert-butyl-terrylene in dioxane, which serves as a structural analog. It has been found to be 0.7 at room temperature [84].

The spectral characteristics of terrylene depend strongly on the surrounding environment. For terrylene in two different solutions, the absorption and fluorescence properties are shown in fig. 3.8. While fig. 3.8(a) shows the fluorescence and the fluorescence excitation in dichloromethane (DCM), fig. 3.8(b) shows the absorbance spectrum for a solution of terrylene and p-

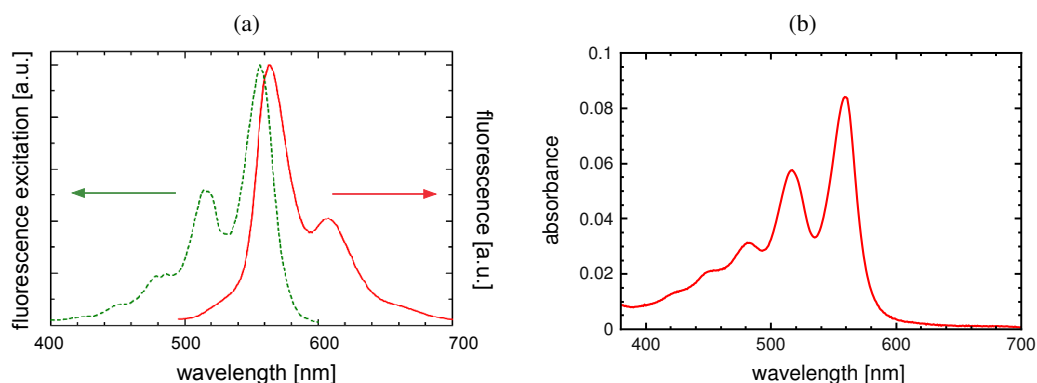


Figure 3.8: Spectral characteristics of terrylene in different solutions. **(a)** shows the fluorescence excitation (green dashed line) and the fluorescence (red solid line) spectrum of terrylene in dichloromethane at room temperature (adapted from [85]). **(b)** shows the UV/Vis absorption spectrum of an unsaturated solution of 2.3 mg/ml p-terphenyl and 46 ng/ml terrylene in toluene. Measured by W. Scholdei at the MPI for Polymer Research in Mainz with a spectral resolution of 1 nm [86].

terphenyl in toluene. Since p-terphenyl does not absorb in this spectral range, it has no contribution to the absorbance. In general, the shape of the absorbance in toluene has a similar shape as the fluorescence excitation in DCM. The spectral position of the peaks agrees well and the solvent shift shows only a difference of about 2 nm. The absorption for terrylene ranges from approximately 400 nm to 600 nm with a maximum at approximately 560 nm. According to the Franck-Condon principle and the transition probabilities in molecules, the fluorescence of terrylene in DCM shows the expected mirror symmetry of the fluorescence excitation. Since the optical properties of a fluorescence dopant like terrylene are highly influenced by the surrounding medium or the matrix, resp., further optical characteristics will be presented with respect to the matrix material used in this work.

3.3.2 p-Terphenyl as a single crystal host

Since the first investigation of terrylene in p-terphenyl as a sample system by S. Kummer et al. [87, 88], it has become a system widely used for single molecule spectroscopy. Different approaches were made to produce samples of this guest-host system suited for single molecule spectroscopy: E. g. growth of very pure terrylene-doped p-terphenyl crystals via sublimation of a mixture of these two compounds [42, 87, 88] or spin-coating of extremely thin doped crystals on a substrate [89]. For bulk measurements crystals were grown from the melt using standard Bridgman techniques [42].

p-Terphenyl

Terphenyls are a group of a central benzene ring with two adjacent phenyl rings. The different orientations of the phenyl rings allow three different isomers with the same chemical for-

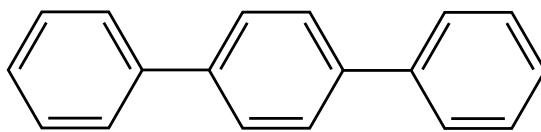


Figure 3.9: Structure formula of p-terphenyl.

mula ($C_{18}H_{14}$), but different spatial structures. Depending on the position of the substituted phenyl rings with respect to the benzene ring, the different isomers are denoted ortho-, meta- or para-terphenyl (with their abbreviations o-, m- or p-terphenyl, resp.). While o-terphenyl and m-terphenyl have an angled structure, p-terphenyl is of linear shape, cf. fig. 3.9. At room temperature, it forms a white, solid, crystalline powder. The molar mass is 230.31 g/mol and the density 1.23 g/cm³. P-Terphenyl has a melting point of 213 °C and a boiling point of 404 °C.

The size of one p-terphenyl molecule is $1.36 \times 0.48 \text{ nm}^2$ [42]. At room temperature, two opposing forces are responsible for the structure of single p-terphenyl molecules, e. g., in the gas phase: the delocalized π -electrons tend to a planar molecule structure, while steric effects of the hydrogen atoms in the phenyl rings, close to the benzene ring, cause a twisted configuration [90]. In this twisted formation, the M-axis, defined by the short axis of the molecule's outer rings and the M'-axis, defined by the short axis of the molecule's central ring are tilted against each other by an angle α . Contrastingly, in a crystal lattice, additional forces reduce the freedom of movement for the central benzene ring to $\pm 13.3^\circ$ [91]. However, at room temperature this movement is so fast and random, that in X-ray and neutron diffraction experiments, the molecules show a planar structure. P-terphenyl forms crystals of monoclinic structure, by aligning the long molecular axis parallel to the c -axis of the crystal, cf. fig. 3.9 and fig. 3.10(a). The lattice constants are $a = 8.1 \text{ \AA}$, $b = 5.6 \text{ \AA}$ and $c = 13.6 \text{ \AA}$ with b as the direction of the monoclinic axis and the monoclinic angle (between a and c) $\beta = 92.1^\circ$ [92]. Every unit cell contains two molecules and their angle between the b -axis and the previously defined M-axis is alternating $\Theta = \pm 32.7^\circ$, cf. fig. 3.10(a). However, it has been observed [93] and theoretical calculated [94], that p-terphenyl crystals undergo a phase transition at a temperature of 193.3 K from a monoclinic to a triclinic unit cell. Due to the reduction of the temperature, the dynamic, unorganized twisting of the central ring is frozen to defined positions, leading to two equiprobable domains α and β , which are related by a symmetry plane [93]. The molecules in the same site have an opposite orientation in these two domains. At low temperatures, the triclinic unit cell contains four molecules at four inequivalent positions ($M_1 - M_4$). These positions are defined by different angles of the axis formed by the outer phenyl rings of the molecule (M-axis) with respect to the central benzene ring (M'-axis) yielding 15.1° (M_1), 18.0° (M_3), 23.3° (M_4) and 26.3° (M_2) [41, 47], cf. fig. 3.10(b). The long axis of the p-terphenyl molecules are still parallel to each other. It is convenient to describe the crystal structure at low temperatures with a pseudo-monoclinic unit cell containing eight molecules. The lattice constants are then $a' \sim 2a$, $b' \sim 2b$ and $c' \sim c$ with b' as the direction of the (pseudo-) monoclinic axis and the (pseudo-) monoclinic angle $\beta' = 92^\circ$ [93]. The growth of the crystal predominantly takes place in the a - b plane, leading to thin, platy crystal flakes. P-terphenyl shows different polarizabilities, depending on the molecular axis. It is larger for the c -axis and results in birefringence of the crystal.

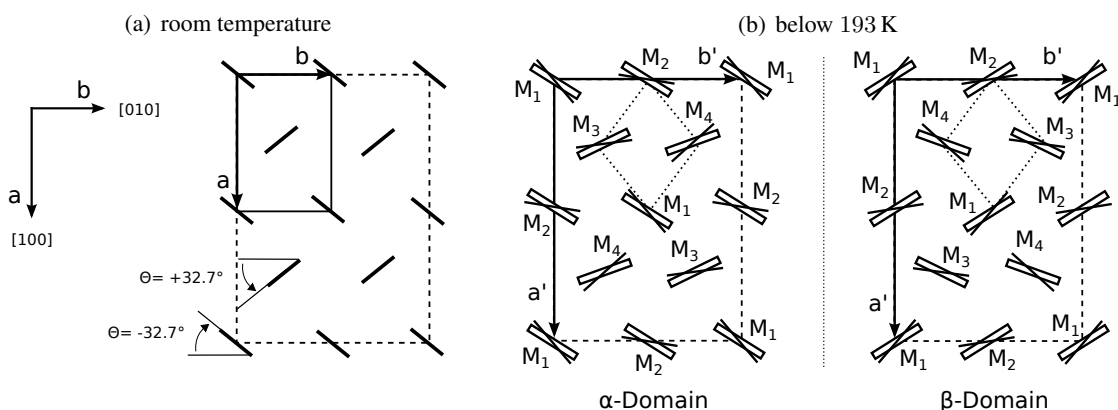


Figure 3.10: Schematic of the crystal structure of p-terphenyl at (a) room temperature and (b) below 193 K. Each figure shows the projection of the short axis of the molecule's outer rings (M-axis) onto the a/b - (resp. a'/b' -) plane. At room temperature, the molecules are planar (in average), showing two possible angles Θ between the b -axis and the molecular plane. The monoclinic unit cell, containing two inequivalent molecules is shown by the solid line. At low temperatures, the central's ring twisting is frozen to defined positions, leaving four inequivalent positions ($M_1 - M_4$). The pseudo-monoclinic unit cell contains now four inequivalent molecules, shown by the dashed line. The dotted line highlights the triclinic unit cell. The central ring and its position is drawn with a thin bar (M' -axis), the outer rings are drawn with a thick bar (M -axis). Below 193.3 K, two equiprobable domains α and β exist, related by a symmetry plane. For more details, see text. Adapted from [47,96]

At room temperature, the refractive indices for the corresponding axes were determined as $n_a = 1.584$, $n_b = 1.687$ and $n_c = 2.004$ for a wavelength of 546.1 nm, but they are unknown for low temperatures [95].

For the electronic singlet state, p-terphenyl shows an absorption in the ultraviolet spectral range ($\lesssim 325$ nm, with a maximum at about 275 nm). The fluorescence is in the spectral range between approx. 315 nm and 460 nm with a maximum at 340 nm. The absorption band for the triplet states is moved to a maximum at 460 nm, becoming negligible above 520 nm [97]. Crystals of p-terphenyl show no sign of self-absorption [98].

In this work, where terrylene is used as a dopant for p-terphenyl, for fluorescence and absorption measurements, the visible spectral range is of interest. In this region, p-terphenyl is transparent and no spectral crosstalk with the embedded guest molecule exists.

P-terphenyl embedded terrylene

In spite of the size differences of p-terphenyl and terrylene, p-terphenyl crystals can be doped with terrylene via different chemical methods. For low concentrations (less than 0.01 %) it has been shown, that the doping of p-terphenyl with terrylene does not change the intermolecular interaction energy and no significant deviation of the monoclinic or triclinic crystal structure exists [99]. Each of the previously introduced four inequivalent sites can host one (two) ter-

rylene molecule(s). Waiving possible crystal defects, simple size comparisons between both molecules suggest, that one terrylene molecule would replace two p-terphenyl molecules within the unit cell of the lattice. Contrastingly, it has been concluded that at low temperatures, one p-terphenyl molecule is replaced by one terrylene molecule, aligning the long axis of terrylene roughly parallel to the one of p-terphenyl. The transition dipole moment of terrylene is oriented along the long axis of the molecule. [41]. Since crystal growth is not an equilibrium process, a substitution of two p-terphenyl molecules is possible, but improbable [96]. Each site provides a slightly different surrounding for the embedded dopant, resulting in an inhomogeneous shift of the transition frequencies of terrylene. Therefore, the replacement of one p-terphenyl molecule by one terrylene molecule within the four crystal sites leads to four different optical sites, which have been designated as X_1 to X_4 . Since the optical sites are named according to their spectral position starting with the lowest wavenumber, the indices i of crystal sites M_i and optical sites X_i differ. In each site, the angle between the long axis of the molecule and the a -axis is slightly different with 99.8° (M_4, X_2), 100.5° (M_2, X_3), 102.6° (M_1, X_4) and 103.6° (M_3, X_1) [96]. This leads to a small variation of the dipole moment of terrylene depending on each site. Although the benzene rings of neighboring naphthalene units show a small twist against each other, resulting in a torsional strain of roughly 4° , the entire molecule is centrosymmetric in a mono-substituted site. [96]. The insertion sites show different photostabilities and spectral dynamics for the substituted terrylene molecules: Molecules at X_2 and X_4 are extremely stable and survive up to 10^{12} optical cycles without bleaching at 1.8 K and their fluorescence count rates under full saturation are very high, ranging between $3 \times 10^6 \text{ s}^{-1}$ and $6 \times 10^6 \text{ s}^{-1}$ [42], even at room temperature, optical cycle rates up to 8×10^6 and saturation count rates of $2.1 \times 10^6 \text{ s}^{-1}$ are possible [100]. At X_1 instead, they show reversible, photo-induced blue-shifted frequency jumps to a site designated XY, which can be followed by further blue shifted jumps to sites designated XY', XY'' and XY'''. A reset to the initial site XY can be achieved by heating the sample above 40 K. The excitation of a molecule in X_1 leads to a change in the geometry of terrylene and, triggered by that, an adjacent p-terphenyl molecule might modify the orientation of its central phenyl ring, resulting in a new environment for this dye molecule and therefore a new optical site XY with a new absorption wavelength. The additional jumps to further optical sites can be explained by a reorientation of the central phenyl ring of other p-terphenyls in the next surrounding solvent shell [80]. Molecules in the optical site X_3 show spontaneous jumps of the absorption lines to unknown positions on a very short timescale, which is why this site is viewed as unstable. If one terrylene substitutes two p-terphenyl molecules, four different geometric combinations of neighboring p-terphenyls are possible, denoted as C_1 to C_4 , as analogous to M_1 to M_4 in fig. 3.10. Each geometric combination can consist of two non-equivalent p-terphenyl molecules ($M_1 - M_4$), leading to eight additional terrylene sites named p_1 to p_8 with red-shifted absorption lines. Terrylene in these di-substitution sites exhibits a slightly different deformation with angles between the long axis of the molecule and the a -axis between 98.9° and 106.1° . Molecules in these sites are not centrosymmetric anymore, since the inter-naphthalene twists vary [96]. A summary of the assignment of optical and crystal sites to their spectral origin and their optical properties can be seen in tab. 3.2.

In fig. 3.11 fluorescence spectra for single terrylene molecules in a p-terphenyl crystal can be seen. The spectra (a) and (b) were measured at room temperature for excitation wavelengths

optical site	crystal site	wavelength [nm]	wavenumber [cm ⁻¹]	photostability
X ₁	M ₃	580.38	17230	induced jumps
XY		579.44	17258	induced jumps
XY'		579.11	17268	induced jumps
XY''		578.80	17277	induced jumps
XY'''		578.54	17285	induced jumps
X ₂	M ₄	578.50	17286	very stable
X ₃	M ₂	578.27	17293	unstable
X ₄	M ₁	577.90	17304	very stable
$p_1 - p_8$	C ₁ - C ₄	589.97 - 609.76	16400 - 16950	

Table 3.2: Designations of the optical and crystal sites of terrylene in p-terphenyl and their absorption wavelength with the according photostability. [42, 96]. For details see text.

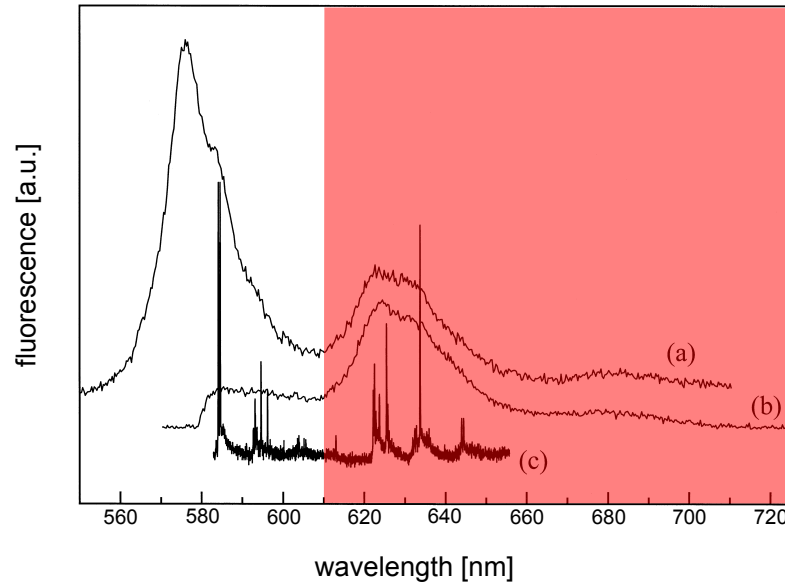


Figure 3.11: Fluorescence spectra of single terrylene molecules in p-terphenyl. **(a)** is obtained at room temperature and an excitation wavelength of 488.0 nm. **(b)** is also measured at room temperature but with an excitation wavelength of 568.2 nm. The origin of the broad peaks at room temperature can be recognized by comparing it with the spectrum for liquid helium temperatures in **(c)** which was excited at the 0-0' electronic transition. The red underlying marks the range investigated in this work. Taken from [100]. For details see text.

of 488.0 nm and 568.2 nm, respectively. In spectrum (a), three broad peaks can be distinguished at spectral positions of 578 nm, 630 nm and 685 nm. The difference between (a) and (b) is due to acquisition method. These three bands correspond to the vibrational lines in the low temperature fluorescence spectrum in (c). While the broad peak at 578 nm is the envelope of the purely

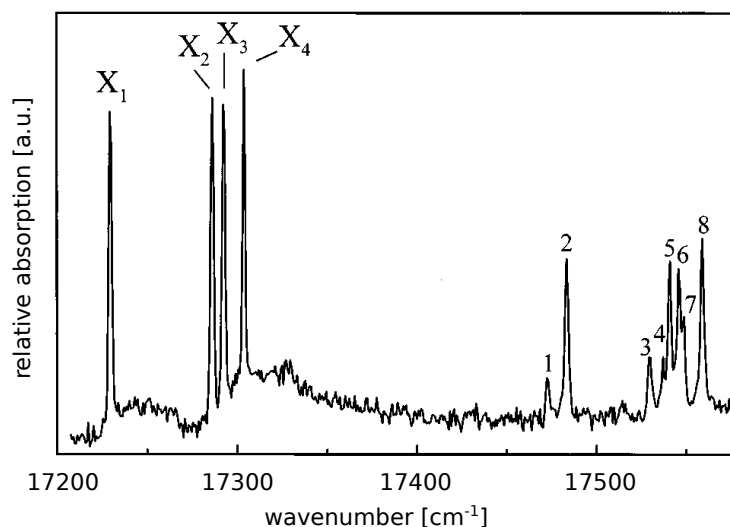


Figure 3.12: Ensemble absorption spectrum of a 5 mm thick terrylene in p-terphenyl Bridgman crystal (concentration: 10^{-4} mol/mol) at a temperature of 4.2 K, taken from [42]. X_1 to X_4 denote the optical site of terrylene within the crystal, numbers 1 to 8 vibronic transitions. For details see text.

electronic transition and the first vibronic transitions, the broad peak at 625 nm consists only of vibronic peaks. The poorly pronounced broad peak at 685 nm is supposedly a combination of low- and high energy vibronic transitions [100]. The red underlying marks the range which is investigated in this work due to constraints of the optical setup.

Fig. 3.12 shows a typical ensemble absorption spectrum of p-terphenyl embedded terrylene at 4.2 K. The crystal was produced from the melt via the Bridgman technique. The four strong absorption lines correspond to the four optical sites X_1 to X_4 , each representing a pure electronic transition ($0-0'$). They are of equal intensity which shows, that the terrylene molecules are homogeneously distributed between the four crystal sites. Each ZPL is accompanied by two vibronic transitions, located at about 245 cm^{-1} to 248 cm^{-1} and 255 cm^{-1} to 258 cm^{-1} shifted to higher wavenumbers: lines 1 and 2 belong to X_1 , lines 3 and 4 belong to X_2 and so on. The optical sites p_1 to p_8 are not shown here.

The lifetime-limited linewidth of a single terrylene molecule embedded in a p-terphenyl crystal is independent of the optical site and varies between 30 MHz to 55 MHz for low power excitation and below 2.2 K [42]. However, the lifetime-limited linewidth has been predicted to be around 42 MHz [101]. The ISC rates have been determined as $k_{23} = 1.9 \times 10^3 \text{ s}^{-1}$ and $k_{31} = 2.0 \times 10^3 \text{ s}^{-1}$ as the population and depopulation rate of the triplet state, respectively. With the experimentally determined total decay rate of S_1 as $k_{21} = 3.1 \times 10^8 \text{ s}^{-1}$ and eqn. 3.2, the triplet quantum yield becomes $\Phi_T = 6.1 \times 10^{-6} \text{ s}^{-1}$ [87]. The lifetime of the excited S_1 state has been determined for a single molecule below 4 K via intensity correlation measurements to be 3.6(4) ns [67]. For the determination of the saturation intensity, the collection efficiency and the orientation of the molecular dipole with respect to the polarization of the incident light have

to be taken into account [102]. Most values for the saturation intensity of a single terrylene molecule in p-terphenyl in the site X₂ at a temperature of 1.4 K determined experimentally and given in literature vary slightly around 24(5) W cm⁻² [87, 88]. This is due to the fact that the excitation light was polarized almost perpendicular compared to the molecular dipole. For a parallel polarization the saturation intensity has to be found much lower between 81 mW/cm² and 94 mW/cm² [103].

Experimental setup

For the experiments presented in this thesis, different experimental setups have been used and different ways of producing and investigating dye-doped organic crystals on a TOF have been tested. The optical setup for exciting the molecular sample and analyzing the emitted fluorescence light is the same for all experiments. Additional setups containing the TOF can be easily spliced to the optical setup. These additional setups are the sublimation cell for growing doped crystals directly on the TOF (explained in sec. 5.1) and the cryostat which allows the spectroscopic investigation of a molecular sample at cryogenic temperatures.

4.1 Optical setup

The complete optical setup is schematically depicted in fig. 4.1. The optical setup consists of two independent parts: the excitation path (yellow beam path) includes all elements used for the excitation of samples adhered to the TOF and the fluorescence path (red beam path) includes the elements for collecting and analyzing the fluorescence light from the sample on the TOF. Both parts are connected to the TOF on the same side, which reveals the perfect properties of a TOF for the excitation of a surface adsorbed sample and the simultaneous collection of the emitted fluorescence. Some parts are only used for a specific task of the experimental process. It is explicitly mentioned when they are used and, for clarity, corresponding components are encircled with a dashed gray line.

4.1.1 Excitation path

All laser light used for the experiments in this thesis is generated by a ring dye laser (Matisse DS, Sirah, not shown in the setup) using rhodamine 6G as a dye. It is pumped by a diode-pumped solid-state laser (Verdi V10, Coherent) with a wavelength of 532 nm and an output power of 10 W. The dye laser is tuneable from 560 nm to 615 nm and, using 10 W of pump power, has a maximum output power of 1.8 W at a wavelength of 575 nm. It has a linewidth of 250 kHz [104]. The wavelength is determined with a fiber-coupled wavelength meter (WS-6/600, High Finesse)

and constantly logged in a datafile. The light is guided via a 47 m long polarization-maintaining fiber (PM-460-HP, Nufern) from the laser laboratory to the experiment table. Although the fiber is polarization-maintaining and the polarization of the light is carefully adjusted with a half-wave-plate to match the axis of the fiber, polarization fluctuations of the light exiting this fiber cannot be completely avoided. Therefore, after being guided to the experiment table, the laser light passes a half-wave-plate and a polarizing beam splitter. The polarizing beam splitter passes light with parallel polarization, while light with perpendicular polarization is reflected and not used. The half-wave-plate allows one to rotate the polarization-axis of the light by any desired angle and therefore to choose how much of the light should have a parallel polarization, passing the beam splitter. Any fluctuation in polarization, e. g., caused by the polarization maintaining fiber, will be converted into intensity fluctuations. Furthermore, the stability of the laser intensity is logged at the point of the intensity stabilization with a photodiode (PD 1) via a beamsplitter (BS). To compensate for fast intensity fluctuations down to 1 Hz, an acousto-optic modulator (AOM, Crystal Technology 3080-125) is used and a telescope is reducing the diameter of the laser beam to fit its entry slit. A polarizer (Pol), allows one to set the linear polarization of the light to a predefined angle. When passing a standard glass plate (GP), a small fraction of the excitation laser light is coupled into a standard glass fiber (460HP, Nufern) which is directly or via a 2x2 single mode fiber optic coupler (FC632-90B, Thorlabs) spliced to the TOF. Depending on the measurement or sample preparation, the TOF is placed in different environments, like a sublimation cell, a cryostat, or a laminar flow box. On the opposite side of the TOF, a powermeter (Coherent, FieldmaxII-TO) is placed to observe and log the transmitted power during measurements (PD 2). At position PD 3, the power inside the fiber guided to the TOF is controlled with either a single photon counting module (SPCM; AQHR-14-FC, Excelitas Technologies) or a powermeter.

4.1.2 Fluorescence path

The fluorescence path is used for collecting and analyzing the light that is emitted by the sample and that is coupled into the nanofiber in the direction opposite to the direction of propagation of the excitation light. The spectral characteristics can be investigated with a grating spectrometer (Shamrock SR-303i, Andor Technology) that is equipped with a CCD camera (Newton DU920N-BR-DD, Andor Technology). Three different gratings allow spectral resolutions of 0.4 nm/pixel, 0.2 nm/pixel, and 0.1 nm/pixel [105]. To investigate the time-dependent behavior of the emission of an emitter, which is crucial for the identification of the single-particle character (cf. ch. 3.2.3), a Hanbury-Brown and Twiss setup, is included in the optical setup. Once a sample on the TOF is excited and emits fluorescence, a fraction of the light is coupled back into the fiber. This backscattered fluorescence is then detected by the spectrometer or one SPCM as indicated in fig. 4.1. After leaving the TOF, most of the light passes the glass plate. For some measurements, a SP filter (650 nm) blocks background and stray light in the beampath. A 50/50 beamsplitter splits the light for two interferometer arms. Two identical long pass filters (610 nm or 650 nm) in front of the fiber couplers further suppress unwanted wavelengths in the beampath. Two single mode fibers (460HP, Nufern) guide the light from the fiber coupler to two SPCMs. Both counting modules generate a TTL-pulse for every photon detection. Each TTL-pulse is provided with a time tag by and processed further with a computer. Since the correlator is based

on a field programmable gate array (FPGA), with a clock speed of picoseconds. Instead of using the intensity interferometer, one beam path can be coupled to the spectrometer instead.

Collection efficiency

Since the spectrometer and the SPCMs are both fiber coupled, the collection efficiency for both detection methods depends on the transmission property of the TOF (η_{TOF}), the same optical elements passed by the fluorescence light (η_{optic}) and the same coupling efficiency into the fiber, which is coupled to one of the detectors (η_{fiber}). The coupling efficiency into each detector is different for SPCM (η_{col1}) and spectrometer (η_{col2}), as well as the corresponding detection efficiency (η_{SPCM} resp. η_{CCD}). If the 2x2 fiber coupler is used, η_{TOF} has to be corrected with the corresponding value of the split ratio. All efficiencies depend differently on the wavelength of the transmitted light and the overall collection efficiency can be estimated by

$$\eta(\lambda) = \eta_{\text{TOF}}(\lambda) \cdot \eta_{\text{optic}}(\lambda) \cdot \eta_{\text{fiber}}(\lambda) \cdot \eta_{\text{col1/2}}(\lambda) \cdot \eta_{\text{SPCM/CCD}}(\lambda) \quad (4.1)$$

The transmission property of the TOF used in this work is wavelength independent for the spectral region of interest and has been measured to be around $\eta_{\text{TOF}}(\lambda) \approx 0.95$ (cf. sec. 2.1.2, especially fig. 2.9). The transmission efficiency of the optical path η_{optic} is also roughly wavelength independent for the spectral region of interest between 610 nm resp. 630 nm and 650 nm and consists mainly of the transmission of the glass plate (0.92) and the beam splitter (0.45). The mirrors contribute only weakly with a reflection of 0.99 each. The LP and SP filters have a transmission efficiency of 0.95 each. This yields $\eta_{\text{optic}} \approx 0.35$. The coupling into the single mode fiber for the used fiber coupler (60FC-4-M12-33, Schäfter + Kirchhoff) depends strongly on the quality of manual coupling. Since the coupling was checked before the measurements, it should approx. be above $\eta_{\text{fiber}} \gtrsim 0.3$. The overall detection efficiency of the spectrometer has been determined experimentally to be $\eta_{\text{col2}} \cdot \eta_{\text{CCD}} = 0.01$ for a wavelength of 600 nm [106]. For the fiber-coupled SPCM, the detection efficiency for a wavelength of 650 nm is $\eta_{\text{col1}} \cdot \eta_{\text{SPCM}} = 0.60$ [107]. This yields overall detection efficiencies of $\eta \approx 6\%$ when using the SPCM and $\eta \approx 0.1\%$ for using the spectrometer at 600 nm.

4.2 Cryostat

Cooling a molecular sample down to cryogenic temperatures is necessary for spectroscopic measurements of narrow lifetime limited single molecule linewidths. A simple liquid helium bath cryostat is used which assures sample temperatures down to round about 2 K, but usual working conditions are 4.4 K. It consists of a main liquid helium reservoir, in which the sample chamber can be inserted. The liquid helium reservoir is surrounded by a concentric evacuated shield, which is constantly evacuated with a rotary vane pump (Alcatel 1012A) during all measurements. There is a concentric liquid nitrogen reservoir within the evacuated shield which is used for precooling of the helium environment and shielding the helium reservoir from room temperature radiation. In order to perform measurements at cryogenic temperatures with a TOF, a new sample rod and sample chamber had to be designed. To keep the light guiding abilities of a fiber, it should not be in direct contact with the liquid helium but still have a good thermal

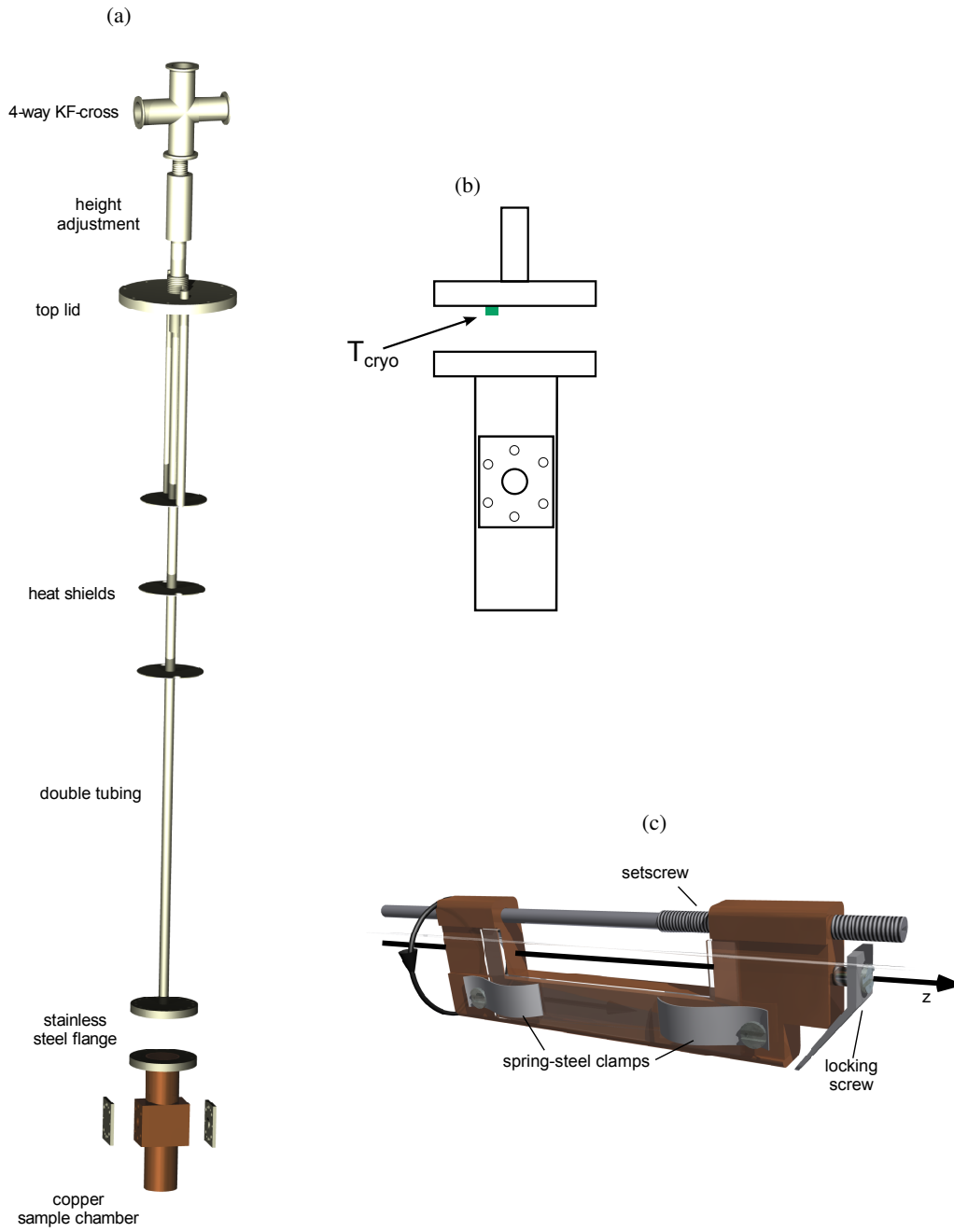


Figure 4.2: Schematic of the complete sample rod (a), a detailed sketch of the sample chamber with the position of the temperature sensor (b) and a schematic of the fiber mount (c). (a) and (c) are adopted from [86, 106]. See text for details.

contact to grant a sufficient cooling to a cryogenic temperature by allowing one to evacuate the sample chamber and to add a small amount of helium gas which ensures the thermal contact. A schematic of the complete sample rod can be seen in fig. 4.2(a). Via the top lid, the rod is fixed and sealed above the liquid helium reservoir. Outside the cryostat there is a height adjustment which allows one to adjust the vertical position of the sample chamber by about 10 cm. The 4-way KF-cross on the top enables several connections to the sample volume. They are used for an overpressure safety valve, a mechanical or a pirani pressure gauge, an electric feedthrough for the temperature sensor inside the sample chamber, a fiber feedthrough for the fiber going in and out, and a valve for evacuating or flooding the sample volume with helium buffer gas. The top of the sample rod is connected with a thin double stainless steel tubing with the sample chamber. The double tubing allows one to keep the electric wires and the fiber separated, which makes assembling the sample rod easier. It is surrounded by three copper heat shields to minimize the heat transfer via radiation. The sample chamber is attached at the bottom end of the tubing, via a stainless steel flange which can be opened for access to the chamber. It is sealed with a pure indium wire with a diameter of 1 mm. This ensures a high-vacuum proof connection, even when immersed in liquid helium. In fig. 4.2(b) a sketch of the sample chamber can be seen. The silicon diode temperature sensor (Lake Shore DT-670-CU-1.4L) is attached to the upper flange and the temperature is continuously monitored (Lake Shore 211 temperature monitor). The bottom part of the sample chamber is made of oxygen-free copper which grants a more efficient thermalization with the liquid helium bath. Two flanges are positioned face to face on the side of the sample chamber, allowing one to connect it to a vacuum chamber for free beam deposition of molecules on a sample. The flanges can be opened when sample rod and sample are assembled to flush the volume with helium gas and thereby remove all remainders of air. The lids for the two flanges are made of stainless steel and are sealed with the same pure indium wire. Due to heat transfer between the sample chamber and the warm environment, the minimum temperature in helium bath mode (with no additional evaporative cooling) is about 4.4 K.

The TOF, manufactured and fixed on a holder as described in sec. 2.1.2, is placed on an additional fiber mount to ensure proper positioning and thermalization of the fiber. It is displayed in fig. 4.2(c). The main body is made of oxygen-free copper and has full contact with the fiber holder, when fixed. Two spring-steel clamps are used for fixing and adjusting the fiber holder and allow for movement between fiber holder and fiber mount due to thermal expansion and contraction. The fiber mount is inserted into the sample chamber along the labeled z-axis with the locking screw on the top. With the set-screw, the vertical position can be adjusted while the locking screw is used for retaining the fiber mount inside the sample chamber.

Thermal expansion and contraction of the TOF

When inserted on the fiber mount into the sample chamber, the TOF is fixated with magnets on the fiber holder schematically shown in fig. 2.7(a). Cooling down a TOF on an iron holder can be very challenging because of the different expansion and contraction behaviors. The linear thermal expansion coefficient α_L describes how the length L of an object with a defined material

part	material	temperature range (K)	range of $\alpha_L (10^{-7}/\text{K})$
TOF	Silica	4 ... 283	-0.2 ... 4.4 [108, 109]
Fiber holder	Iron	4 ... 283	0.14 ... 118.5 [110]

Table 4.1: Linear thermal expansion coefficients for the TOF and different materials in contact with the TOF

part	thermal behavior	$\frac{\Delta L}{L}$	absolute length change
Fiber holder	contraction	-3.3×10^{-3}	-231 μm
Fiber	contraction	-1.2×10^{-4}	-8 μm
Fiber	expansion	2.3×10^{-4}	16 μm

Table 4.2: Maximum possible absolute length change for fiber and fiber holder with a length of $L = 70 \text{ mm}$ during cooling down to 4 K.

changes with a change in temperature T :

$$\alpha_L = \frac{1}{L} \frac{dL}{dT} \quad (4.2)$$

Due to the linear geometry of fiber and sample holder, the volumetric thermal expansion coefficient α_V can be neglected. Table 4.1 shows the thermal expansion coefficients for the material of the fiber holder and the material of the TOF for a wide range of temperatures. The magnets are not taken into account since they are not connected with each other and they only affect a small part of the optical fiber outside the tapered region. Silica, the main constituent of the TOF, has a positive expansion coefficient for temperatures above round about 150 K and therefore experiences a contraction during cooling in this temperature range. Below 150 K the expansion coefficient is negative and results in an expansion of the material. The maximum negative thermal expansion coefficient is $-8.1 \times 10^{-7}/\text{K}$ at round about 58 K. Iron, the material of the holder has a positive expansion coefficient for the whole temperature range and undergoes only a contraction during cooling. To estimate the maximum stress for the TOF, the expansion of fiber holder and TOF have to be taken into account, based on the different expansions during cooling. Because silica shows both expansion and contraction during cooling but for different temperature ranges, two cases have to be taken into account: Contraction of the iron holder with a contraction of the TOF and contraction of the holder with an expansion of the TOF. The change in length can be calculated by

$$\frac{\Delta L}{L} = \int_{T_1}^{T_2} \alpha_L(T) dT \quad (4.3)$$

where T_1 is the initial temperature while T_2 is the final temperature of the cooling process. With a distance $L = 70 \text{ mm}$ between the magnets holding the TOF and the values for α_L from table 4.1, the maximum possible absolute length change can be calculated by using the maximum thermal expansion coefficient for the cooling for the whole temperature range, see table 4.2.

As it can be seen, the contraction of the fiber holder dominates during the cooling process. Combined with the length change of the fiber, the maximum possible overall contraction for

the TOF would be between 239 μm and 215 μm . This is a small contraction and can easily be compensated by pre-stretching the TOF after the pulling process.

Another difficulty for cooling down fibers to cryogenic temperatures is the influence of the buffer gas which is used inside the cryo rod to ensure the thermalization of the TOF and the sample. As described in detail in [106], it turned out that a too high helium buffer gas pressure can result in a complete loss of fluorescence signal and transmitted power. To avoid this effect, a very small amount of buffer gas is used (approx. 10 mbar at 4.4 K). This is enough to ensure the cooling of the sample but avoids any loss of transmission.

Manufacturing of dye-doped crystals

Different approaches by different groups were performed to produce terrylene doped p-terphenyl crystal for SMS: they have been produced from solution, from the melt or from the gas phase with diverse methods like spin-coating [89], cold-finger sublimation [42, 87, 88] or Bridgman techniques [42]. Terrylene doped p-terphenyl crystals from solution for the use with a TOF were already produced in this group before [38, 86, 106], but did not lead to SMS. For SMS with a TOF, three requirements have to be fulfilled: as for other investigation methods, the quality of the crystal has to be such that the dopants are incorporated in a very regular crystal structure causing no additional phonon coupling and leading to narrow fluorescence lineshapes. Also, the dopant concentration has to be low enough that inhomogeneous broadening allows the spectral selection of single molecules. Additionally, for SMS with TOFs, the size of a crystal has to be small enough so that the light guiding abilities of the fiber are still granted when the crystal is interfaced with the TOF.

We tested different sample preparation techniques like cold-finger sublimation and crystal growth from oversaturated solution concerning their suitability for the combination of TOFs and SMS and will present the results in this chapter. The focus was set on high crystal quality and a production and deposition method on the TOF which ensures a high transmission through the fiber. To control both parameters, the crystal is excited through the fiber and the transmitted power is directly checked during and after the deposition: the bigger the crystal, the bigger the power drop. The crystal quality can be controlled only indirectly: the emitted fluorescence light from the sample is collected and investigated spectrally. While the shape of the spectrum allows conclusions on the crystal quality, the intensity of the signal is an indicator for the dopant concentration. A large number of measurements were performed on the two manufacturing methods. Only a representative selection will be given here. All spectra presented in this chapter were recorded with a spectral resolution of 0.4 nm.

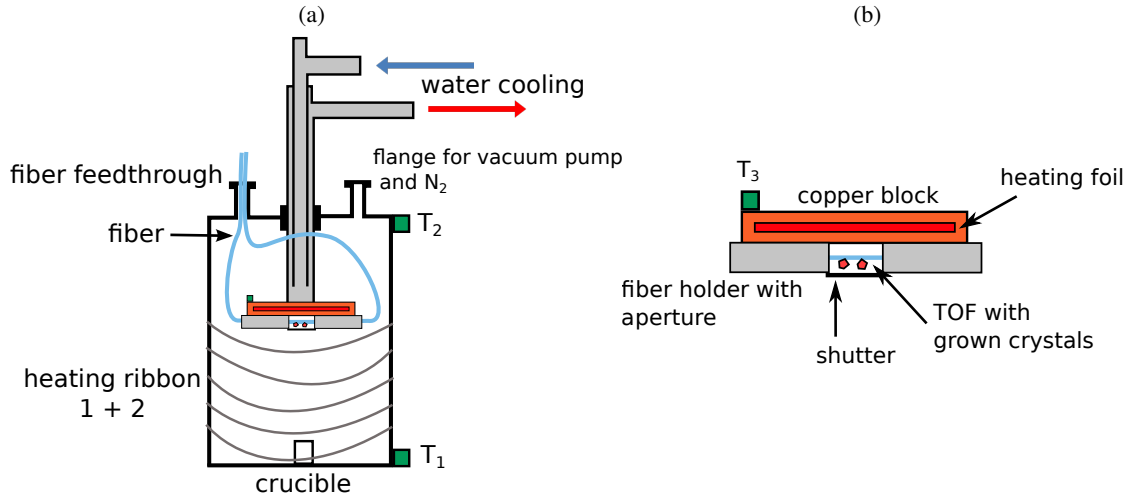


Figure 5.1: Schematic of (a) the cold-finger sublimation cell and (b) the fiber holder. Details see text.

5.1 Cold-finger sublimation

A common method for growing pure crystals of superior quality as well as crystals with different doping grades is the use of a sublimation cell. To have full control over the resulting crystal sizes, dopant concentrations, and crystal qualities, the terrylene doped p-terphenyl crystals are directly grown on a TOF. The sublimation process offers many degrees of freedom such as temperature of the crucible and the different parts of the sublimation cell, the pressure inside the cell, and the moment of stopping the sublimation process.

5.1.1 Sublimation cell

The cell used in this work was designed following earlier work of sublimation growth of terrylene doped p-terphenyl crystals [61, 111]. However, compared to other setups where the grown crystals have to be carefully harvested for further investigations, the main objective for the construction of the sublimation cell here was to be able to grow crystals directly on the TOF and to control the growth process spectroscopically. Furthermore, the growth process should be stoppable to avoid too big or too many crystals growing on the TOF, which would deteriorate the transmission of light significantly.

A schematic of the sublimation cell can be seen in fig. 5.1. The body of the cell consists of a vacuum tube with CF60 flanges on the top and bottom for easy access to the inside cell and with several CF16 flanges on the top lid for different connections: a fiber feedthrough connects the TOF inside the cell via a glass fiber with the optical setup (at the position of the TOF in the optical setup in fig. 4.1) and the spectrometer, another flange leads to a valve which allows to evacuate the cell with a vacuum scroll pump (Oerlikon, Scrollvac SC15D) as well as to introduce nitrogen gas for the sublimation process. Further flanges, which are not shown, guide electrical

wires for temperature sensor T_3 , the crucible, and the heating foil of the fiber holder into the chamber. The concentric KF flange has a squeeze-type gasket for the water cooling in- and outlet. On the side of the cell, two temperature sensors (Omega, type K, 5TC-KK-KI-20-1M) are mounted, T_1 at the bottom and T_2 at the top. Two heating ribbons are wrapped around the whole chamber, the top, and bottom flange. This allows the creation of a temperature gradient with different temperatures at bottom and top. On the bottom flange, inside the cell, a small crucible is placed, which can be filled with a mixture of molecules to sublime. On the end of the height-adjustable water cooling, a massive copper block is attached, which contains a PTFE heating foil (Omega, Kapton KHLV) and another temperature sensor T_3 . This allows one to set the exact temperature for the fiber holder, which is mounted below the copper block. In early experiments, the complete TOF was exposed during the whole sublimation. Later, an adjustable aperture covered the TOF from three sides that could be opened between 0 mm to 10 mm, thus reducing the section of the TOF where sublimation can take place. Additionally, a mechanical shutter was introduced. It is operated from outside the cell and can be used to completely cover the TOF at any moment during the sublimation to stop the growth process immediately.

5.1.2 Preparing the molecule raw material

In a first step a molten mixture of terrylene (LianYunGang Henrychem Science, purity $\geq 98\%$, used as obtained) and p-terphenyl (Sigma-Aldrich, purity $\geq 99.5\%$, used as obtained) was prepared. The terrylene concentration was set to $c_{\text{terrylene}} = 2.6 \times 10^{-4} \text{ g/g}$. The melting was carried out in an oven under a constant nitrogen pressure of 1 bar. In addition, the nitrogen gas was constantly exchanged during the whole process. To avoid sublimation and evaporation of the organic material, the crucible was covered. To ensure that all material was melted, the final temperature of the process was kept at 280°C for 10 min, which is above the melting point of terrylene ($T_{\text{melt}} = 70^\circ\text{C}$) and p-terphenyl ($T_{\text{melt}} = 213^\circ\text{C}$). To reach this final temperature, the oven was heated slowly from room temperature to 25°C within 10 min and kept at this temperature for 1 min. The heating to 160°C took again 10 min and the temperature was kept for 10 min at this point to stabilize and to equably disperse within the mixture. It took again 10 min to rise the temperature to 240°C , followed by a 5 min rest. The final temperature was reached again in 10 min. After cooling down and crystallization, the mixture was carefully pestled into a fine powder to ensure homogenization. This powder was kept closed and used for all sublimation processes without further treatment. Lower terrylene concentrations were realized by adding more p-terphenyl later on.

5.1.3 Sublimation of doped crystals on the TOF

Before a TOF or the prepared raw material could be placed in the crucible inside the sublimation cell, an attentive cleaning of the cell was required. Initially, the chamber and all parts inside were swiped with ethyl alcohol ($\text{C}_2\text{H}_6\text{O}$, Merck uvasol), which is a solvent for p-terphenyl. Additionally, the cell was closed and heated above 240°C for an hour with the vacuum pump running. After the cleaning process, the TOF could be attached to the fiber holder inside the cell. Three ways were used to sublime crystals on the fiber: the TOF directly exposed during the whole sublimation process, an aperture with a fixed width of slit between 1 mm to 2 mm which

had to be installed together with the TOF, and a fixed aperture in combination with a mechanical shutter surrounding the TOF from three sides which could be operated from outside stopping the growth process immediately. The height of the TOF above the bottom flange was usually kept at the highest possible position at 23 cm. When the shutter was used, it was kept close till the temperature of the sublimation cell and its contents had reached an equilibrium. Before the heating was initiated, the chamber was evacuated to a pressure of 10^{-2} bar and then filled with an initial nitrogen pressure of 0 mbar to 100 mbar. During the whole process, excitation light with a wavelength of 578.5 nm was coupled into the TOF and the fluorescence was coupled back to the spectrometer according to the optical setup in fig. 4.1. The transmitted power was controlled with a powermeter. After the desired temperatures were reached, the shutter was opened and the fluorescence was recorded. The fluorescence signal is an indicator for the quality of the sublimated crystals. While a broad fluorescence indicates a high dopant concentration and/or a bad crystal quality, a drop in the transmitted power indicates big and/or misplaced crystals in the taper transitions.

Sublimation on bare TOF

In a first attempt, the possibility of growing crystals via sublimation directly on TOF was investigated. The cell was prepared as explained above and several runs with different parameters were performed while the sample was excited via the fiber and the transmission was checked. The parameters that could be changed were: nitrogen pressure, final temperature of crucible, temperature of cell, temperature of fiber holder. However, these parameters only had a small influence on the shape of the fluorescence spectrum and the transmitted power was always completely lost during the sublimation process. To check if this was a general sublimation problem or just in combination with the growth on a TOF, some crystals from inside the cell were carefully harvested after the process finished. During the harvesting it could be seen, that the crystal growth started with small crystals on the surface of contact to the sublimation cell with an increasing size further away. A crystal sample was investigated with a scanning electron microscope (SEM). The resulting image can be seen in fig. 5.2(a). The crystal consists of several smaller crystals, the surface of contact to the sublimation cell is on the top. Some crystals are even arranged perpendicularly (white stripes in the middle) to the main crystal.

To investigate the spectral properties of a sublimated crystal independently of growing them on a TOF, a suspension of isopropanol and harvested crystals was dropped on the TOF of a new fiber until a crystal was adhered. The spectrum is compared to the one obtained during the growth of crystals directly on the TOF and can be seen in fig. 5.2(b). Both spectra were recorded with an excitation power of 122 nW prior to sublimation. During the sublimation the excitation power was not recorded. The spectra remained stable over time, indicating that the terrylene molecules were well incorporated in the crystal matrix. No power was transmitted through the fiber after the sample was grown or deposited, respectively. The growth conditions for both samples were the same with maximum temperature of the cell and the crucible of 170 °C and a nitrogen background pressure of 50 mbar. The fluorescence signal of the harvested crystal (black spectrum) shows a similar shape as the spectrum of a single terrylene molecule in a p-terphenyl crystal (cf. fig. 3.11) with a pronounced but broad peak at 645 nm. In contrast, the crystal sublimated on the TOF (red spectrum) has no pronounced peak at this position. The

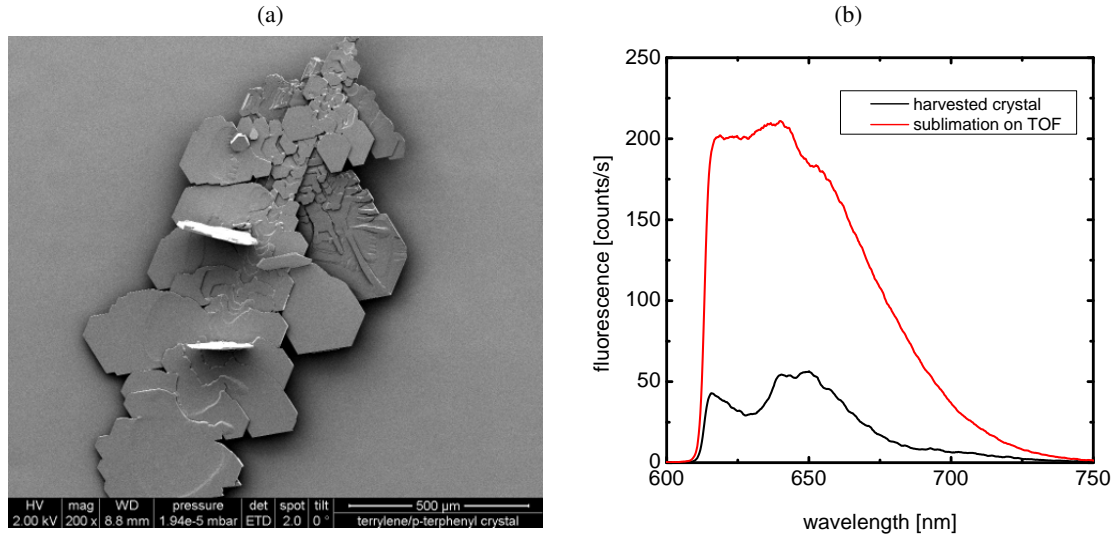


Figure 5.2: (a) shows a SEM image of a terrylene doped p-terphenyl crystal grown via sublimation. Direction of growth is along the long axis from top to bottom. (b) shows two background corrected spectra of terrylene doped p-terphenyl crystals on a TOF. The black spectrum is obtained by depositing a sublimation crystal on the TOF. The red spectrum is obtained by sublimating crystals directly on the TOF. In both cases, the crystal was excited with a wavelength of 578.5 nm and a transmitted power of 122 nW prior to sublimation. A LP filter suppresses the fluorescence below 610 nm. For details see text.

fluorescence signal consists of one broad peak with a shoulder at the position of the pronounced peak. The harvested crystals grew on the fiber holder and copper block which could result in slightly different growth temperatures compared to the TOF. This would directly affect the crystal quality.

Sublimation with aperture

Crystal growth in the taper transitions will cause disturbances for the mode conversion from the untapered fiber to the waist, which will lead to the excitation of higher transverse guided modes. The latter will then be lost in the waist region which acts as a single mode filter, thereby reducing the TOF transmission. To avoid the problems resulting of crystals growth on this part of the TOF, apertures were constructed and mounted, leaving only a slit with the width of 1 mm to 2 mm on the side of the fiber opposite the crucible. Again, several runs with different sublimation parameters were performed while the fluorescence and the transmitted power was observed. The parameters changed were the ones before and they had only a slight influence on the shape of the fluorescence signal. All sublimations resulted in a complete loss of transmitted power. Also measurements of the sublimated fiber were performed with a SEM to investigate the shape and the growth area of the crystals. In fig. 5.3 a SEM image of a fiber sublimated with an aperture and the corresponding fluorescence can be seen. Different SEM images show that

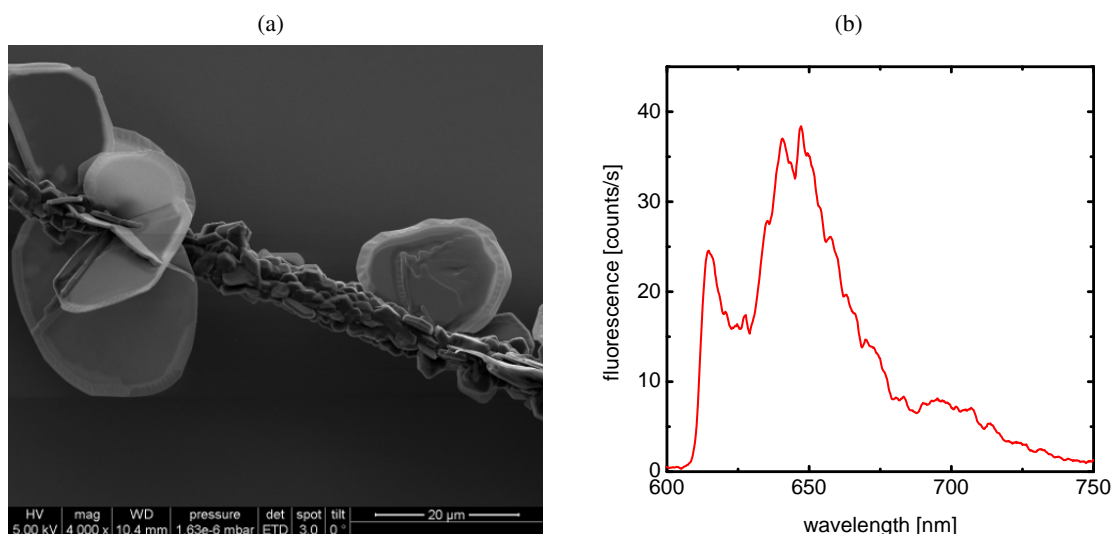


Figure 5.3: (a) shows a SEM image of the crystals grown on a TOF via sublimation with the use of an aperture. (b) shows the corresponding background corrected fluorescence, excited with a wavelength of 578.5 nm and a transmitted power of 82 nW prior to sublimation. A LP filter is cutting the fluorescence below 610 nm. See text for details.

the use of the aperture strongly reduces the area of growth on the fiber to the length of the waist. The SEM image in fig. 5.3(a) shows the fiber completely covered with crystals with the size of a few micrometers. Some bigger crystals grow on top of the layer of small crystals with a size up to 20 μm. The differences of the shape of the fluorescence signal, compared to the previous measurements, can be seen in fig. 5.3(b). The pronounced peak at 645 nm is similar to the one of a single terrylene molecule in p-terphenyl at room temperature (cf. fig. 3.11) and similar to the harvested sublimated crystal adhered to the TOF (cf. fig. 5.2(b)).

Sublimation with aperture and shutter

To avoid the complete overgrowth of the TOF during the sublimation process, a mechanical shutter was introduced to the sublimation cell. It could be operated from outside at any moment of the process and shielded the TOF completely from further contact with the molecular vapor. As before, several runs with different sublimation parameters were performed, which did not seem to affect the shape of the fluorescence. The shutter was kept closed until the desired temperature of cell and fiber holder was reached. Even before opening it, a slight increase in fluorescence and a drop in the transmitted power was observed, indicating that the shutter was not shielding the TOF completely. For mechanical reasons, this could never be entirely avoided. After opening the shutter, the fluorescence and the transmitted power was monitored and, before the transmitted power dropped to zero, the shutter was closed and the heating of all components was switched off. Probably because of the non-hermetic closure of the shutter or

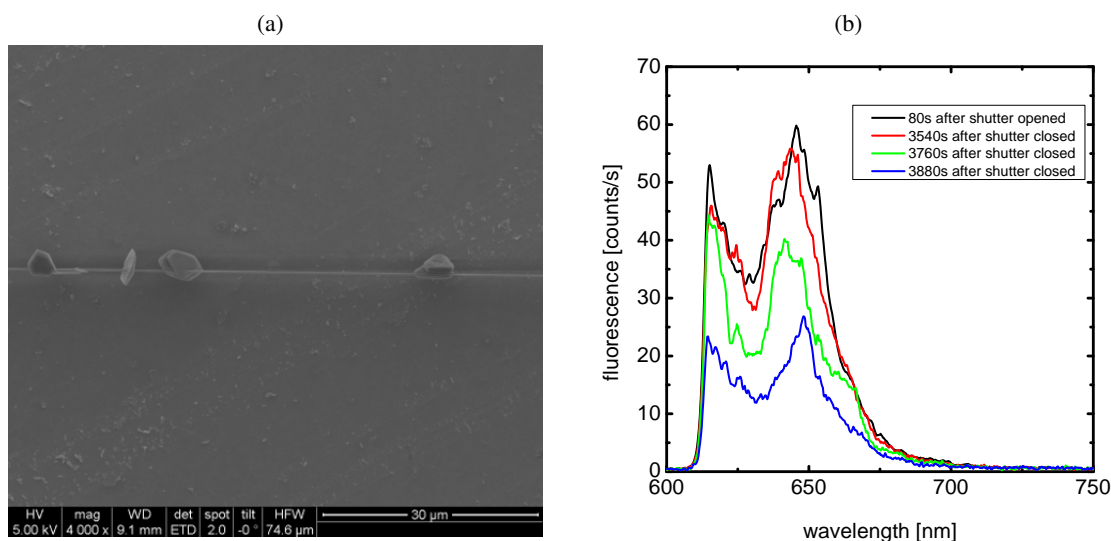


Figure 5.4: (a) shows a SEM image of the crystals grown on a TOF via sublimation with an aperture and the use of a shutter. Note that the detail shown here is not part of the waist, but a part of the transition with a diameter of 369 nm. (b) shows the corresponding background corrected fluorescence at different times after opening and closing the shutter, excited with a wavelength of 578.5 nm and a transmitted power of 49 nW prior to sublimation. A LP filter is cutting the fluorescence below 610 nm and the aperture has a slit width of 2 mm. See text for details.

the slow process of cooling down the cell¹, a further drop in the transmitted power and a change in the shape of the fluorescence spectra was observed in most cases. In fig. 5.4, a SEM image and fluorescence spectra of crystals sublimated on a TOF while using a shutter can be seen. The SEM image in fig.5.4(a) shows several crystals up to a size of 6 μm, grown with irregular distances of each other on the TOF. Between the crystals no growth can be seen. Note that the SEM image does not show the exact center of the TOF, as the latter has a diameter of round about 320 nm, while the part of the TOF shown here has a diameter of 369 nm. This size is measured on the SEM image. The changes in the fluorescence signal during the sublimation process and after the shutter was closed can be seen in fig. 5.4(b). The cell and the crucible was heated up to about 140 °C before the shutter was opened. It took about 80 s until the fluorescence signal stabilized (black curve). After 150 s the shutter was closed and all heaters of the sublimation cell were switched off. Even when the shutter was closed, the transmitted power kept dropping and the fluorescence signal changed its shapes and intensity. After almost 1 h, no power was transmitted anymore and the fluorescence signal still changed intensity and shape. The blue curve is where it stabilized. During the growth process, the shape of the fluorescence spectra had some similarities with a typical ensemble/single molecule spectrum of terrylene in p-terphenyl at room temperature (cf. fig. 3.11) during the growth process (cf. the green curve), the fluorescence

¹After 3 h of cooling down from an initial temperature of 170 °C, the temperature of the cell was round about 50 °C.

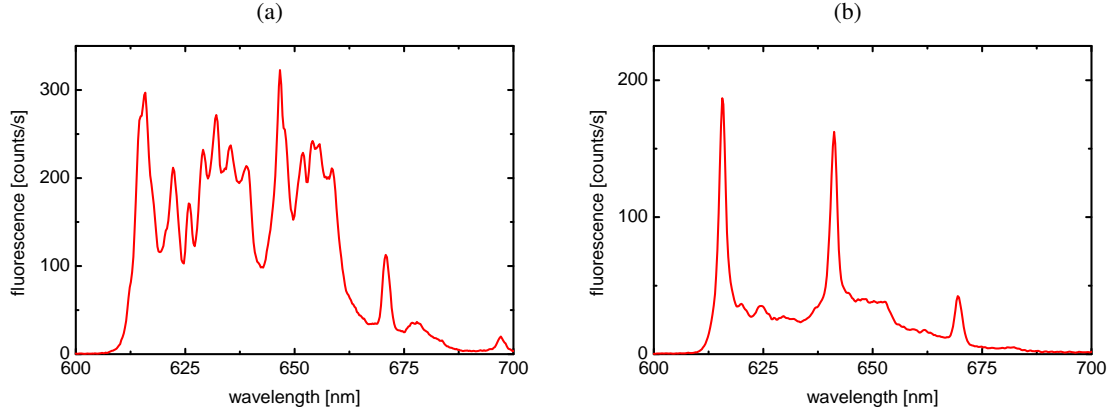


Figure 5.5: Interference fringes in the fluorescence signal during the sublimation process, caused by isolated growth of crystals on the fiber, as seen as in fig. 5.4. The spectra are recorded during the same measurement as the ones in fig. 5.4 at **(a)** 100 s after the shutter was opened and **(b)** 100 s after the shutter was closed. For details see text.

signal for the stable system (cf. the blue curve) shows a rather small peak at 645 nm with no clear double peak structure. The isolated crystal growth on the fiber might lead to interferences which are responsible for some of the additional shoulders in the spectra. A reason for the continued growth after closing the shutter was either the imperfect sealing or a resublimation of grown crystals on the TOF. During some of the sublimations, strong interference fringes in the fluorescence signal were observed, which are illustrated exemplarily in fig. 5.5. It shows two spectra from the same measurement as in fig. 5.4 but after 100 s (fig. 5.5(a)) after opening the shutter and 140 s (fig. 5.5(b)) after closing the shutter. The existence of small particles on the TOF can form a Fabry-Pérot interferometer or etalon. The sublimated crystals with the distance L act like partially reflective mirrors resulting in an optical resonator with distinctive peaks in the transmission spectrum, whose intensity follows the Airy-formula [112]. The distance of the transmission peaks is the free spectral range $\Delta\lambda$. For a TOF with crystals and the light partially inside and outside the fiber, the frequency distance Δf is related to the distance L of the reflecting crystals and the effective refractive index n_{eff} of the TOF(cf. eqn. A.29):

$$\Delta f = \frac{c}{2 \cdot n_{\text{eff}} \cdot L} \quad (5.1)$$

While the irregular peak pattern in fig. 5.5(a) indicates the existence of several reflecting crystals on the TOF, the spectrum in fig. 5.5(b) reveals three sharp peaks whose positions are determined via fits with the Airy-formula at 615.62 nm, 641.18 nm and 669.45 nm. This yields a free spectral range of approx. $\Delta f = 20$ THz. With eqn. 5.1 and $n_{\text{eff}} = 1.19$ for the TOF used here (cf. ch. 2) the distance between the reflecting crystals can be calculated to be approx. $L = 6 \mu\text{m}$. This fits well to the distances between crystals on the TOF for this sublimation, shown in fig. 5.4(a). Note that the SEM image was taken after the complete sublimation process, while the two spectra showing interferences were taken during the crystal growth. Additionally, the finesse $F = \Delta\lambda/\delta\lambda$ with $\delta\lambda$ as the FWHM of a transmission peak can be calculated as

a characteristic of the resonator. With $\delta\lambda \approx 1.6$ nm, the finesse is calculated as $F = 18$ and $F = 14$, resp. Although this is a rather low value for an optical resonator, for a spectroscopic use any interference caused by a resonator is undesirable. Besides the growth of isolated crystals which can lead to interference effects, another limiting effect is that the shutter cannot stop the growth process completely. Thus, with this technique, a TOF with transmission and suitable fluorescence signal cannot be prepared.

5.1.4 Deposition of downsized sublimated crystals

The sublimation method produces crystals of suitable fluorescence signal but the growth directly on the TOF leads to the loss of the transmission properties of the fiber and the occurrence of interference effects. Hence, the possibility of depositing sublimated crystals manually on the TOF was investigated. After sublimation, a small amount of crystals was carefully harvested from the copper block and mixed with isopropanol in a cuvette. Since the harvesting took place after the sublimation cell was cooled down, the crystal were of rather big size. To reduce the size, the cuvette was kept in an ultrasonic bath for times up to 30 min. To remove the crystals of bigger size, different filter papers were used with pore sizes of 7 μm to 12 μm (type Schwarzband), 2 μm to 4 μm (type Blauband) and 0.2 μm . The filtered suspension was then dropped on the TOF until a fluorescence signal could be observed. To investigate the influence of the ultrasonic bath on the crystal structure, SEM images were taken of different filtered suspensions. In fig. 5.6, two SEM images and a fluorescence spectrum can be seen. The effect of the ultrasonic bath in combination with filtering the suspension with filter paper of pore size 2 μm to 4 μm on the crystal size can be seen in fig. 5.6(a). The size is highly reduced according to the specifications of the used filter. In fig. 5.6(b) the evolution of the corresponding fluorescence signal can be seen. The fluorescence signal shows the typical double peak structure at 645 nm, known already from earlier sublimation measurements. The transmitted power is 112 nW prior to adhering the crystal and the crystal causes to drop the transmitted power to 6 %. Note that, in all prior sublimation measurements, a transmission together with a suitable fluorescence could not be established. When observing the evolution of the fluorescence signal, a drop in intensity can be seen, while the shape remains almost the same. The signal is completely lost for all adhered downsized crystals, but, here, the spectrum was stopped to be recorded earlier. Since a well-incorporated terrylene molecule should have a high stability against photochemical processes even under ambient conditions, this indicates a damage in the crystal structure and/or terrylene molecules which are dissolved away from the crystal. This effect was only observed with sublimated crystals treated in an ultrasonic bath and is not a general problem with sublimated crystals, as shown by the measurement of the fluorescence of a sublimated and untreated crystal (cf. fig. 5.2(b)). The mechanical effect of the treatment in an ultrasonic bath on the initial big p-terphenyl crystals can be seen in fig. 5.6(c). It shows two crystals which were kept for about 30 min in the bath. Both show a pronounced damage on the surface and the edges. Together with the observed drop of the fluorescence signal it can be concluded, that an ultrasonic treatment of p-terphenyl crystals effectively downsizes them but also causes mechanical damage in the crystal structure resulting in a reduced photochemical stability of terrylene.

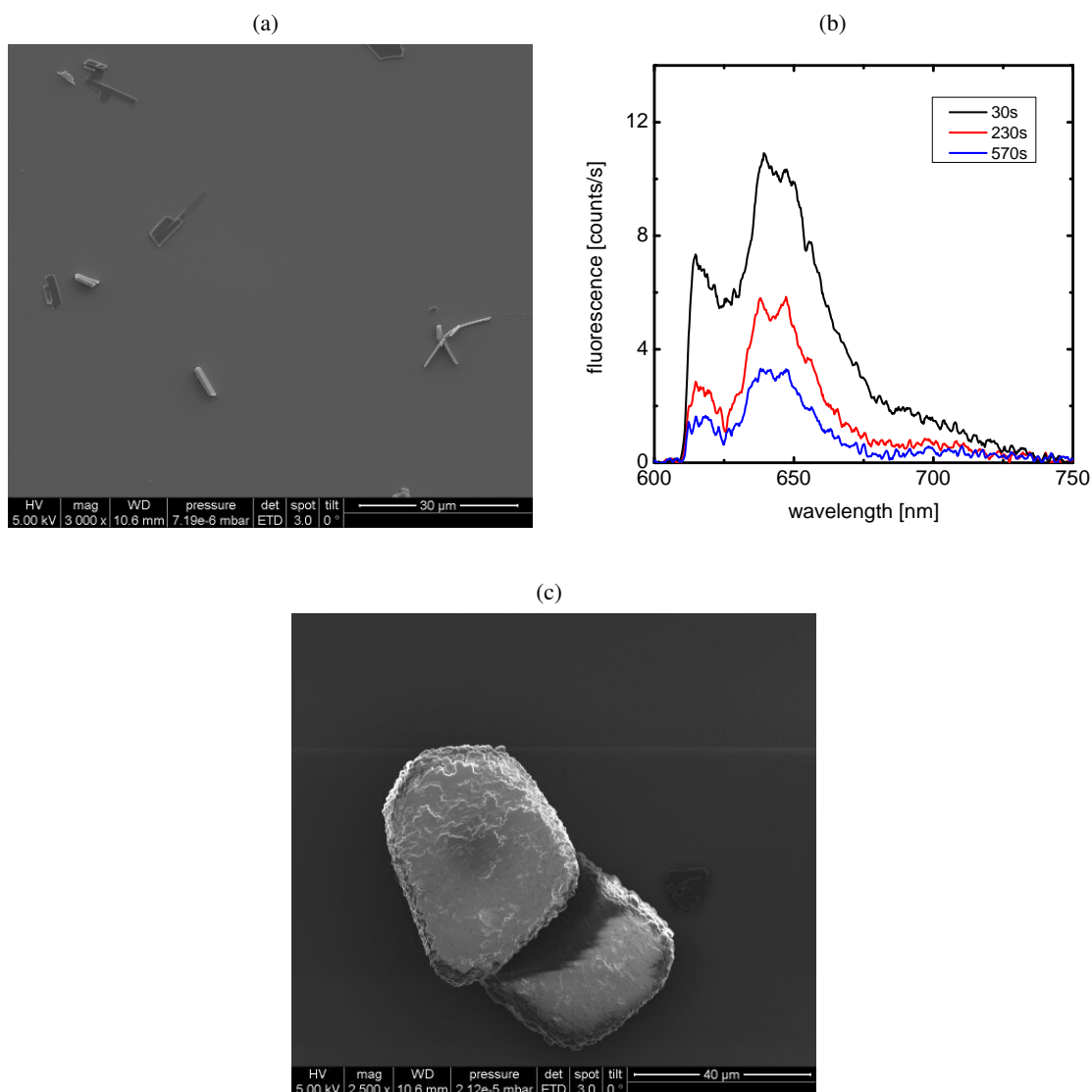


Figure 5.6: Influence of the ultrasonic bath on the size and the spectral characteristics of sublimated crystals. (a) shows the downsized crystals after 30 min in an ultrasonic bath and filtered with filter paper pore size 2 μm to 4 μm . (b) shows the evolution of the corresponding fluorescence between 30 s to 570 s after such a crystal was deposited on the TOF. The excitation wavelength is 578.5 nm and the deposited crystal caused a drop of transmitted power from 112 nW to 7 nW. (c) shows two rather big crystals with visible damage caused by exposure to the ultrasonic bath. For details see text.

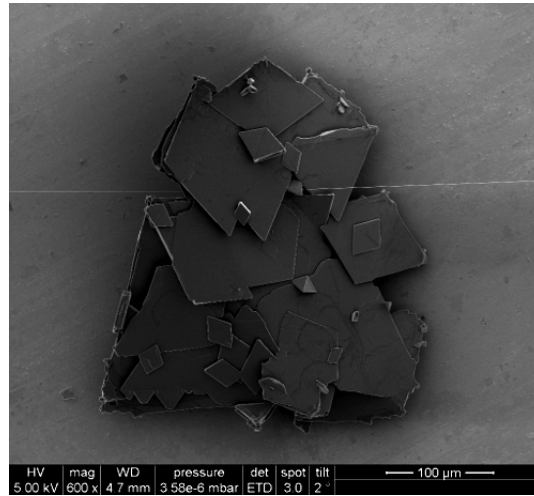


Figure 5.7: SEM image of a terrylene doped p-terphenyl crystal on a TOF. The crystal was produced with the former dropping method used in our group from an oversaturated solution with an initial concentration of the terrylene/p-terphenyl mixture of 2.6×10^{-6} g/g and an oversaturation of 10.53 mg/ml p-terphenyl/toluene. The adhered crystal caused the transmitted power to drop to zero.

5.2 Crystal growth from oversaturated solution

It has been shown in our group that the use of an oversaturated solution compared to an undersaturated solution accelerates crystal growth and that this leads to a better inclusion of terrylene molecules in p-terphenyl [86, 106]. The method of growth and deposition of crystals was to heat an oversaturated solution of terrylene, p-terphenyl and toluene to 80 °C and to start the growth process by cooling the solution within a pipette. Such a drop of solution with grown crystals was then dropped on the TOF. During this procedure, the solution kept crystallizing and this resulted in rather random crystals of unpredictable size, dopant concentration, and quality. Furthermore, the size of the crystal was always so large that no light could be guided through the fiber anymore. It was never possible to grow and deposit crystals with sufficient quality for SMS with this method. In fig. 5.7 such a crystal deposited on a TOF can be seen.

In general, the growth of crystals from an oversaturated solution depends strongly on parameters like pressure, temperature, rate of temperature change during cooling, and surface tension and turbulences of the solution. Since terrylene and p-terphenyl are both involved in the growth process even more parameters arise which have an influence on the dopant concentration in the crystals: the dopant concentration increases if either the initial terrylene concentration is increased or the crystallization speed is increased. The size of such a crystal is mainly determined by the growth time and the oversaturation of the solution. To gain more control over the crystal growth from oversaturated solution compared to earlier work in this group, different modifications of this method were carried out. To ensure the light guiding abilities of the fiber, particular attention was paid to grow small crystals. To achieve the single molecule level, the quality of

the grown crystals needed to be improved significantly.

The oversaturated solutions were always prepared in the same way. Great care was taken during the preparation process to avoid contaminations of the solution and hence of the dyed crystals. The cuvettes were cleaned in an ultrasonic bath in an aqueous detergent (Extran MA02 neutral, Merck) and flushed first with distilled water, then Acetone ($\text{C}_3\text{H}_6\text{O}$, Rotipuran purity $\geq 99.8\%$). The glass pipettes, used for measuring toluene, were rinsed with Acetone only. To prevent dust particles settling on the surfaces of the cleaned pipettes and cuvettes, the drying was carried out under a lab's flow box. The manufacturing process for an oversaturated solution was as follows: a mixture of terrylene (LianYunGang Henrychem Science, purity $\geq 98\%$, used as obtained) and p-terphenyl (Sigma-Aldrich, purity $\geq 99.5\%$, used as obtained) was dissolved in toluene ($\text{C}_6\text{H}_5\text{CH}_3$, Merck uvasol). The solubility of p-terphenyl in toluene is reached for a concentration of about 5 mg/ml at ambient conditions. Heating the solution in an ultrasonic bath at 80°C for about half an hour guaranteed that all molecules were in solution.

5.2.1 Different oversaturations and very low concentrations

A low dopant concentration is an important demand for SMS and relative terrylene concentrations down to 10^{-9} have been successfully used [42]. Relative terrylene concentrations so far used in this group for the initial terrylene/p-terphenyl mixture were only in the order of 10^{-5} and the resulting fluorescence excitation spectra showed rather broad spectral features which indicate a relative high concentration of terrylene molecules that could prevent the observation of single molecules with a TOF [106]. To investigate the general possibility of using lower dopant concentrations for the crystal growth from solution and the possible improvement of highly diluted crystal samples, oversaturated solutions with low concentrations of 10^{-8} g/g terrylene/p-terphenyl and different oversaturations were prepared. The solutions were heated up to 80°C and immediately drawn up with a clean glass pipette. Repeatedly, drops of the crystallizing solution were dripped on the TOF until a fluorescence signal could be obtained. After recording the spectrum, the fiber was cleaned with acetone, and the process was repeated many times. The samples were excited via the fiber with a wavelength of 578.5 nm and a transmitted power of 170 nW prior to adhering the crystal. The fluorescence was recorded with the spectrometer in integration intervals of 10 s. No power transmission through the fiber could be achieved. In fig. 5.8 the highest obtainable fluorescence spectra of both oversaturations are shown. In both cases the fluorescence signal is very broad and continuously ranges from 610 nm (where the LP filter prevents the recording of fluorescence light with lower wavelengths) to 760 nm. The strength of the fluorescence is rather low with a maximum of 7 counts/s for the sample with an oversaturated solution of 18.47 mg/ml p-terphenyl/toluene (fig. 5.8(a)) and even lower with 5 counts/s for the sample with an oversaturated solution of 11.48 mg/ml p-terphenyl/toluene (fig. 5.8(b)). The higher the oversaturation, the faster is the crystal growth and the easier present dopants are incorporated into the crystal. Consequently, the sample with the higher oversaturation (fig. 5.8(a)) shows a more distinct fluorescence signal than the one with the lower oversaturation (fig. 5.8(b)). However, the signal shows only one broad peak. In the spectral range above 610 nm, according to fig. 3.11 one would expect one distinctive peak centered at 630 nm which drops to zero and a second weakly pronounced peak at 685 nm. Both spectra have similarity with the spectra of non-localized terrylene (cf. fig. 3.8(a)). Non-localized terrylene shows a bleaching effect under a

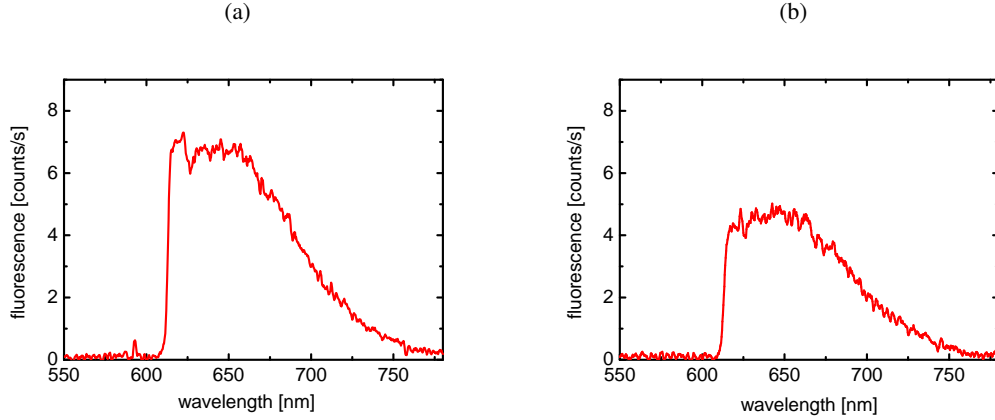


Figure 5.8: Background corrected fluorescence of samples grown from highly diluted terrylene concentrations and an excitation wavelength of 578.5 nm and a transmitted power of 170 nW prior to adhering the crystals. A LP filter cuts the fluorescence below 610 nm. The sample shown in **(a)** results from an initial terrylene/p-terphenyl mixture with a concentration of 2.4×10^{-8} g/g and an oversaturation of 18.47 mg/ml p-terphenyl/toluene. The sample in **(b)** results from a similar initial terrylene/p-terphenyl mixture with a concentration of 2.5×10^{-8} g/g but a lower oversaturation of 11.48 mg/ml p-terphenyl/toluene.

continuous excitation at room temperature. But since the spectra were not recorded long enough to observe bleaching, it could also be possible that the crystal growth resulted in a crystal of low quality, leading to a strong electron-phonon coupling between dopant and crystal. From the fluorescence signal, it can be assumed that the crystal quality will not be sufficient for SMS. Both measurements represent the strongest achievable fluorescence signals achieved with this concentration and this method.

5.2.2 Deposition of crystals from solution via drop-touch method

So far, crystals from an oversaturated solution were deposited on a TOF by dropping solution onto the waist [38, 86, 106]. Beside the uncontrolled growth process of the crystals within the pipette, this method has the disadvantage of a high consumption of solution and a small probability that crystals adhere to the fiber. A different crystal deposition method, which relies on a rather simple setup and procedure, was therefore introduced. It is schematically shown in fig. 5.9.

After crystals have formed from the oversaturated solution according to the chosen parameters, a standard microliter plastic pipettor was drawn up with the solution. By slightly pressing the pipettor, a small drop was formed at the tip, small enough to not detach. The drop was then brought into contact with the TOF and immediately pulled away. This procedure was repeated until a crystal was adhered to the surface of the TOF. The TOF was coupled to the optical setup shown in fig. 4.1 and an adhered crystal could be identified with its fluorescence signal. Furthermore, the fluorescence and transmitted power are indication of the crystal quality and

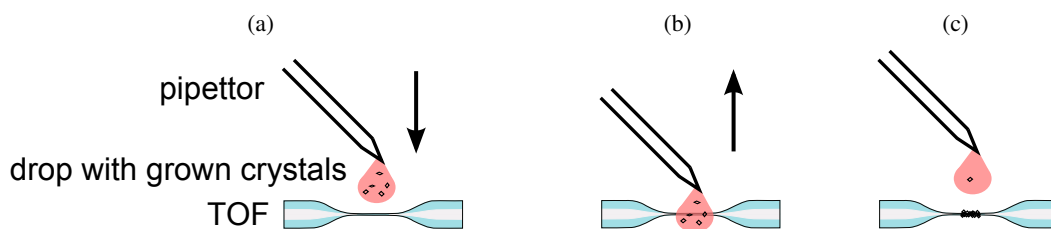


Figure 5.9: Drop-touch method of adhering crystals from solution to a TOF. Details see text.

crystal size, respectively. If the attached crystal was not satisfactory in terms of quality or size, it could be washed away by rinsing the TOF with acetone and the process could be repeated. For obtaining small crystals on the TOF via this drop-touch method, many tries might be necessary. The advantage of this method is that it can be repeated very often and quickly. After a crystal with appropriate quality and size was attached, the fluorescence signal was observed up to an hour to check if bleaching occurred, which would indicate a low crystal quality. Note that some bleaching can arise from terrylene molecules which are not incorporated in the crystal. In fig. 5.10 the time evolution of the background-corrected fluorescence of two samples directly after adhering to the TOF can be seen. In fig. 5.10(a) the fluorescence permanently decreases over time. After about 27 min, the signal is almost completely lost due to bleaching. The crystal in fig. 5.10(b) also exhibits a decrease in the fluorescence signal, but after a time of more than 36 min (green curve) the signal is stable and does not decrease further for the next 24 min (blue curve). For a first check of the crystal quality, features of the spectrum can be compared to the spectrum of a single terrylene molecule in p-terphenyl at room temperature (cf. fig. 3.11): the peak in the stable spectrum is clearly pronounced at 645 nm, even the small peak can be identified at 695 nm. In contrast, the unstable spectrum does not show a pronounced peak but a very wide peak with a shoulder at the position of 645 nm. The peak is so wide that the small peak at 695 nm is completely covered.

Before a crystal sample is processed further, in particular cooled down to cryogenic temperatures, the fluorescence signal should be stable. Furthermore, the shape allows a preselection of crystals with supposedly higher quality, according to the mentioned criteria.

5.2.3 Enhanced crystal growth via fast precipitation

For reproducibly producing small crystals with a good crystal quality providing a high terrylene stability and narrow lineshapes at room temperature, more control had to be gained over the whole growth process. Instead of changing the ratio of p-terphenyl and toluene and thereby varying the oversaturation of the used solutions, a precipitation agent can be used. For a possible precipitation agent, terrylene and p-terphenyl have to be insoluble and toluene has to be soluble. A solvent fulfilling these requirements is isopropanol. When isopropanol is added to an oversaturated solution of terrylene and p-terphenyl in toluene, the oversaturation increases instantly and strongly since the mixture of toluene and isopropanol have a lower solubility for the two molecule species. The accelerated crystal growth starts and creates a distribution of different

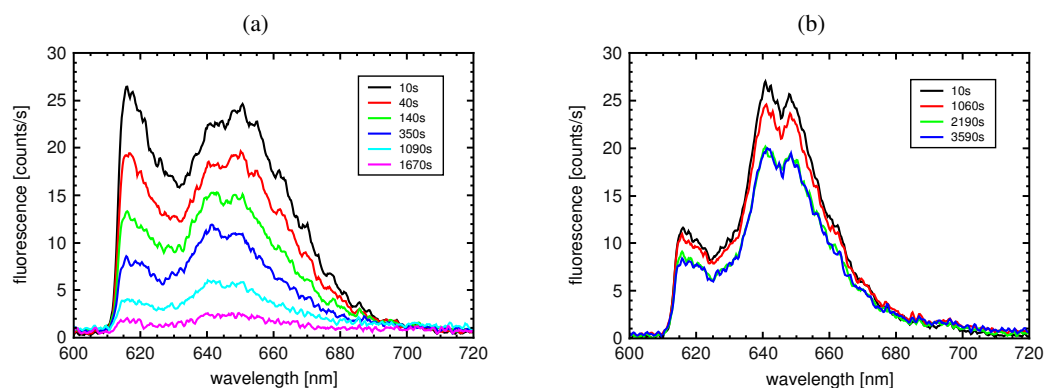


Figure 5.10: Time evolution of two background-corrected fluorescence spectra directly after adhering the sample to the TOF. A LP filter cuts the fluorescence below 610 nm. The sample in (a) was excited with 578.51 nm and a transmitted power of 27 nW prior to adhering the crystal. Bleaching is clearly visible and the fluorescence decreases almost to zero. The sample in (b) was excited with 578.5 nm and a transmitted power of 24 nW prior to adhering the crystal.

crystal sizes of monocrystalline structure in a suspension. After the precipitation is complete, further recrystallization and agglomeration which changes the structure and size of the crystals can occur over time. This can modify the crystals in two ways: While possible defects are cured improving the structure of the crystals, agglomeration leads to bigger crystals with an increased number of defects.

The procedure to produce such a suspension with crystals grown via fast precipitation was always as follows: Oversaturated solutions with the desired concentrations of terrylene and p-terphenyl in toluene were prepared. For further processing, a small defined volume of a few ml was filled into a separate recipient and heated again to 80 °C in an ultrasonic bath until all molecules were dissolved. After a specified time, room temperature isopropanol of a defined volume was added and the precipitation process was started. After a few minutes, the crystals are completely precipitated and the suspension can be used to place crystals on a TOF with the drop-touch method. The suspension can be used for several days over which the size and the quality of the crystals can however change. To gain access to the smaller crystals, the tendency of the suspension to form sediments can be used. A simple size selection was performed by joggling the solution and sedimenting it: The density of the crystals is higher than the one of the toluene/isopropanol mixture and the bigger crystals will sink much faster than the small ones. If the pipettor was drawn up in the upper part of the suspension, predominantly small crystals were captured.

Besides the known number of parameters for crystal growth, this procedure adds even more degrees of freedom. Some of them can be controlled, like the volume of the oversaturated solution, the volume of the precipitant, the elapsed time until the precipitant is added, and the time after the precipitation when the crystal sample is adhered to the TOF. Others, like the distribution of crystal sizes which are drawn up with the pipettor, are however difficult to control. To investigate the influence of the elapsed time before the precipitation is started on the crystal size

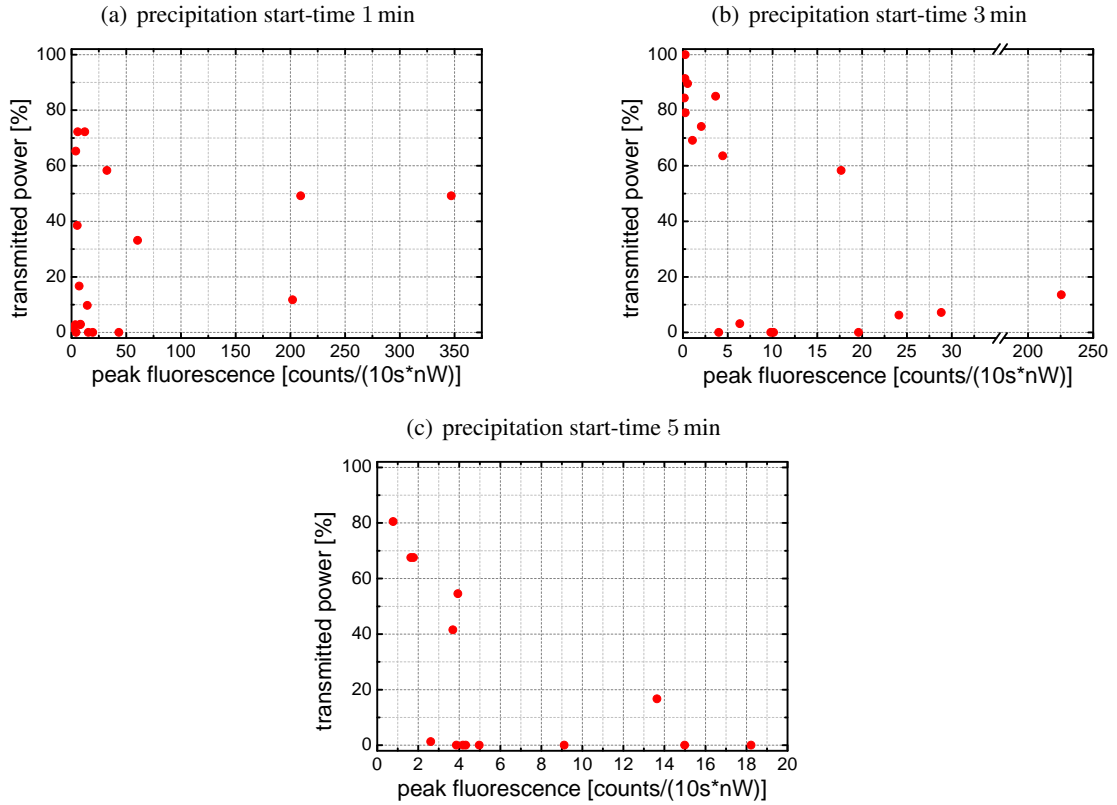


Figure 5.11: Dependence of background-corrected and excitation power-normalized maximum of fluorescence signal on transmitted power for terrylene doped p-terphenyl crystals for start-times of the precipitation between 1 min and 5 min. The initial concentration of the oversaturated solution was 8.55×10^{-5} g/g terrylene/p-terphenyl and 10.9 mg/ml p-terphenyl/toluene and the integration time of the spectrometer 10 s. Data taken from [113]. For details see text.

and the fluorescence yield, a series of crystal depositions on a TOF was performed, where the transmitted power and the peak fluorescence were measured. Here, peak fluorescence means that only the maximum fluorescence count rate of the whole spectrum was taken into account. Only fluorescence signals with a pronounced peak structure like in fig. 3.11 were used. The excitation wavelength was 578.5 nm, the integration time of the spectrometer 10 s and the maximum peak fluorescence was background-corrected and normalized for the excitation power. In fig. 5.11 the relation between transmitted power and peak fluorescence can be seen for elapsed times of 1 min, 3 min and 5 min before the precipitation was started. The transmitted power is related to the crystal size and the number of deposited crystals. The bigger the crystal or the more are adhered, the smaller is the transmitted power. The peak fluorescence is an evidence for the terrylene concentration of the crystal while it would be desirable to have a larger data base, some fundamental conclusions can be drawn: The shorter the start-time, the higher is the possible achievable peak count rate and the higher is the number of crystals with a substantial

transmitted power. It can be concluded that shorter precipitation start-times lead to higher concentrated and smaller crystals. When comparing the achieved transmitted powers of all three measurements it is conspicuous that for half of the adhered crystals the transmitted power drops to or close to zero. No measurement shows a crystal with 100 % of transmission and an appreciable fluorescence signal, indicating the difficulty to grow, pick, and deposit a crystal of small size on a TOF. Crystals with high transmitted power could be more often produced with short precipitation start-times (5.11(a),5.11(b)). The variation of results is quite high and no conclusive result can be drawn from this measurement, but precipitation start-times between 1 min and 3 min seem to result in slightly smaller crystals with a distinctive fluorescence. For the preparation of terrylene doped p-terphenyl crystals which were used for SMS in this work, the time was always chosen between those values.

To examine the crystal quality and smallest achievable size, a drop of a precipitated solution (which was used for crystal sample #3 later) was drawn up with the pipettor like for the adhering of crystals on the TOF and was placed on a copper substrate. After drying out, the sample was investigated with a SEM. The resulting images can be seen in fig. 5.12(b) and fig. 5.12(c). In both images, the solution evaporated from the left to the right side, i. e. from the outer to the inner side of the drop. As known from chromatography, during the movement of the mobile phase (suspension consisting of crystals and solution), the different sizes of the consisting particles lead to different speeds compared to the mobile phase. The big crystals are too slow to follow the withdrawing evaporating solution and are therefore separated from the mobile phase. This separation by crystal size can be seen in fig. 5.12(b), which is giving an overview of a $150\text{ }\mu\text{m} \times 100\text{ }\mu\text{m}$ large area of the remainders on the substrate. The crystal size is decreasing from left to right. In fig. 5.12(c), an image of the center of the remaining crystals is shown. The crystal size is now very homogeneous. To estimate the size of the smallest crystals achievable via the precipitation growth method, in fig. 5.12(d) the magnification of an area in the center of the remaining crystals can be seen. Exemplarily, one small crystal was measured to have a length of 381.5 nm. This is almost as small as the diameter of 320 nm of the used TOFs. The shape is similar to the p-terphenyl monocrystals produced via spin-coating and measured with an AFM by S. Karotke [61]. Another possibility to determine the crystal structure is to measure the selected area electron diffraction (SAED) with a transmission electron microscope (TEM). In fig. 5.12(a) the SAED signal of a terrylene doped p-terphenyl crystal, produced from the sample later used for crystal #3 taken and measured by B. Bayer from the Universität Wien, can be seen. The diffraction pattern fits well to the crystal line structure of a p-terphenyl monocrystal. Thus, the crystal growth method via fast precipitation has proven to produce monocrystals of small size.

To investigate the possibility of depositing such small crystals on a TOF via the drop-touch method, different oversaturated solutions were precipitated and crystals from the suspension were placed in the described way on the TOF while monitoring the transmitted power. The prepared samples were again examined with a SEM. Since the main focus was to adhere small crystals and these crystals are often not clearly identifiable with a SEM on a TOF, so far only one crystal but without monocrystalline structure could be clearly found on the TOF. The resulting image can be seen in fig. 5.13.

The precipitation method has shown to produce significantly smaller crystals than the former

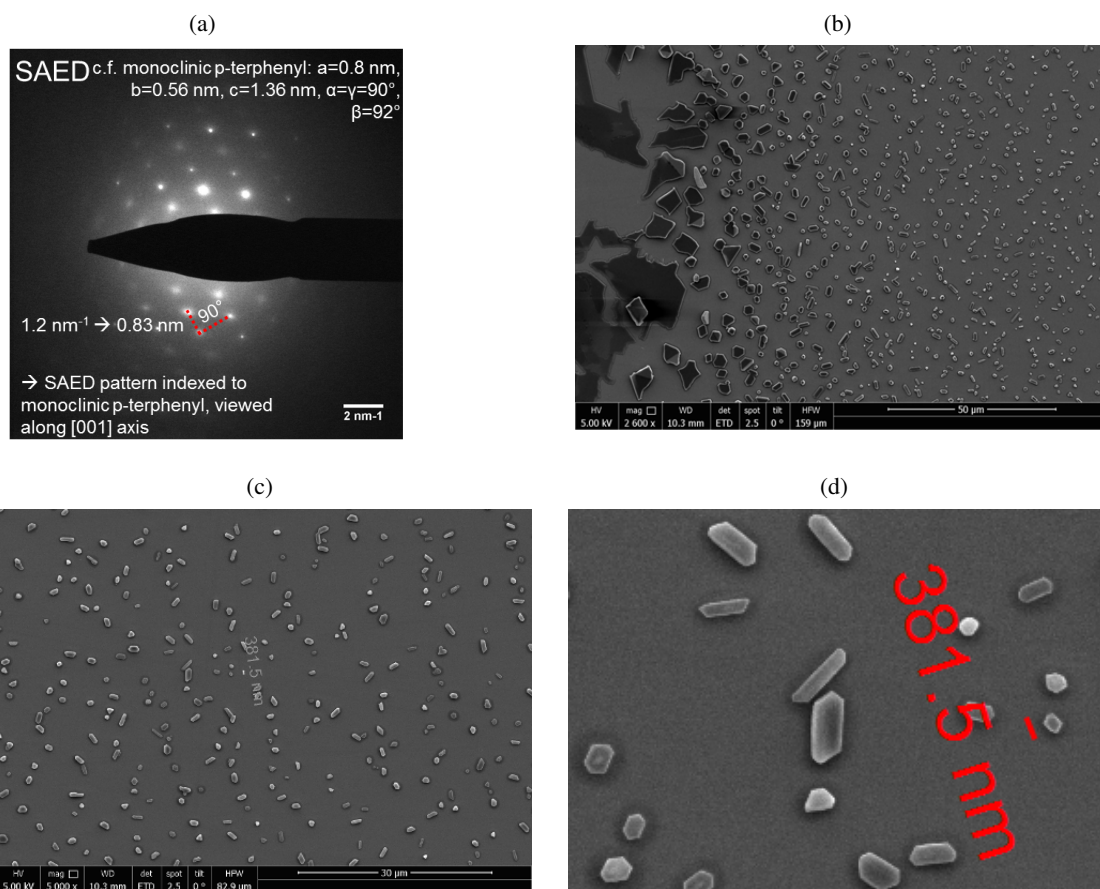


Figure 5.12: TEM and SEM images to show the monocrystalline structure of the terrylene doped p-terphenyl crystals obtained from a precipitation reaction of an oversaturated solution of terrylene and p-terphenyl in toluene with isopropanol as a precipitating agent (same sample used for crystal #3 later). **(a)** shows a SAED image of a TEM (taken by B. Bayer from the Universität Wien). The diffraction pattern proves the monocrystalline structure. **(b)** and **(c)** show SEM images of the dried suspension. **(d)** is a magnification of **(c)** including a length measurement of a small monocystal. For details see text.

growth method. The size is small enough to still transmit light through the TOF and the shape is monocrystalline. The drop-touch method has proven to improve the deposition of crystals on the TOF and especially to allow the adhering of small crystals. Three of the many produced crystal samples have been used for SMS. The corresponding ensemble fluorescence spectra under ambient conditions can be seen in fig. 5.14. In tab. 5.1 the underlying production characteristics for the three crystal samples can be seen. The highest achievable power transmission through the fiber with a single molecule sample on the TOF was 46.3 %.

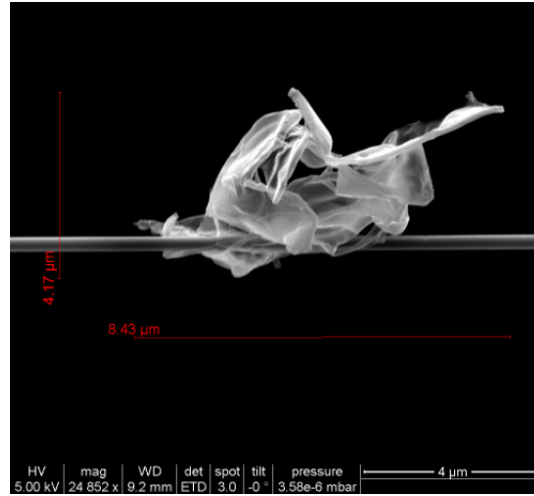


Figure 5.13: SEM image of a terrylene doped p-terphenyl crystals on a TOF, produced from a volume of 0.91 ml of oversaturated solution with an initial terrylene/p-terphenyl concentration of the mixture of 8.3×10^{-5} g/g and an oversaturation of 14.62 mg/ml p-terphenyl/toluene. 3.09 ml isopropanol were used as a precipitation agent and caused a drop in the transmitted power to 9.8 %.

	crystal #1	crystal #2	crystal #3
volume solution	0.7 ml	0.35 ml	0.35 ml
start-time	1 min 40 s	2 min	2 min
volume precipitant	3.3 ml	3.65 ml	3.65 ml
resttime	1 day	none	4 days
initial concentration (g/g)	8.3×10^{-5}	8.5×10^{-5}	7.8×10^{-5}
oversaturation (mg/ml)	14.62	14.90	14.48
transmitted power (%)	25.0	46.3	42.5

Table 5.1: Crystal samples used for SMS with their production characteristics and transmitted power through the fiber after adhering to the TOF. The production characteristics covers the volume of oversaturated solution and precipitant. The “start-time” is the elapsed time before the precipitation process is initiated. The time between the precipitation of the solution and the deposition of crystals is the “resttime”. Concentration and oversaturation are from the initial solution. For further details see text.

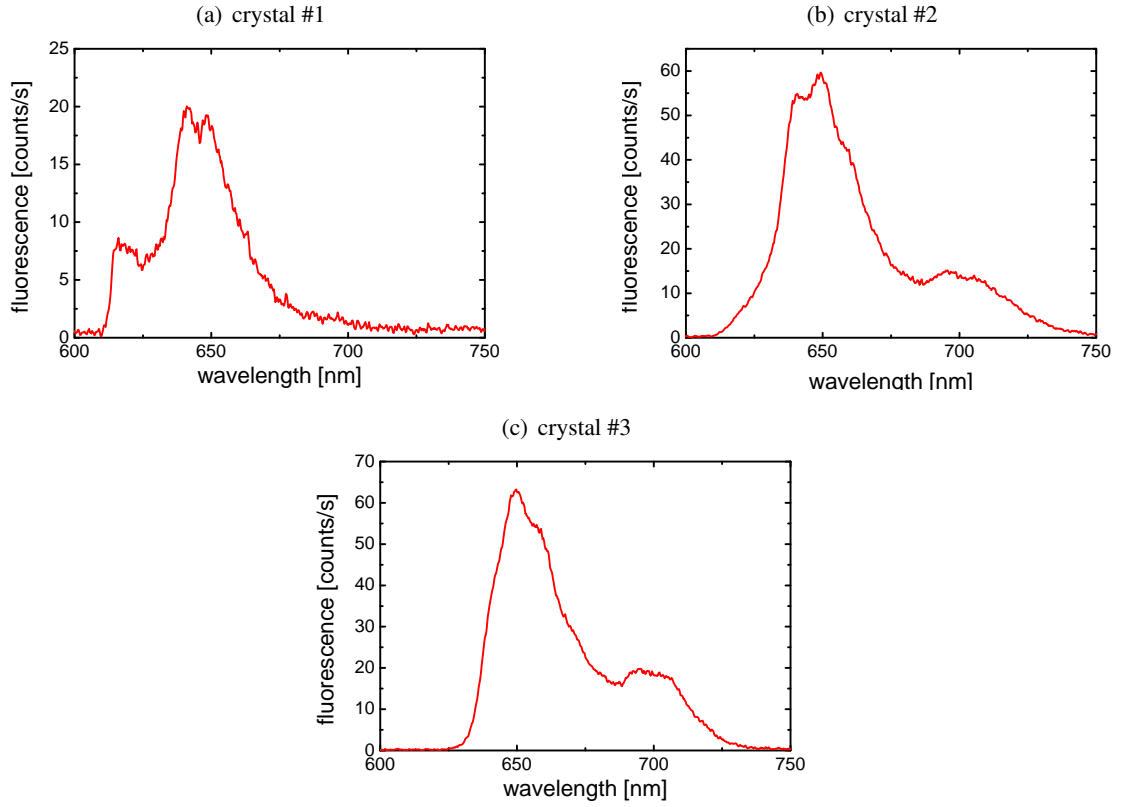


Figure 5.14: Background corrected ensemble fluorescence spectra at ambient conditions for the crystals #1 to #3, which were used for SMS. LP filters cut the fluorescence below 610 nm **(a)** and 630 nm **(b)** and **(c)**, respectively. Excitation wavelengths are always 578.5 nm and excitation powers are **(a)** 24 nW of transmitted power prior to adhering the crystal, **(b)** 82 nW of transmitted power prior to adhering the crystal and **(c)** 61.2 nW excitation power inside the fiber, measured with the 2x2 single mode fiber optic coupler.

Spectroscopy of molecules in solid state at low temperatures

Optical nanofibers have proven to be an extremely sensitive tool for surface spectroscopy [24, 114]. But, so far, only ensembles of dye molecules, either surface adsorbed or as dopants in an organic crystal matrix, have been investigated using nanofibers. As described in chapter 5, preparing crystal samples of terrylene in p-terphenyl from an oversaturated solution via fast precipitation leads to the smallest crystal sizes usable for spectroscopy on a TOF and, at room temperature, to fluorescence signals similar to spectra of single terrylene molecules. In order to perform spectroscopy of single terrylene molecules with a TOF, the crystal samples have to be cooled down to cryogenic temperatures to take advantage of the accompanying narrowing of the homogeneous linewidths.

In this chapter, the process of cooling down the TOF is described and fluorescence measurements on the molecular ensemble of different crystal samples are presented. It is shown how single emitters within the sample can be found and identified. Once single molecules are identified, several experiments are performed in order to characterize their properties. The crystal samples #1 to #3 with the characteristics presented in tab. 5.1 are used for the different measurements presented here.

As common in spectroscopy and for better comparison with existing work, for the following measurements the scale is converted from wavelength $[\lambda] = \text{nm}$ to wavenumber $[\tilde{\nu}] = \text{cm}^{-1}$. However, if the spectral range is on the order of a single molecule, the frequency $[\nu] = \text{Hz}$ is used as a scale.

Cooling down procedure

Once the crystal samples were prepared, deposited on the TOF, and have proven to be of the desired quality (in terms of fluorescence signal, size and stability), the fiber mount was inserted into the open sample chamber. After carefully closing and sealing the sample chamber and the

side flanges with indium wire, the whole cryo rod was evacuated with a scroll pump (oerlikon, Scrollvac SC15D) for at least 1 h before it was placed in the warm cryostat and fixated. The nitrogen tank was then filled with liquid nitrogen to start the slow pre-cooling of cryo rod and the sample. Because the sample volume was evacuated and the liquid nitrogen had no direct contact with the sample chamber, the pre-cooling from 295 K to round about 125 K, took 2 h. For the further cooling, liquid helium was filled into the main cryo reservoir which contained the sample chamber with the sample. The reservoir was simply completely filled, which reduced the temperature further to round about 20 K on a timescale of 20 min. At this point, a small amount of helium gas (Air Liquide, Alphagaz 2) was injected into the sample space of the cryostat. This was done very slowly in order to avoid turbulences. It has been pointed out, that too much buffergas degrades the light guiding abilities of the TOF [106], therefore it is important to only use a tiny quantity. The amount of the buffergas was not exactly quantified but when the spectroscopic signal of the sample showed a significant change in width, the gas flow was stopped. This was the case for round about 10 mbar of helium buffergas at a temperature of 4.4 K. The fact that the width of the signal decreased immediately and there was no further change with time guarantees that the sample was efficiently cooled.

Figure 6.1 shows a series of fluorescence spectra of crystal #2 during the cooling process from room temperature down to cryogenic temperatures. The excitation wavelength was 578.5 nm and, thus, always resonant with a terrylene ensemble. All spectra show the region between $13\,500\text{ cm}^{-1}$ and $16\,500\text{ cm}^{-1}$, a long pass filter filtered out the fluorescence light with wavenumbers higher than $16\,393\text{ cm}^{-1}$. The spectral resolution of the spectrometer for these spectra is round about 0.4 nm (10 cm^{-1}). The broad band with the slight double peak structure located at $15\,500\text{ cm}^{-1}$ at room temperature reveals its substructure due to the homogeneous narrowing of the spectral shape when lowering the temperature. At 4.4 K (cf. fig. 6.1(d)), three main lines with a substructure are visible. These narrow spectral lines will be examined further in the next section. The buffergas was led into the sample chamber directly after taking spectra 6.1(c). Since the spectrum consists of one broad band with no pronounced substructure or even separated peaks before adding the buffergas, it can be assumed that the sample was not perfectly thermalized without. Note that the absolute emitted fluorescence in this spectral region (area under the curve) experienced a strong drop between 295 K and 150 K (cf. fig. 6.1(a) and 6.1(b)), followed by a further decrease when cooled to 20.1 K (cf. fig. 6.1(c)). For 4.4 K the overall emitted fluorescence increased to a value higher than at room temperature (cf. fig. 6.1(d)). The excitation power and excitation wavelength was kept constant during the whole cooling procedure. The cooling process is accompanied by a reduction of phonons and a narrowing of the ZPL. This can lead to a reduced number of excited molecules. At 4.4 K the ZPLs are very narrow and almost lifetime-limited with a low saturation intensity. Furthermore, only a small spectral jump, as observed for terrylene in p-terphenyl (cf. the corresponding subsection in sec. 6.2.1) could bring the narrow ZPL of a molecule in full resonance with the excitation laser, leading to a strong fluorescence emission.

Once a molecule sample was cooled down to cryogenic temperatures, it was kept at this temperature for several months without interruption. All the following measurements were performed at a sample temperature of 4.4 K.

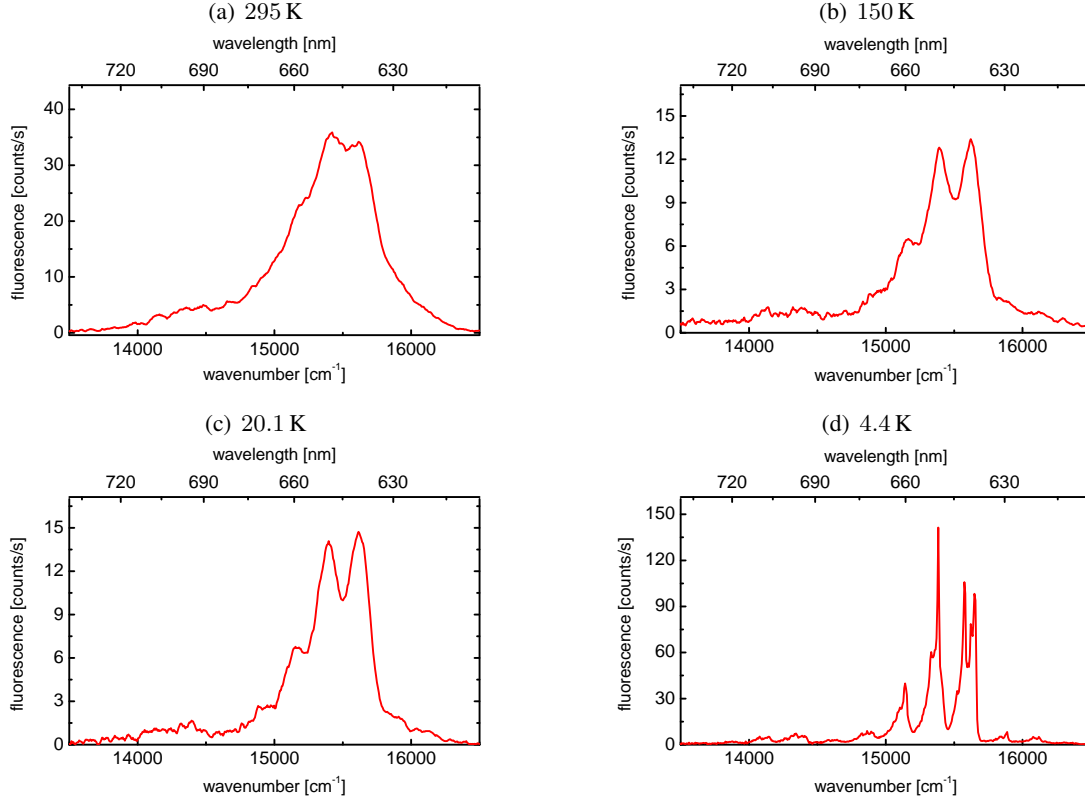


Figure 6.1: Background corrected fluorescence signal of crystal #2 at different temperatures during the cooling process. The excitation power is 82 nW of transmitted power prior to adhering the crystal with a wavelength of 578.5 nm and the spectral resolution is 0.4 nm (approx. 10 cm⁻¹) for all spectra. The approx. overall emitted fluorescence is **(a)** 4800 counts/s, **(b)** 1800 counts/s, **(c)** 1400 counts/s, and **(d)** 6000 counts/s. For details see text.

6.1 Ensemble spectroscopy

6.1.1 Identification of peaks

To resolve the narrow vibronic lines further and to get insights into the fluorescence spectra at cryogenic temperatures, a different grating of the spectrometer was used, resulting in an effective resolution of 0.1 nm (approx. 2.5 cm⁻¹). For a better comparability with spectral positions given in literature, this and the following spectra are converted to relative wavenumbers. Therefore, the excitation wavenumber $\tilde{\nu}_0$ is subtracted from each wavenumber $\tilde{\nu}$ of the spectrum. This results in positive wavenumbers, although the excitation is always carried out at a higher energy than the fluorescence is observed. The fluorescence spectrum of crystal sample #1 at a temperature of 4.4 K, excited with 577.895 nm and an excitation power of 16.2 nW of transmitted power prior to adhering the crystal can be seen in fig. 6.2. This high resolution fluorescence spectrum reveals characteristic peaks at certain positions, belonging to pure vibronic transitions (with no

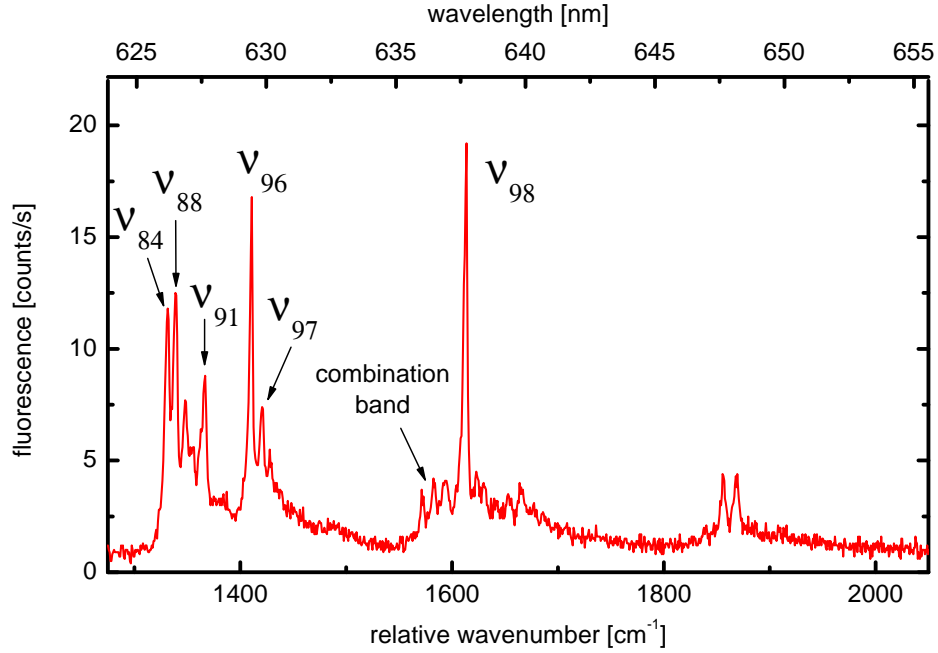


Figure 6.2: Background corrected fluorescence ensemble spectrum of crystal #1 in the center of site X_4 at a temperature of 4.4 K for an excitation wavelength of 577.895 nm and an excitation power of 16.2 nW of transmitted power prior to adhering the crystal. Peaks with known vibronic origin are denoted according to [42].

phonon participation). Known peaks are denoted according to [42]. All these vibronic transition originate from different carbon-carbon stretch vibrations within the terrylene molecule and can be found in detail in literature [42, 115]. On the low energy side, these transitions are accompanied by phonon sidebands, clearly visible for the two bands at 1450 cm^{-1} and 1700 cm^{-1} . As phonon sidebands have a broad spectral distribution, they cannot be further resolved. The stronger the phonon sideband, the more phonon states are excited within the terrylene molecules. The intensity of the phonon sideband strongly increases when the ZPL is saturated or the crystal sample exhibits a strong electron-phonon coupling. The electron-phonon coupling is determined by the coupling of the electronic states of a terrylene molecule to the vibrations of the p-terphenyl crystal lattice. Therefore, the crystal quality in terms of crystal structure is important to achieve a small phonon sideband. According to [115], the combination band is the simultaneous excitation of the vibronic lines ν_{84} and ν_{88} with a strong vibronic line at 243 cm^{-1} .

For a further investigation of the strength and the position of the vibronic transitions near the transition frequency of the optical site X_4 , the fluorescence ensemble spectra of different crystal samples are compared. The site X_1 was not investigated for crystal #1 and crystal #3 or did not exhibit a terrylene population (crystal #2). Site X_2 and X_3 were investigated but for this spectral range, the fluorescence is partly cut off by a 630 nm long pass filter. In fig. 6.3 a comparison

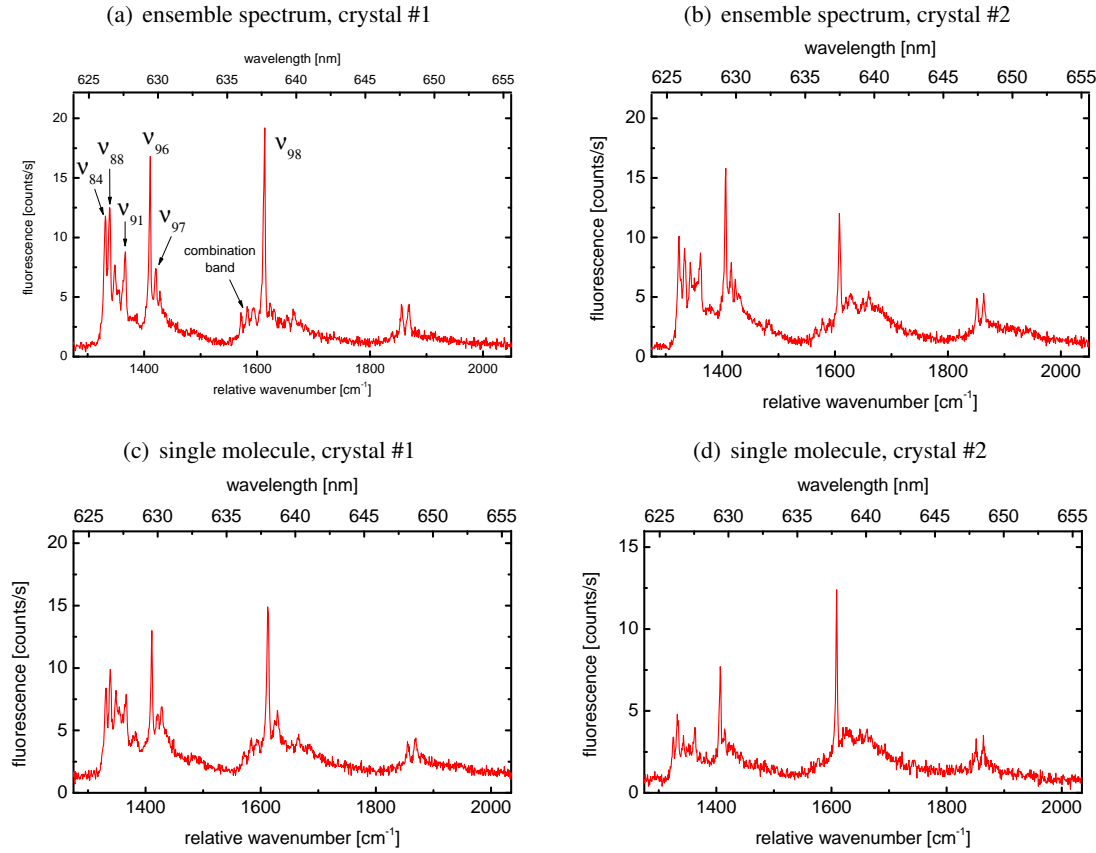


Figure 6.3: Comparison of background-corrected ensemble fluorescence spectra with the fluorescence spectra of single molecules near the center of optical site X_4 for different crystal samples: **(a)** ensemble spectrum of crystal #1 with a excitation wavelength of 577.895 nm and an excitation power of 8.1 nW of transmitted power prior to adhering the crystal. **(b)** ensemble spectrum of crystal #2 with an excitation wavelength of 577.894 nm and an excitation power of 52.4 nW of transmitted power prior to adhering the crystal. **(c)** single molecule at the spectral position 577.896 nm in crystal #1 and an excitation power of 1.9 nW of transmitted power prior to adhering the crystal and **(d)** single molecule at the spectral position 577.851 nm in crystal #2 and an excitation power of 17 nW of transmitted power prior to adhering the crystal. For details see text.

between the fluorescence spectra of the different ensemble spectra of crystals #1 and #2 and fluorescence spectra of single molecules can be seen for the X_4 site. When comparing the peak positions of ensemble and single molecule spectra, no significant difference can be detected. Due to the higher excitation power, phonon sidebands are more distinctive for the measurements in crystal #2 (cf. fig. 6.3(b) and fig. 6.3(d)). The intensity of the different vibronic transitions shows differences, most easily visible for the two strongest vibronic lines ν_{98} and ν_{96} : in most cases, the intensity of ν_{98} is higher than for ν_{96} for the ensemble as well as the single molecule

spectrum. Only for the ensemble spectrum of crystal #2 near the site X_4 (cf. fig. 6.3(b)) it is the other way around.

The spectral center positions of the six known peaks of the purely vibronic transitions of the two ensemble spectra are determined via Gaussian fits and are listed in tab. 6.1.

Taking into account the spectral resolution of 2.5 cm^{-1} of the spectrometer for these spectra, all ensemble peak positions of both samples agree well with each other. Only the lowest transition ν_{84} is slightly shifted to a lower frequency. Compared to the peak positions of a single molecule in site X_4 measured by Kummer et al. [42] (second column), all positions are shifted between 32 cm^{-1} and 44 cm^{-1} to higher frequencies (with an average of 41.5 cm^{-1} for crystal #1 and 36.3 cm^{-1} for crystal #2). However, the distance between the peaks agrees very well.

The reason for this shift possibly lies in a different influence of the crystal host on the vibrational transitions of the terrylene molecules. Earlier measurements of fluorescence ensemble spectra of terrylene in p-terphenyl on a TOF in this group revealed a shift to higher frequencies as well, but only 11 cm^{-1} to 14 cm^{-1} [38, 86]. The main difference between the crystal samples used before and now is the way of manufacturing: while the former crystals were produced from an oversaturated solution, crystallizing mainly uncontrolled within the pipette (cf. sec. 5.2), the crystal samples here are all produced via the method of fast precipitation and deposited via the drop-touch method. The spectrometer has never been precisely calibrated, e. g. with a helium-neon laser. Only the internal calibration method of the spectrometer was used before each measurement. Thus, a systematic error cannot be ruled out.

6.1.2 Anomalous peaks

The peak structure of the shown ensemble spectra coincide well with each other except for the intensity of some vibronic transitions and the spectral position of the transition ν_{84} . Nevertheless, in one ensemble spectrum of crystal #2, near the transition frequency of the X_4 site and in the spectrum of the single molecule at a spectral position of 577.896 nm in crystal #1 (cf. fig. 6.3(c)), a clear deviation of the common structure was observed. For the ensemble spectrum, this deviation is shown in fig. 6.4: the vibronic transitions are marked following the previous notation and the additional peak is assigned with ν_x . Note that for better visibility of the peaks, a smaller area is shown here, compared to the previous spectra. All peak positions are determined via Gaussian fits and are listed in tab. 6.1. As before, they are offset by 33 cm^{-1} to 50 cm^{-1} . Since all peaks have their origin in vibronic transitions of terrylene in p-terphenyl, additional peaks are an indication, that molecules with different transitions exist and can be excited. From earlier experiments with terrylene in polyethylene it is known, that about 10 % to 20 % of the molecules show a qualitatively different intensity and frequency pattern [115]. Also earlier experiments of terrylene in p-terphenyl revealed the existence of a terrylene species with additional vibronic transitions but at slightly different spectral positions [42]: Kummer et al. discovered two additional vibronic lines in site X_2 at positions 1370 cm^{-1} and 1583 cm^{-1} . Due to a low signal-to-noise ratio, the line at 1370 cm^{-1} cannot be applied to any peak here. The line at 1583 cm^{-1} showed a much weaker intensity than their transition ν_{98} at 1574 cm^{-1} (X_2) and was 9 cm^{-1} shifted to a higher relative wavenumber. Taking into account the spectral resolution of 2.5 cm^{-1} for the measurement presented here, the distance of 11 cm^{-1} between ν_x and ν_{98} corresponds

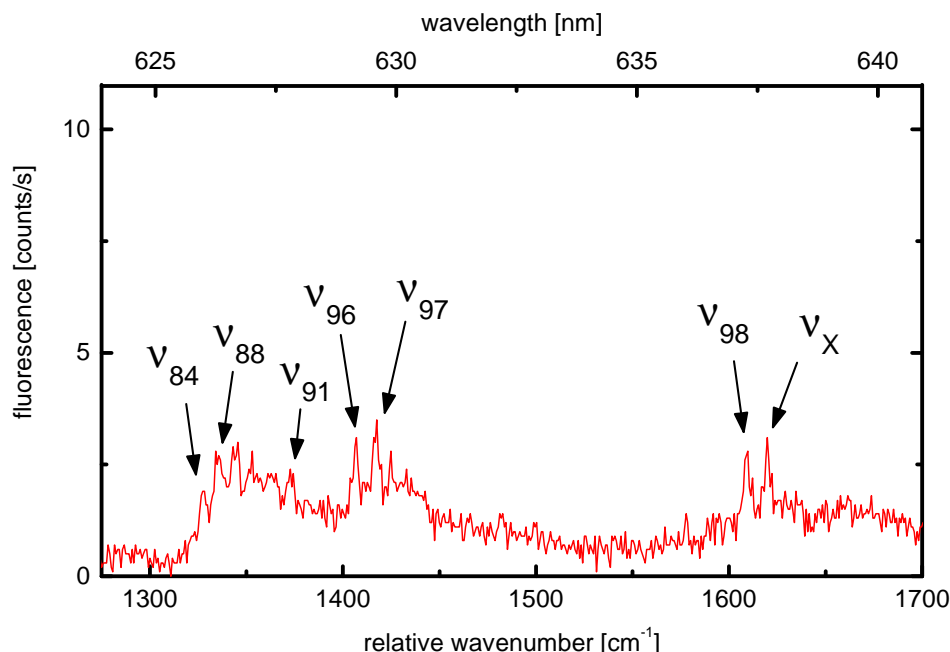


Figure 6.4: Background corrected fluorescence ensemble spectrum of the optical site X_4 of crystal sample #2, showing an additional vibronic transition (ν_x). Excitation wavelength was 577.935 nm with an excitation power of 9.0 nW of transmitted power prior to adhering the crystal. The vibronic transitions are denoted according to the spectra before.

well with this distance and it can be concluded that the anomalous peak here is the same as discovered by Kummer et al.

Several attempts have been made to explain the origin of these shifted or additional vibronic lines [42, 115]. An isotopic substitution with a heavy ^{13}C atom in the terrylene structure would increase the reduced mass and should shift the vibronic transitions towards lower frequencies. Also, for pentacene in p-terphenyl it has been found, that heavy atom substitution shifts the purely electronic transition to shorter wavelengths [116]. Since the spectrum showing the anomalous peak is recorded in the red wing of site X_4 , the substitution with ^{13}C as the reason for the additional vibronic line at this excitation wavelength can be ruled out. More likely is the existence of different types of environments within the p-terphenyl matrix, leading to different vibronic transitions. For the crystals manufactured via fast precipitation and investigated via a TOF and compared to earlier experiments and other production methods, the amount of molecules with anomalous peaks seems to be very low: in all crystal samples investigated, it could only clearly be observed twice.

	SM, X ₄ [42]	crystal #1, X ₄	crystal #2, X ₄	crystal #2, X ₄ , anomalous
ν_{84}	1288 cm ⁻¹	1331 cm ⁻¹	1323 cm ⁻¹	1328 cm ⁻¹
ν_{88}	1295 cm ⁻¹	1339 cm ⁻¹	1334 cm ⁻¹	1336 cm ⁻¹
ν_{91}	1323 cm ⁻¹	1366 cm ⁻¹	1361 cm ⁻¹	1373 cm ⁻¹
ν_{96}	1369 cm ⁻¹	1410 cm ⁻¹	1406 cm ⁻¹	1407 cm ⁻¹
ν_{97}	1379 cm ⁻¹	1420 cm ⁻¹	1416 cm ⁻¹	1417 cm ⁻¹
ν_{98}	1576 cm ⁻¹	1613 cm ⁻¹	1608 cm ⁻¹	1609 cm ⁻¹
ν_x				1620 cm ⁻¹

Table 6.1: Peak positions of different vibronic transitions in the ensemble fluorescence spectra of the optical site X₄ in crystal samples #1 and #2 (cf. fig. 6.3). The last row contains the positions of the spectrum containing an anomalous peak denoted with ν_x (cf. fig. 6.4). The literature values are determined experimentally for a single molecule in X₄ by Kummer et al. [42].

6.1.3 Fluorescence excitation spectroscopy

The first single molecule detection experiment by Moerner and Kador in 1989 allowed to measure the absorption signal of a single pentacene molecule in a p-terphenyl host directly [5]. However, due to the ratio of the unfavorable molecular cross section to the beam cross section, the absorption was low and only led to a limited signal-to-noise ratio. In order to overcome these limitations, Orrit et al. introduced fluorescence excitation spectroscopy as a new method for single molecule spectroscopy in 1990 [6], making it the preferred technique for single molecule investigation. For a fluorescence excitation measurement, a tunable narrowband single-frequency laser is scanned over the absorption band of the single molecule or ensemble and the emitted fluorescence is collected. By recording the fluorescence intensity as a function of the excitation wavelength, the molecular absorption can be visualized. To maximize the signal-to-noise ratio, the emitted fluorescence has to be collected efficiently and scattered light has to be minimized. Therefore, an extinction of the excitation light by a long pass filter is essential.

Here, the fluorescence was either detected by one of the SPCMs or the spectrometer (cf. fig. 4.1). The emitted fluorescence of a molecule covers a broad range of wavelengths, since the emission occurs from the ground vibrational level $\nu' = 0$ of the first electronically excited state S₁ to the different vibrationally excited levels of the electronic ground state S₀ (cf. fig. 3.1 for the energy levels within a molecule and fig. 6.2 for the spectral representation of some of these vibronic transitions). While the SPCM counts all incoming photons passing the long and short pass filters indiscriminately, the spectrometer distinguishes spectrally between them and a manual integration over a specific spectral region has to be performed afterwards. The spectrometer is sensitive to cosmic radiation hitting the CCD, which causes additional events adding to the fluorescence counts. If such an event was recorded in the spectral range used for the fluorescence excitation measurement, the recorded spectrum was discarded. In order to minimize the spectral noise and to raise the amount of usable recordings, the range of integration was narrowed down to the ν_{98} vibronic transition. It offers one of the strongest peaks and allows the use of a 630 nm long pass and a 650 nm short pass filter to block the laser excitation light and other scattered light.

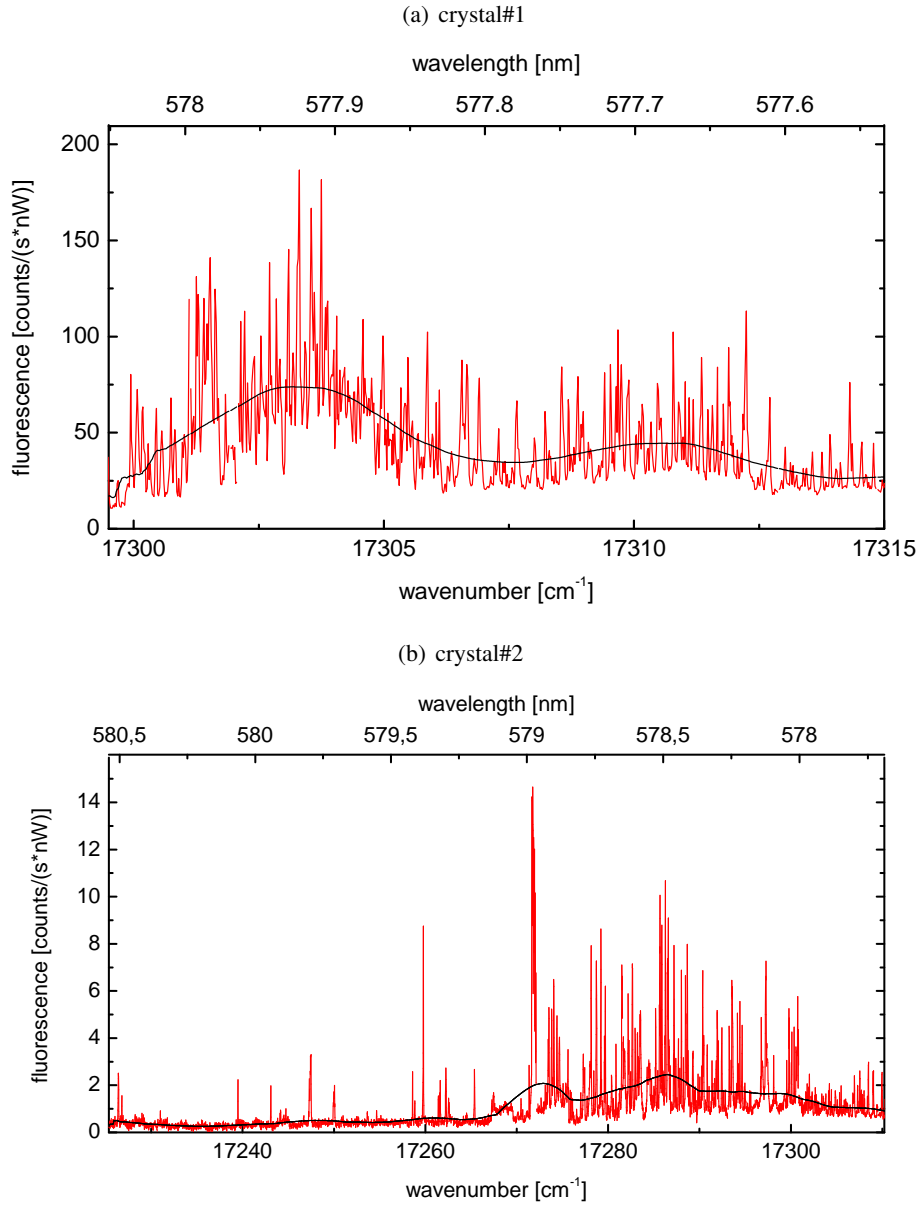


Figure 6.5: Fluorescence excitation spectra of **(a)** crystal #1 with an excitation power between 1.7 nW and 2.3 nW of transmitted power prior to adhering the crystal and **(b)** crystal #2 with an excitation power between 10.5 nW and 52 nW of transmitted power prior to adhering the crystal. The smoothed curves (black lines) are the moving averages of the fluorescence signals. For both measurements, the laser frequency scan speed is 50 MHz/s. The fluorescence is normalized for an excitation power of 1 nW. For details see text.

Detailed fluorescence excitation measurements were performed for crystal samples #1 and #2. They can be seen in fig. 6.5. Both spectra were obtained by scanning the laser frequency continuously with a speed of 50 MHz/s and measuring the total fluorescence counts in a wavelength range of 0.63 nm around the vibronic transition ν_{98} . The integration time is 10 s per data point and both spectra are normalized to an excitation power of 1 nW. Note, that only the spectrum of crystal #2 in fig. 6.5(b) covers the full spectral range of the four crystal sites X_1 to X_4 of terrylene in p-terphenyl. The spectrum of crystal #1 in fig. 6.5(a) covers only the spectral range of X_4 . Both spectra exhibit a strong inhomogeneous broadening of the ZPLs of the molecules, resulting in a wide range of transition frequencies. For a sample with an equal distribution of terrylene molecules on the four crystal sites in p-terphenyl, the fluorescence excitation is expected to show four strong peaks at the spectral position of the sites at $17\,230\text{ cm}^{-1}$ (X_1), $17\,286\text{ cm}^{-1}$ (X_2), $17\,293\text{ cm}^{-1}$ (X_3) and $17\,304\text{ cm}^{-1}$ (X_4) (cf. fig. 3.12). For a possible assignment of peaks to the spectral position of the sites, the moving averages of the fluorescence signal are added (black lines). For crystal #1 two peaks can be identified at $17\,303.3\text{ cm}^{-1}$ and at $17\,310.5\text{ cm}^{-1}$. The first one can be identified as X_4 while the second one is of unknown origin. In crystal #2 no peaks are clearly identifiable, either because they are missing (X_1) or they are strongly smeared out (X_3 and X_4). The smoothed fluorescence of crystal #2 shows two peaks at $17\,272\text{ cm}^{-1}$ and at $17\,286\text{ cm}^{-1}$ of which the latter one can be probably assigned to X_2 . Although both crystal samples were produced from oversaturated solutions with a similar terrylene concentration (cf. tab. 5.1), the spectra reveal that the terrylene concentrations of the crystals are quite different: the fluorescence count rate is strongly increased for crystal #1. The strength of inhomogeneous broadening cannot be compared for both crystals, since the fluorescence excitation spectrum of crystal #1 covers only a small range of crystal #2.

6.1.4 Statistical finestructure

As described in sec. 3.2.1, the absence of smoothness of the inhomogeneous broadened line is a direct result of the superposition of the narrow homogeneous lines of many individual molecules. Since the transition energies of these molecules are stable over time, the spectral position of the peaks is not varying when measured at different times. The spectral peaks represent the statistical fine structure (SFS) It can be identified by repeatedly performing a measurement of the fluorescence excitation in the same spectral region. The measurement of the SFS was performed in the region of the X_4 site for crystal #1 and can be seen in fig. 6.6. It shows the fluorescence excitation determined with a resolution of 500 MHz. The integration is carried out over a spectral range of 0.63 nm around the vibronic transition ν_{98} . The red line is a magnification of the spectrum presented in fig. 6.5(a). The black line corresponds to a fluorescence excitation measurement performed four days later. Both measurements agree well with each other, showing narrow peaks with the same intensity at the same spectral positions. Small differences in peak position or intensity are probably due to instabilities of the laser scan speed.

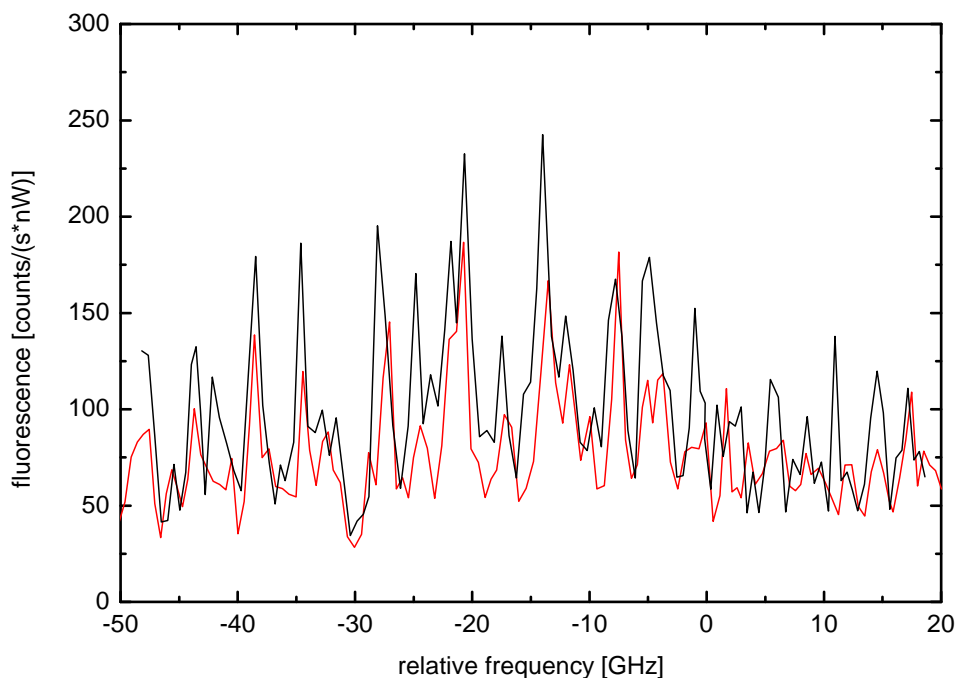


Figure 6.6: Detailed fluorescence excitation spectrum around the purely electronic transition of site X_4 (zero detuning) in crystal #1 with a laser scan speed of 50 MHz, an integration time of 10 s and normalized to an excitation power of 1 nW of transmitted power prior to adhering the crystal. Both spectra are recorded with a time difference of 4 d. For details see text.

6.2 Single molecule experiments

6.2.1 Finding a single molecule in a haystack

The fluorescence excitation measurements give a first insight into the spectral position of the ZPLs of individual terrylene molecules within the p-terphenyl crystal. To verify that any of the sharp peaks correlates to the ZPL of a single molecule, the fluorescence autocorrelation is measured.

Fluorescence excitation and linewidth

To reduce the number of possibilities for such a measurement dramatically, a preselection was performed by identifying the narrowest peaks in the fluorescence excitation spectrum for each crystal sample. The laser scan speed was reduced stepwise to a minimum of 1 MHz/s, which could be still handled by the stabilization of the dye laser, and promising spectral regions for a fluorescence excitation were scanned. This results in fluorescence excitation spectra of much higher resolution. In fig. 6.7(a) such a detailed spectrum can be seen. It is a re-scan of a small area of the fluorescence excitation spectrum of site X_4 in crystal #1 showed in fig. 6.5(a) with a

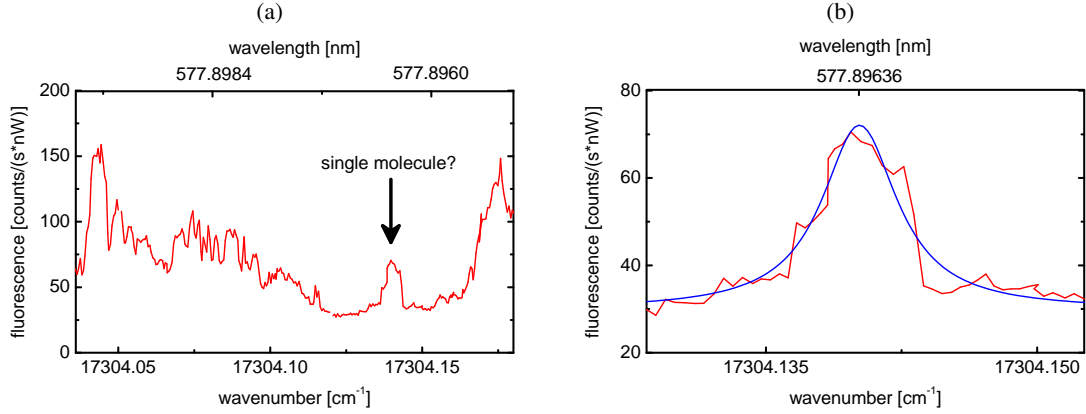


Figure 6.7: (a) shows the fluorescence excitation spectra of a small area on the high frequency side of site X_4 in crystal #1 (cf. fig. 6.5(a)) with a laser scan speed of 1 MHz/s, an integration time of 10 s and normalized to an excitation power of 1 nW of transmitted power prior to adhering the crystal. The arrow marks a possible candidate for a single molecule. (b) shows a magnification of the small peak fitted with a Lorentzian resulting with a FWHM linewidth of $5.1(4) \times 10^{-3} \text{ cm}^{-1}$ (153(3) MHz).

resolution of 10 MHz. All fluorescence peaks with a FWHM appropriate for a single molecule in a crystal matrix at low temperatures (up to a few hundred MHz) have to be considered as possible candidates for single molecules. If they are separated from other peaks, the linewidth can be determined by fitting a Lorentzian. Fig. 6.7(b) shows a magnification of the single peak in fig. 6.7(a) with the same resolution. It is fitted with a Lorentzian and the FWHM linewidth is $5.1(4) \times 10^{-3} \text{ cm}^{-1}$ or 153(3) MHz.

As discussed in sec. 3.1.4, the homogeneous linewidth of a single molecule strongly depends on the temperature. When it is lowered to cryogenic temperatures, the phonon coupling between molecule and host matrix is strongly reduced. Below 2.2 K, the linewidth of terrylene in p-terphenyl can be almost lifetime-limited with a predicted value of around $\Delta\nu_0 = 42 \text{ MHz}$ [101]. Kummer et al. have performed measurements on terrylene in p-terphenyl at various temperatures and found values between 30 MHz to 55 MHz for the low temperature limit [42]. In this work, measurements were conducted at a temperature of 4.4 K, which leads to an increase in the molecule's linewidth. To calculate the linewidth of terrylene molecules in p-terphenyl at arbitrary temperatures, eqn. 3.31 has to be considered. The dephasing-dependent lifetime $T_2^*(T)$ can be calculated via the pure phase relaxation time $T_2^*(\infty)$ and eqn. 3.32. For 4 K, T_2^* has been determined from the linewidth of a single molecule in a rather large sublimation crystal as 2.3(2) ns [67] and with an activation energy of $E_a = 17(2) \text{ cm}^{-1}$ [42] it yields $T_2^*(\infty) = 5(3) \text{ ps}$. By inserting eqn. 3.30 and eqn. 3.32 into eqn. 3.31 the temperature dependent linewidth is given by:

$$\Delta\nu(T) = \Delta\nu_0 + \frac{1}{\pi T_2^*(\infty)} \cdot \exp \left[-\frac{E_a}{k_B T} \right] \quad (6.1)$$

Therewith, the expected linewidth for terrylene in p-terphenyl at 4.4 K is $\Delta\nu = 291(5) \text{ MHz}$.

This value can only be a rough estimation, since the dephasing-dependent lifetime $T_2^*(4\text{ K})$ taken from literature and used to calculate $T_2^*(\infty)$ and $\Delta\nu(T)$ depends on the specific sample used for the measurement. E. g. a crystal with smaller dephasing would lead to a smaller linewidth.

The value determined from the fluorescence excitation spectrum for the shown peak is only half as large as the calculated theoretical value for the linewidth of terrylene at 4.4 K and therefore a strong indication for a single terrylene molecule.

Fluorescence intensity autocorrelation

After localizing promising isolated fluorescence peaks which exhibit a FWHM linewidth that is compatible with a single molecule, a measurement of the fluorescence intensity autocorrelation was performed. The optical setup was reconfigured for the use of the two SPCMs instead of the spectrometer by simply replugging the optical fiber (cf. fig. 4.1). To minimize detection of stray light from external light sources and of the excitation light from the laser, a 650 nm short pass and a 630 nm long pass filter were used in the optical setup. To carry out a correlation measurement, the laser wavelength was set to the previously determined position of a possible single molecule and the photon emission was recorded for up to an hour. In the Hanbury-Brown Twiss setup, the photon beam is divided by a 50/50 beamsplitter and led to the two SPCMs, where the arrival times are recorded [117].

In order to verify the antibunching behavior of a single molecule candidate, the fluorescence intensity correlation function is investigated for short times τ . The antibunching for a terrylene molecule with the expected linewidth should take place on a timescale of nanoseconds. In fig. 6.8 the correlation function $g^{(2)}(\tau)$ is plotted against the separation time τ for short times up to ± 100 ns with a resolution of 1 ns. The excitation wavelength was 577.5634 nm with a power of 9.6 nW. The power was low enough to not cause power broadening (cf. sec. 6.2.3). The data shows a clear antibunching dip at $\tau = 0$, which proves that the investigated signal stems from a single molecule. Due to the low excitation power, no Rabi oscillations can be observed. The normalization has been carried out with the countrate at long times. Around the antibunching, $g^{(2)}$ is slightly higher than unity as a consequence of the photon bunching from the triplet state. This leads to a decay of the autocorrelation function corresponding to the lifetime of the triplet state. The drawn line is the result of a fit of eqn. 3.45. The argument of the exponential consists of the fluorescence rate $k_{21} = 1/T_1$ and the dephasing contribution $\Gamma_2 = 1/T_2 = 1/2T_1 + 1/T_2^*$. While k_{21} is independent of the temperature, T_2^* becomes large only for very low temperatures of about 2 K, at which the dephasing is dominated by the fluorescence rate. Since the experiments in this work have been carried out at a temperature of 4.4 K, pure dephasing cannot be neglected. To determine the pure dephasing time T_2^* for a slightly different sample temperature of 4.4 K, eqn. 3.32 has to be solved. For 4 K, T_2^* has been determined experimentally from the linewidth of a single molecule as 2.3(2) ns [67]. With an activation energy of $E_a = 17(2)\text{ cm}^{-1}$ [42] it yields $T_2^*(\infty) = 5(3)\text{ ps}$. With this value, the expected pure dephasing time for the temperature in the experiment is calculated as

$$T_{2,\text{theor.}}^*(4.4\text{ K}) = 1.3(8)\text{ ns} \quad (6.2)$$

By setting the lifetime of the excited state to the experimentally determined value of $T_1 = 3.7(2)\text{ ns}$ by S. Kummer [67], the fit of the autocorrelation function in fig. 6.8 with eqn. 3.45

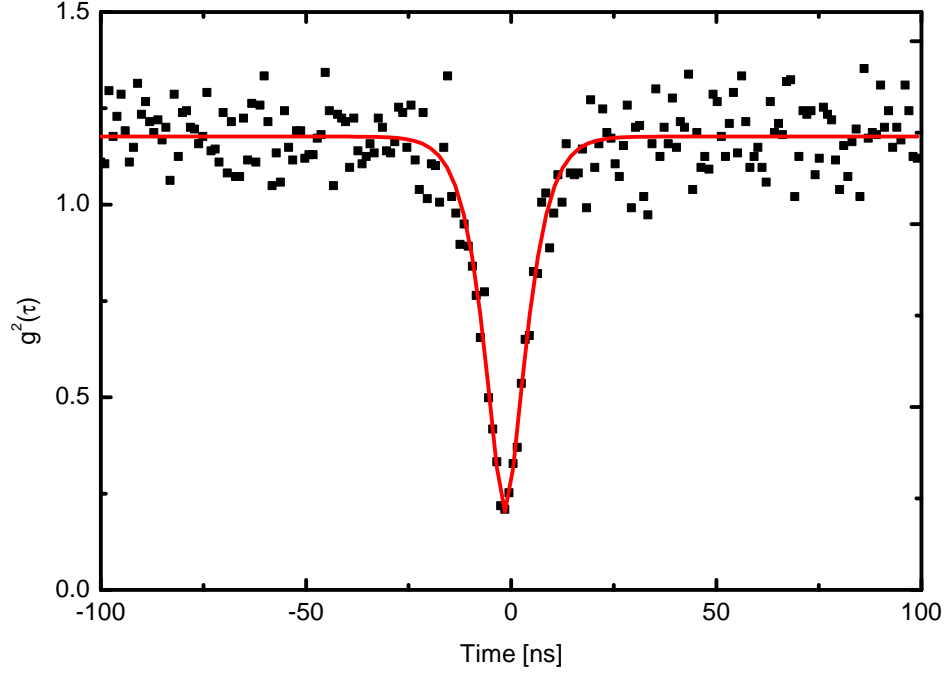


Figure 6.8: Normalized fluorescence intensity autocorrelation function $g^{(2)}(\tau)$ at short times for a single terrylene molecule in p-terphenyl (crystal #3, spectral position 577.5634 nm). The red line is a fit of eqn. 3.45. For details see text.

reveals for the pure dephasing time for this molecule $T_2^*(4.4 \text{ K}) = 5(4) \text{ ns}$. This is round about four times higher than the expected value. The higher the pure dephasing time T_2^* is, the smaller is the dephasing contribution to the homogeneous linewidth, thus leading to a smaller broadening of the homogeneous linewidth. With eqn. 3.31, the fluorescence rate T_1 , and the determined pure dephasing time T_2^* , the homogeneous linewidth for this molecule can be calculated as $\Delta\nu(4.4 \text{ K}) = 102(45) \text{ MHz}$.

For this molecule the linewidth was also determined from a fluorescence excitation measurement yielding 184(17) MHz. This value and the linewidths $\Delta\nu$ of other molecules from crystal #1 to #3 investigated in this work can be seen in tab. 6.2. The linewidths have been determined from autocorrelation measurements and/or spectrally from a fluorescence excitation measurement from the peak width. Due to some reasons like spectral stability (cf. the next section) or relatively high scan speeds, the linewidths determined spectrally have the tendency to be larger than the ones determined from the $g^{(2)}$ measurement.

The three crystal samples show a large variation for the linewidths of the embedded molecules between 35 MHz and 394 MHz. Crystal #2 shows the largest linewidth for terrylene, even larger than the theoretical expected 291 MHz. It is remarkable that all other linewidths in crystal #1 and #3 are smaller than this theoretical value. Some molecules in crystal #3 even reach the lifetime-limited value, expected below 2.2 K. A possible reason for linewidths smaller than

molecule	577.8966 nm, #1	577.8510 nm, #2	577.5634 nm, #3	577.4252 nm, #3	577.5410 nm, #3	577.5702 nm, #3
T_2^* (ns)	–	0.9(7)	5(4)	–	–	–
$\Delta\nu$ (from $g^{(2)}$) (MHz)	–	394(255)	102(45)	35(2)	43(2)	44(2)
$\Delta\nu$ (spectrally) (MHz)	153(3)	366(18)	184(17)	142(12)	181(52)	113(23)

Table 6.2: Summary and overview of the properties of some single terrylene molecules (denoted with spectral position and crystal #) found in crystal #1 to #3.

expected for this temperature could be the extraordinary small crystal samples, which have been manufactured and used in this work. The Bridgman crystals used by Kummer et al. had thicknesses between a few hundred μm and 5 mm [42]. The crystals used here have lateral dimension far less than 1 μm (cf. sec. 5.2.3). According to the Debye model, the phonon density in a solid is directly proportional to the volume. A smaller volume leads to less atoms, thus less vibrational states. This results in less phonon states and, therefore, less dephasing for the embedded terrylene molecules might occur.

For two molecules, the pure dephasing time T_2^* could be determined from the autocorrelation measurement as well (cf. tab. 6.2). To determine the pure dephasing time from the autocorrelation function, the argument of the exponential in eqn. 3.45 is solved for the parameter obtained from the fit of the autocorrelation function to the experimental data. Here, for most molecules the lifetime of the excited state $T_1 = 1/k_{21}$ is already close to the lifetime-limited value. Thus, the pure dephasing time cannot be extracted from the argument of the exponential. In such cases eqn. 3.46 is used.

Spectral stability

At low cryogenic temperatures, crystals like p-terphenyl have stable and well-defined structures. Since the ZPL of embedded terrylene molecule is extremely narrow at such temperatures, it is highly sensitive to changes in the molecular environment or external perturbations. As a result, the intensity, the width, and the position of the molecule's ZPL can be affected. Not only is the spectral position of the molecule the most sensitive feature of the ZPL, it is also the most crucial one when it comes to a continuous investigation of the molecule's characteristics. The magnitude of interactions between environment and molecule that already lead to a measurable lineshift is rather small: From Stark effect measurements, it is known that an external electric field leads to a shift of the ZPL of a molecule. E. g., for some terrylene molecules in a polymer, it has been observed that a field of 50 kV/m results in a shift of 50 MHz of the ZPL [118]. For the small dimensions of an organic dye molecule, such a field would correspond to an electron moving by 0.1 nm at a distance of 10 nm [47].

Small amounts of crystal defects like dislocations, vacancies or grain boundaries are present

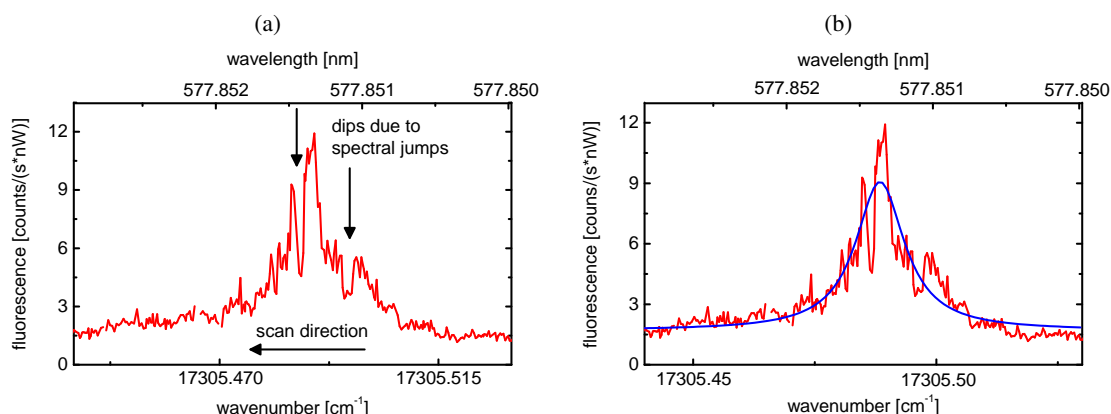


Figure 6.9: Fluorescence excitation measurement of a single terrylene molecule in p-terphenyl (crystal #2, spectral position 577.8510 nm) showing spectral jumps during the scan. The resolution is 10 MHz and the fluorescence signal is normalized to an excitation power of 1 nW. In (a) the resulting dips are marked. In (b) the line is fitted with a Lorentzian resulting in a FWHM linewidth of $1.22(6) \times 10^{-2} \text{ cm}^{-1}$ (366(18) MHz). For details see text.

in every crystal, leading to inhomogeneous broadening, as described before (cf. sec. 3.1.4). But these defects are static at low temperatures and thus contribute only to the static distribution of the ZPLs around the center frequency. Crystal defects can also have a dynamic effect, leading to reversible or irreversible spectral jumps of the ZPL [119]. This could be the case for misarrangements in the molecular packing near a defect which would create additional space and allow for molecular motion.

Such spectral jumps in the molecular frequency due to crystal defects have been also observed for p-terphenyl crystals. Usually, the most stable molecules were found near the center of an inhomogeneous line, with an increase of unstable molecules in the wings [6, 56]. Reversible jumps are for example the photo-induced jumps of molecules in site XY (cf. sec. 3.3.2). Such molecules as well as molecules with irreversible jumps have not been investigated in this work. It has been observed, that during the thermalization process of the sample due to cooling to cryogenic temperatures, spectral instabilities can also occur [120]. Such an instability would become more stable with time as the sample reaches the thermal equilibrium. The molecules in this work were at cryogenic temperatures for months, enough time for a proper thermalization. Although measurements were performed with low excitation energies and the buffergas should ensure a proper heat transfer, a possible heating of the sample due to laser irradiation cannot be completely ruled out.

The investigation of the intramolecular characteristics like fluorescence rate or triplet transitions require a spectrally stable molecule, which allows for an extensive observation over a long time. When a molecule performs a spectral jump during an excitation measurement, the fluorescence signal shows discontinuities. Such a measurement can be seen in fig. 6.9(a). It shows a continuous fluorescence excitation scan with a slow speed of 1 MHz/s. Since the data was acquired with the spectrometer and an integration time of 10 s, the resulting resolution is 10 MHz.

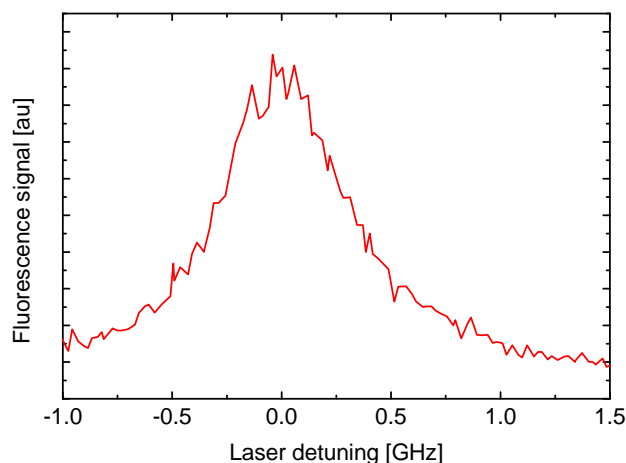


Figure 6.10: Individual fluorescence excitation scan of the molecule at spectral position 577.8436 nm in crystal #3 with a resolution of 25 MHz and an excitation power of approx. 2 nW. For details see text.

Every time the molecule jumps off the frequency of the excitation laser, the signal exhibits a dip in the emitted fluorescence, marked by two arrows. Since the integration time is long compared to triplet transitions, times of no photon emission clearly correspond to spectral diffusion and not to photon bunching. Depending on the spectral position of the jump, a broadening of the single molecule line in the fluorescence excitation may be observed, e. g., if the new jump position is within the linewidth of the molecule. This only weakly influences – if at all – the spectrum of the molecule investigated here: a fit with a Lorentzian reveals a FWHM linewidth of 366(18) MHz (cf. fig. 6.7(b)), which is close to the expected linewidth of 291 MHz for 4.4 K.

In order to find a molecule with a high spectral stability, a fast scan with approx. 250 MHz/s was performed in the spectral region in which the spectral jumps were expected to take place. The individual scans are then compared to see any change in the center frequency. The excitation wavelength was continuously scanned over the molecule's resonance from one side to another and the emitted fluorescence was collected with a SPCM. One typical individual scan can be seen in fig. 6.10. To compare the spectra of the individual scans with each other, they are fitted to Lorentzians. The spectral stability for two different molecules of crystal #3 can be seen in fig. 6.11. Both measurements were performed at different excitation powers, thus allowing not to draw conclusions on the linewidth of the investigated molecule. While the molecule in fig. 6.11(a) is stable at the initial position of 577.8436 nm for more than 25 min, the molecule in fig. 6.11(b) shows fluctuations of about 1 GHz around the initial position of 578.557 nm. Both molecules are located in sites X_4 and X_2 , resp. These sites are known to be stable (cf. sec. 3.3.2) and the spectral distance from the center of the inhomogeneous band is approx. 0.06 nm for both molecules.

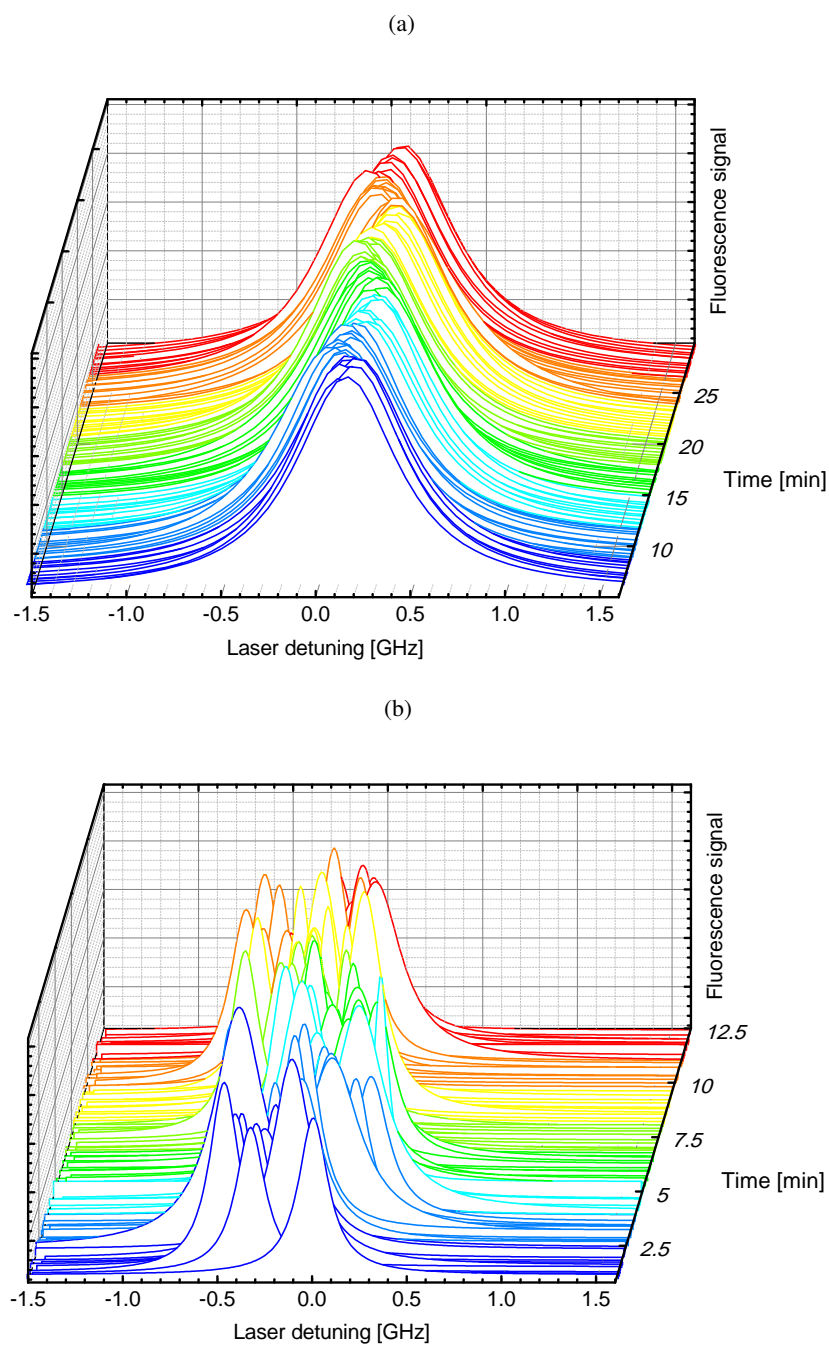


Figure 6.11: Spectral stability of two different molecules. A successive scan with a resolution of 25 MHz and a power of approx. 2 nW and 1 nW, respectively is performed for several minutes. The spectra are fitted with Lorentzians for better visibility and 0 GHz detuning is set for the first spectral position. **(a)** shows a relatively stable molecule (spectral position 577.8436 nm, crystal #3) and **(b)** an unstable molecule (spectral position 578.5570 nm, crystal #3). For details see text.

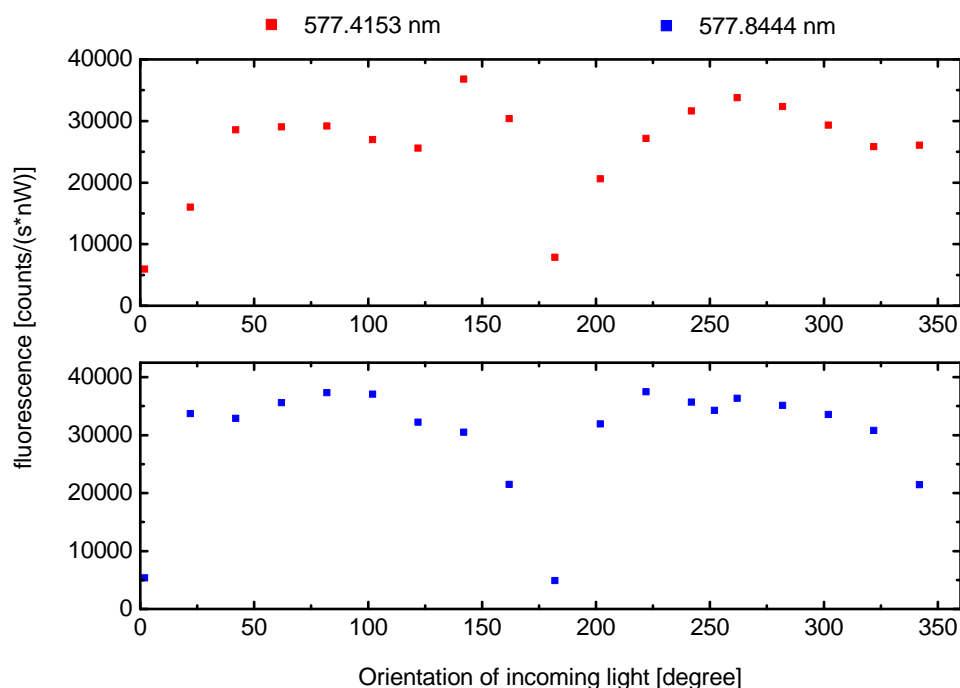


Figure 6.12: Normalized fluorescence intensity for two different molecules in crystal #3 as a function of the polarization of the exciting light coupled into the optical nanofiber with respect to the horizontal plane. For details see text.

Polarization measurements

Unlike other host materials for single molecule spectroscopy like polymers or Shpol'skii matrices, crystals have the advantage of offering a highly ordered surrounding for the guest molecule. Only specific orientations are possible for an embedded dopant. In sec. 3.3.2, these possible orientations have been discussed extensively. The probability for the absorption of light depends strongly on the orientation of the molecule's transition dipole moment and thus, since the latter is parallel to a certain axis of the molecule, on the orientation of the molecule within the crystal with respect to the excitation light.

In this work linearly polarized light was used to excite the molecular samples via a non-polarization-maintaining optical fiber. For the interpretation of the molecule's characteristics in dependence of the excitation power, each molecule's orientation has to be known. To determine the orientations of the single terrylene molecules investigated in this work with respect to the polarization of the laser light coupled into the optical fiber, the intensity of the emitted fluorescence has been measured with a SPCM for different angles of the incident linearly polarized light. The angle of polarization was set with the polarizer before the glass plate in the optical setup (cf. fig. 4.1), with the definition that 0° is perfectly linear horizontal polarization and 90° is perfectly linear perpendicular polarization. For the molecules with the spectral position 577.4153 nm and 577.8444 nm, the results can be seen in fig. 6.12.

Like for the two molecules here, all investigated molecules in crystal #3 show the same drop in the emitted fluorescence for a polarization of 2° and 182° . From this it can be concluded, that the orientation of all terrylene molecules in this crystal is the same. The contrast between the minimum and the maximum is approx. 6 to 7 and the modulation of the fluorescence intensity of both molecules shows a similar phase and amplitude. There is no polarization angle for which the fluorescence signal vanishes completely, suggesting that the polarization of the excitation light at the location of each molecule is not linear. Non-polarization-maintaining fiber was used for the TOF and the connection from/to the optical setup. Even properly taped to the experiment table and guided on a metal rail to the cryostat, small disturbances like bending or temperature fluctuations (inside the cryostat) can cause birefringence within the optical fiber, leading to crosstalk between the two possible polarization modes. As a direct result, the polarization of the light is not purely linear anymore. But even if birefringence was induced here, it was constant for every molecule in time, since the minimum of fluorescence is located explicitly at a specific angle for all terrylene molecules in crystal #3. The constant position of the minimum also shows, that the position of the crystal on the TOF was stable in time.

6.2.2 Autocorrelation measurements

Besides giving evidence that the emitted fluorescence originates from a single molecule, $g^{(2)}$ measurements also allow to extract further intramolecular information. For short times, $g^{(2)}(\tau)$ gives information on the antibunching, the fluorescence rate k_{21} , the dephasing $1/T_2$ and the Rabi oscillations. Longer times hold information about the long-lived triplet state. A combined correlation measurement for short and long times for the molecule with the spectral position at 577.4252 nm in crystal #3 and an excitation power of 7.7 nW can be seen in fig. 6.13. It covers over 7 orders of magnitude in time and the three characteristic features in the emitted fluorescence of a single molecule can be seen (cf. sec. 3.2.3): antibunching for times shorter than 5 ns, followed by Rabi oscillations up to 50 ns and the decay of the correlation function due to the decay of the triplet state. Here, the excitation power is set to a rather high value to ensure the clear visibility of all these three features. Short- and long-time autocorrelation measurements will be discussed separately in general and with regard to the influence of the excitation power below.

Short times

In fig. 6.14, the correlation rates $N(\tau)$ of the correlation measurements for the molecule at the spectral position of 577.5702 nm in crystal #3, performed for different excitation powers between 4.7 nW and 37.7 nW, a linear input polarization of 2° for the excitation light and up to delays of ± 50 ns are shown. Here, the results are not normalized to show the clear increase of the correlation rate with increasing excitation power. Note that the antibunching dip is not exactly centered at $\tau = 0$ due to a time delay in the signal transmission between one SPCM and the FPGA. The excitation power has a clear effect on the steepness of the antibunching dip and on the existence of Rabi oscillations near the antibunching dip. Rabi oscillations are caused by the laser-driven motion between the ground state S_0 and the excited state S_1 . The subsequent damping is due to energy and phase relaxation processes. An increase in the excitation power

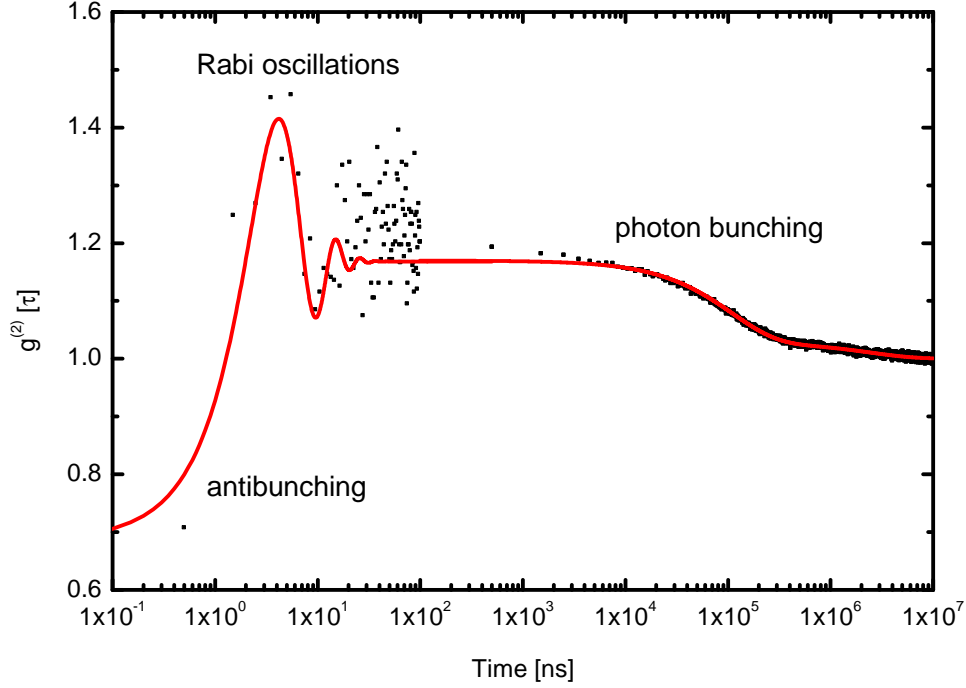


Figure 6.13: Normalized fluorescence intensity autocorrelation function $g^{(2)}(\tau)$ for a single terrylene molecule in p-terphenyl (crystal #3, spectral position 577.4552 nm) measured over 7 orders of magnitude in time. The red line is a fit with eqn. 3.45 and eqn. 3.47. For details see text.

has several effects: the higher the power, the more pronounced are the Rabi oscillations. At the same time, more stray light occurs, resulting in a worsening of the contrast¹. According to eqn. 3.33, the linewidth increases with increasing power and, since the width of the antibunching dip is inversely proportional to the linewidth (cf. eqn. 3.46), the dips width decreases with increasing excitation power.

By determining the Rabi frequency Ω from the autocorrelation function as a function of the excitation intensity for a single molecule, the saturation intensity I_S can be calculated. For three different molecules in crystal #3, the function $g^{(2)}(\tau)$ is determined for short times and the Rabi frequency is calculated for each excitation intensity, according to eqn. 3.45. The excitation power is converted to the excitation intensity according to the parameters of the TOF and the field distribution for linear polarization, cf. sec. 2.1.1. This intensity is only valid for molecules directly on the fiber surface. Since the exact distance between molecule and fiber is unknown, lower intensities can be expected at the exact position of the molecule. The resulting dependence of the square of the Rabi frequency on the intensity is plotted in fig. 6.15 and linear fits according to eqn. 3.37 are applied. Then, the slope corresponds to $\Gamma_2^2/(2I_S)$. It can be seen that, with an increasing excitation intensity, the square of the Rabi frequency Ω^2 grows linearly for each

¹Here, the contrast is defined as the relative depth of the antibunching dip.

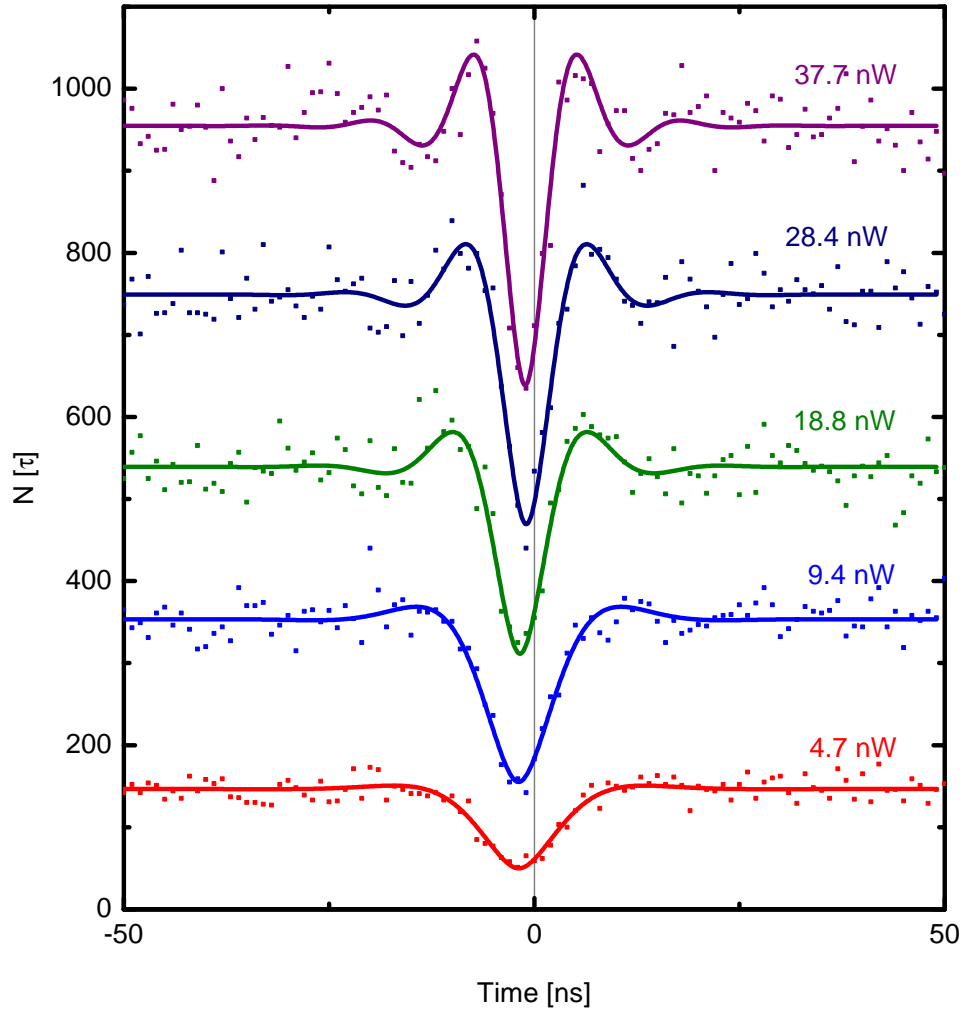


Figure 6.14: $N(\tau)$ at short times for a single terrylene molecule (spectral position 577.5702 nm, crystal #3) for different excitation powers. The lines are fits of eqn. 3.45. For details see text.

molecule. Although all molecules are located in crystal #3 and in the vicinity of site X_4 , the increase of the Rabi frequency differs strongly for every molecule. From the linear fit, the saturation intensity can be extracted. The dephasing rate Γ_2 is simplified to k_{21} and can be extracted from the fit of the correlation function as well. An overview of the obtained results is given in tab. 6.3. The values for the temperature independent fluorescence rate k_{21} are similar for all three molecules and also comparable to the value obtained by S. Kummer for terrylene in p-terphenyl with $k_{21} = 0.28 \text{ ns}^{-1}$ [67]. The saturation intensity has also been calculated by S. Kummer via the measured transition rates k_{21} , k_{23} and k_{31} and varies between 81 mW/cm^2 and 94 mW/cm^2 for a polarization of the excitation light parallel to the molecular dipole and a

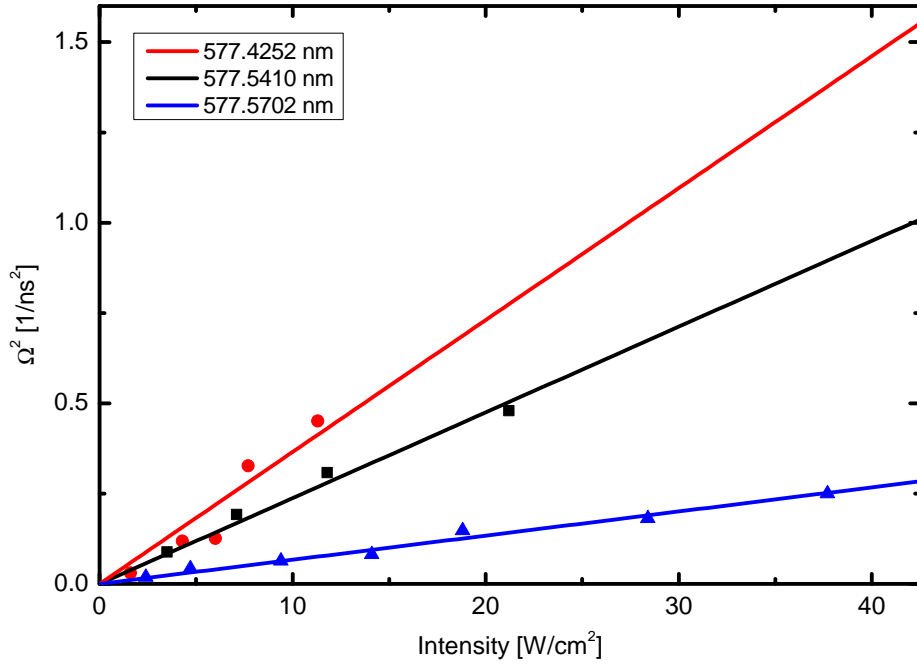


Figure 6.15: Dependence of the square of the Rabi frequency on the intensity for three different molecules in crystal #3. From the linear fit, the saturation intensity can be determined according to eqn. 3.37. For details see text.

	577.4252 nm	577.5410 nm	577.5702 nm
molecule			
k_{21} [ns ⁻¹]	0.22(1)	0.27(1)	0.27(1)
I_S [W/cm ²]	0.66(7)	1.57(7)	5.6(2)
polarization	92°	42°	2°

Table 6.3: Saturation intensities for three different molecules in crystal #3 determined from the data in fig. 6.15 with the help of eqn. 3.37. The fluorescence rates k_{21} have been determined from the fit of eqn. 3.46 to the data of the correlation measurement. The polarization gives the angle between the horizontal plane and the linear polarization of the light. For details see text.

temperature of 1.4 K. Since the saturation intensity of a single terrylene molecule in p-terphenyl is indirectly dependent on the temperature T via the dephasing rate $1/T_2 = 1/2T_1 + 1/T_2^*$ (cf. eqn. 3.34), the expected saturation intensity for 4.4 K has to be determined. To calculate the expected saturation intensity at 4.4 K, eqn. 3.34 has to be used with the dephasing time

$T_2(4.4 \text{ K})$. With the previously determined expected pure dephasing time of $T_{2,\text{theor.}}^*(4.4 \text{ K}) = 1.3 \text{ ns}$ (cf. eqn. 6.2) and the experimentally determined temperature independent fluorescence rate of $T_1 = 3.7(2) \text{ ns}$ [67], the saturation intensity can be calculated as

$$I_S(4.4 \text{ K}) = I_S(1.4 \text{ K}) \cdot \frac{1/T_1 + 1/T_2^*(4.4 \text{ K})}{1/T_1 + 1/T_2^*(1.4 \text{ K})} \approx 3.8 \cdot I_S(1.4 \text{ K}) \quad (6.3)$$

Thus, the expected saturation intensity at 4.4 K is approx. 3.8 times higher than at 1.4 K and therefore between 0.23 W/cm^2 and 0.27 W/cm^2 . The saturation intensities calculated here are varying between 0.66 W/cm^2 and 5.6 W/cm^2 , but were determined with different polarizations of the excitation light. Here, the excitation intensity on the fiber surface is calculated for linear polarization and contains all three field components $|E|^2 = |E_r|^2 + |E_\phi|^2 + |E_z|^2$ of the fundamental mode HE_{11} (cf. sec. 2.1.1). For a molecule with a transition dipole perpendicular to the fiber surface, the maximum coupling to the field is achieved when all field components are maximal. Nevertheless, the longitudinal component does not couple to the molecular dipole. For the fiber diameters and excitation wavelength used here, this reduces the excitation intensity by 23.4 % directly on the fiber surface for the molecule with the maximum coupling to $I_S = 0.51 \text{ W/cm}^2$ (577.4252 nm (polarization 92°)). This saturation intensity is directly comparable with the temperature-adapted values by S. Kummer. The molecule at the spectral position 577.5702 nm is measured with a light polarization perpendicular to the transition dipole moment and the molecule at the spectral position 577.5410 nm with a light polarization approx. between perpendicular and parallel orientation of the dipole. Taking into account the contrast of approx. 6 to 7 between parallel and perpendicular orientation, a rough estimation for the saturation intensity of these two molecules can be given. The saturation intensity reduces to approx. 0.9 W/cm^2 for the molecule at 577.5702 nm and approx. 0.5 W/cm^2 for the molecule at 577.5410 nm. All determined saturation intensities are higher than corresponding temperature-adapted values from literature. A fact, which has not been taken into account is the distance of the molecule from the surface of the TOF. The intensities here refer to a position directly on the surface. Even if small monocrystals of lateral dimensions with a few hundred nm and a thickness of a few ten nm are used, this would reduce the intensity at the position of the molecule up to 20 % (cf. sec. 2.1.3).

Long times

In order to investigate the behavior of the correlation function for long delays, an evaluation of the counted photon events has been performed for values of τ up to a few ms and the bi-exponential eqn. 3.47

$$g^{(2)}(\tau) = 1 + C_1 \exp(-\lambda_1 \tau) + C_2 \exp(-\lambda_2 \tau)$$

has been fitted to the results. In fig. 6.16, the correlation function $g^{(2)}$ is plotted against τ for long times up to 10 ms with a resolution of 1 ns. The decay of the autocorrelation function due to photon bunching is clearly visible. The fit reveals decay times of $\lambda_1 = 159(1) \mu\text{s}$ and $\lambda_2 = 2721(26) \mu\text{s}$ and contrasts of $C_1 = 0.08$ and $C_2 = 0.03$. Similar values were obtained by M. Białkowska for terrylene in p-terphenyl at 5 K with $\lambda_1 = 490 \mu\text{s}$, $\lambda_2 = 3075 \mu\text{s}$, $C_1 = 0.1$ and $C_2 = 0.05$ [69].

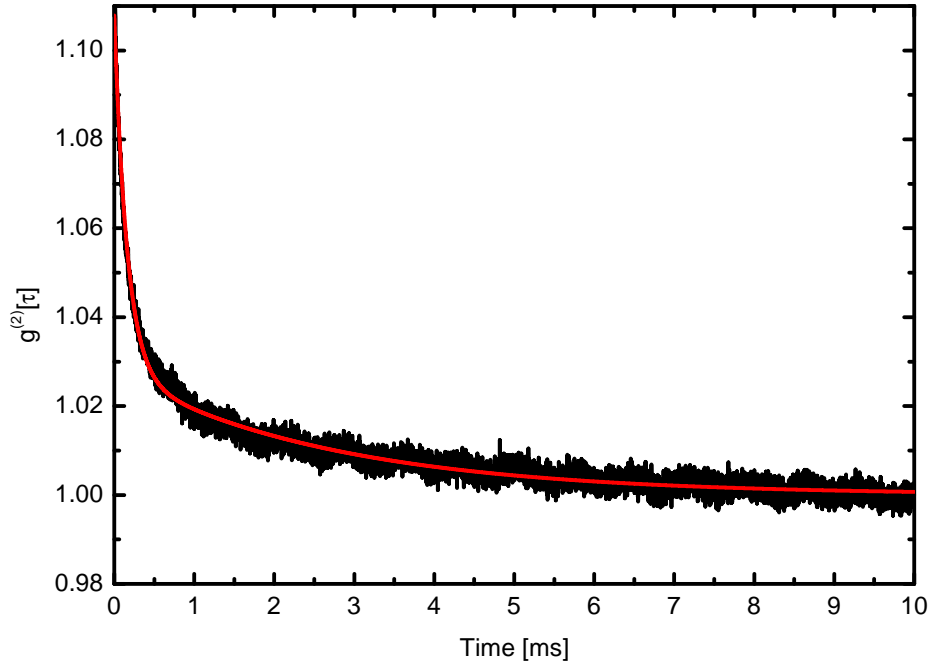


Figure 6.16: Decay of the normalized fluorescence intensity autocorrelation function $g^{(2)}(\tau)$ for a single terrylene molecule (spectral position 577.4252 nm, crystal #3) for an excitation power of 7.9 nW. The red line is a fit of eqn. 3.47. For details see text.

A set of long time autocorrelation measurements was performed for different molecules and for different excitation powers. This should allow to determine the ISC rates k_{31} and k_{23} but, as already observed by S. Kummer, the decay rates λ show a rather high scatter [87]. In our measurement, no conclusive results could therefore be obtained for the ISC rates.

6.2.3 Further saturation measurements

An increase of the excitation power has several effects on a molecule as discussed in sec. 3.1.4. In a previous section, the saturation intensity I_S has been already determined via the Rabi-frequency which were extracted from the autocorrelation functions for different excitation powers. Another possibility is to measure the increase of the fluorescence emission rate R . It is also dependent on the excitation intensity according to eqn. 3.38. To this end, fluorescence excitation measurements of a single molecule were repeated for different excitation intensities and the emitted fluorescence was collected with an SPCM. The excitation wavelength is scanned with a speed of 450 MHz/s a few GHz over the resonance frequency of the molecule. The resulting countrates of these scans are fitted with Lorentzians and are shown in fig. 6.17. As the excitation power increases, a clear increase in the peak width and in the emitted fluorescence can be observed. From the fitted Lorentzians, the fluorescence emission rate R and linewidth

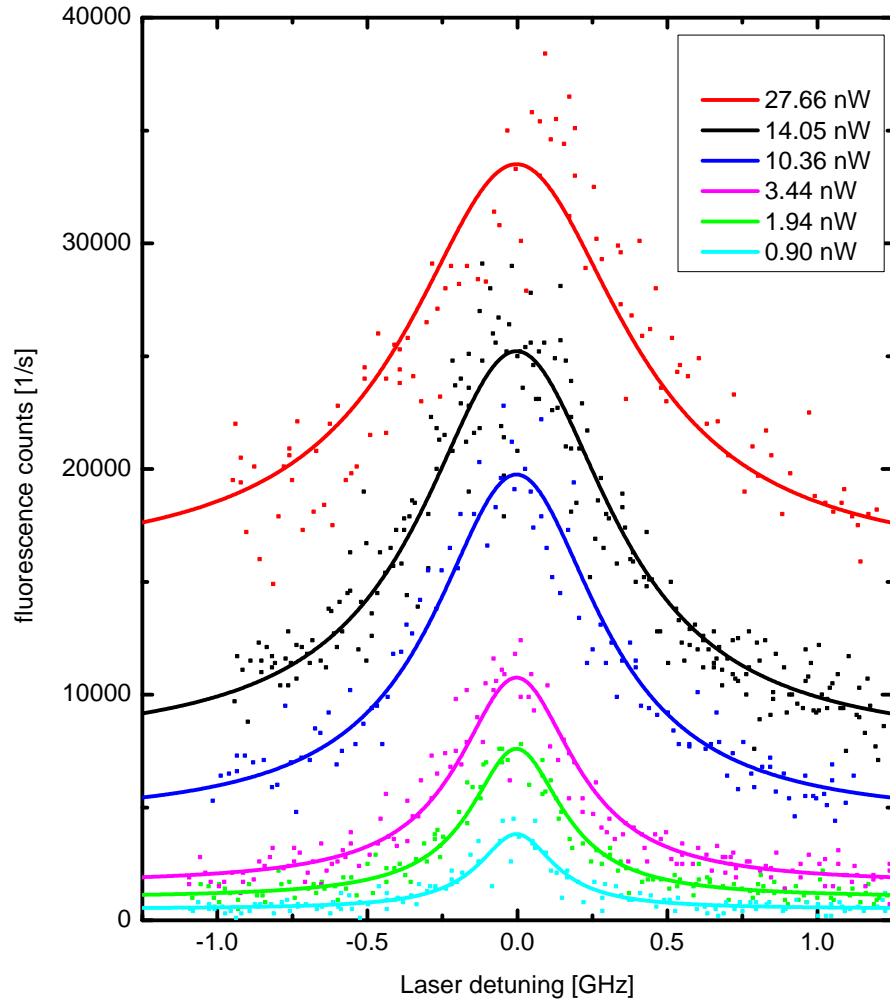


Figure 6.17: Fluorescence excitation measurement for different excitation powers for a single terrylene molecule (spectral position 577.8444 nm, crystal #3). The resolution is approx. 4.5 MHz and the data is fitted with Lorentzians. For details see text.

can be obtained for different excitation intensities I . For three different terrylene molecules in crystal #3, the resulting emission rate $R(I)$ is plotted in fig. 6.18(a). The solid lines are fits of eqn. 3.38 and show that the functional form of the theory is reproduced well by the saturation data. The values obtained from the fit are listed in tab. 6.4. For two of the molecules (spectral positions 577.5410 nm and 577.5702 nm), the saturation intensity has been determined earlier via the Rabi-frequency of the autocorrelation measurement (cf. tab. 6.3). The resulting saturation intensities from the different ways of determination are compatible within the errors, but a few times higher than the lowest ones determined by S. Kummer [103]. All in all, the ex-

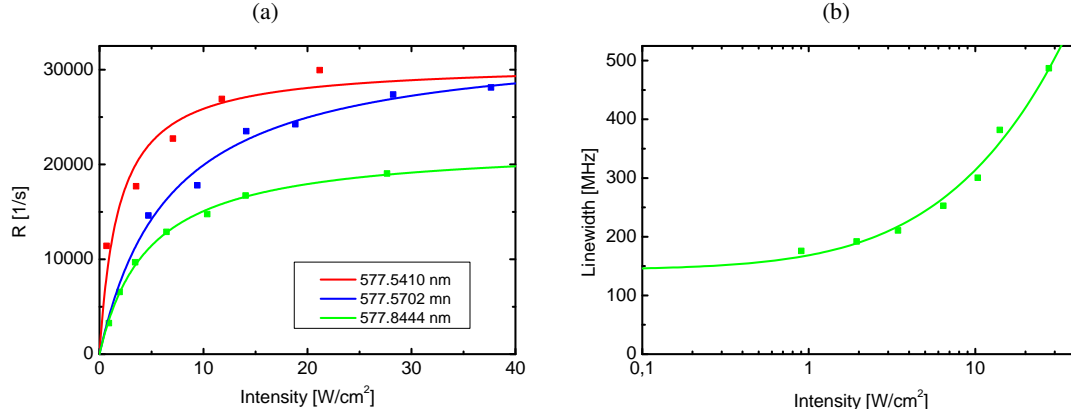


Figure 6.18: Saturation behavior of single terrylene molecules in p-terphenyl in crystal #3. **(a)** Fluorescence emission rate R of three molecules with the shown spectral position. **(b)** Fluorescence excitation linewidth for the molecule at the spectral position 577.8444 nm. Both quantities are plotted as a function of the laser intensity. The solid lines are fits with eqn. 3.38 and eqn. 3.33, respectively. For details see text.

molecule (spectral position [nm])	577.8444	577.5410	577.5702
I_S [W/cm²]	4.7(3)	1.9(8)	6.7(10)
R_∞ [1/s]	22 122(423)	30 680(2863)	33 359(1582)

Table 6.4: Resulting saturation intensities I_S and fully saturated emission rate R_∞ for three different molecules in crystal #3 via eqn. 3.38 determined from linewidth measurements for different excitation powers. For details see text.

perimental values of the saturation intensity which was determined here for different molecules in the same crystal sample, show a large scatter up to a factor of 10. According to eqn. 3.34, the saturation intensity depends strongly on k_{21} , the ISC rates k_{23} and k_{31} and the projection of the molecule's dipole moment along the electric field of the excitation light μ_{21} . Since the determined values for k_{21} show only a slight variation for the different molecules (cf. tab. 6.3), one possible reason for the strong variation of the saturation intensity has to lie in the ISC rates. The molecules' orientation can be ruled out, as measurements of the polarization dependence of different molecules in crystal #3 showed (cf. sec. 6.2.1). Another possibility can be different distances between the fiber surface and the molecules: the higher the distance, the lower is the intensity at the position of the molecule and thus, the higher the saturation intensity.

The linewidth (FWHM) for different excitation powers has been extracted from the fluorescence excitation measurement and is plotted in fig. 6.18(b) for the molecule at 577.8444 nm. A fit has been applied according to eqn. 3.33. At low excitation energies the linewidth reaches

143(12) MHz, a value approx. three times higher than the lifetime-limited value. The saturation intensity resulting from the fit is $2.6(6) \text{ W/cm}^2$, round about half of the value determined via the fluorescence emission rate.

Summary and Outlook

In this thesis, single molecule spectroscopy (SMS) was realized by optically interfacing dye molecules via the nanofiber waist of a tapered optical fiber (TOF). The molecules were embedded in a crystalline host and different methods to manufacture small dye-doped organic monocrystals were investigated. Since the crystals are coupled to the evanescent field at the surface of the nanofiber, it is imperative to keep their size well below the wavelength of the nanofiber-guided light in order to conserve the light-guiding abilities of a TOF. After a crystal of suitable size was manufactured and deposited on a TOF, the sample was cooled down to a temperature of 4.4 K. At this temperature, single molecules within the crystal were spectrally addressed and investigated for their characteristics. The pronounced evanescent field surrounding the nanofiber waist of a TOF then allows one to efficiently couple the guided light and the dopant molecules.

These studies were carried out with terrylene-dye molecules embedded in a p-terphenyl crystal, a well-known organic system with a high quantum yield. The use of a crystal introduces a highly ordered environment for the embedded molecules, leading to a high photostability. Due to crystal defects, the local environment of each molecule is slightly different, thereby causing inhomogeneous broadening of their transition frequencies and, in particular, of their zero-phonon lines (ZPL). This allows one to spectrally address individual molecules out of the ensemble. When the crystals were deposited or grown on the TOF, their excitation through the fiber allowed the observation of emitted fluorescence and transmitted power.

In terms of fluorescence signal and power transmittance through the fiber, the most successful method was to grow the crystals from an oversaturated solution. In this case, use of a precipitation agent speeded up the crystallization process, leading to crystals of different sizes. The smallest achievable sizes were approx. 380 nm in diameter. These crystals could be deposited on a TOF. Images of these nanocrystals on a substrate, taken with a scanning electron microscope (SEM) showed their monocrystalline character. Their small size enabled transmitted powers up to 46.3 %.

To further investigate the spectral characteristics of the doped crystal samples and to localize single terrylene molecules, the TOF with the deposited crystal had to be cooled down to cryogenic temperatures in a liquid helium bath cryostat. Thereby, the number of phonon transi-

tions is highly reduced and the ZPLs are ideally lifetime-limited. In total, three suitable crystal samples were cooled down and investigated at a temperature of 4.4 K. I performed fluorescence spectroscopy of the dopant molecular ensemble and could identify the vibronic peaks belonging to specific vibronic transitions of terrylene in p-terphenyl.

I performed fluorescence excitation measurements for two of the crystal samples. The corresponding spectra revealed a strong inhomogeneous broadening. To verify that the observed sharp fluorescence lines belong to single molecules, I determined the fluorescence intensity autocorrelation function. Clear antibunching was visible for the investigated spectral lines, thereby proving the observation of single molecules. In total, more than ten single terrylene molecules were identified in the crystal samples and some of them were used for further measurements of their spectral characteristics. I determined the linewidth of these molecules, spectrally and from the correlation measurements. Linewidths between 35 MHz and 394 MHz could be found. A comparison with the theoretically expected width of 291 MHz for the temperature of 4.4 K revealed that most linewidths were much narrower than expected. In particular, some were already comparable to lifetime-limited values. Due to the small size of the manufactured nanocrystals, the phonon density is reduced, possibly leading to a small dephasing and a narrow linewidth.

I also examined the spectral stability of the molecules - an important characteristic if one wants to perform measurements with one molecule for a long time period. While some molecules showed spectral instabilities, others offered stable spectral positions for the full time of continuous excitation of 25 min.

In addition to offering a highly ordered surrounding for the embedded molecules the host crystal should also force them to have a specific orientation. In order to check this assumption and to gain information on the orientations of the molecules within the crystal, I performed measurements of the emitted fluorescence in dependence of the polarization of the excitation light. Several measurements on different molecules in the same crystal revealed, that the long axis of all terrylene molecules in this crystal indeed had the same orientation.

Finally, the measurement of the fluorescence intensity autocorrelation function also provides further intramolecular information. Besides the antibunching-dip for $\tau = 0$, due to the coherent excitation with a laser, Rabi oscillations can be observed. Moreover, the triplet state of the molecules leads to a clear photon bunching on longer time scales. By measuring the increase in the Rabi frequency in dependence of the excitation intensity, the saturation intensity for several molecules was determined. For a polarization of maximum excitation, a saturation intensity of 0.51 W/cm^2 was determined. This is two times higher than the expected value for this temperature. However, this intensity was calculated at the fiber surface. The unknown distance between molecule and surface might therefore at least partially explain the deviation.

In summary, the spectral characteristics of the molecules in our nanocrystals is similar to other samples known from literature. One remarkable difference is the narrow linewidth for some molecules, which is already close to the lifetime-limited value, even though at 4.4 K.

Future measurements of the linewidth for higher temperatures would show, below which temperature the lifetime-limited value is reached. It would also conclude to what extent the crystal size and the reduced phonon density are related to the reduced linewidth of the molecules at 4.4 K. Since the transmission properties of the TOF could be granted by using nanocrystals, absorption measurements of single molecules would also be possible and would enlarge the

capabilities of SMS with a TOF. Our nanofiber-coupled dye-doped nanocrystals might be useful as a building block for future quantum information systems. Along this line, the next step would be to turn the system into a triggered photon source. By coupling a single molecule within the crystal to the mode of a fiber Bragg grating resonator, efficient single photon emission into the cavity could be triggered by the excitation with a ps laser pulse. An external electric field would allow one to tune the molecule in resonance with the resonator via the Stark effect. Since the shift of the linewidth due to the Stark effect is different for every molecule in a crystal, it should be possible to shift two molecules in resonance with each other and the fiber Bragg grating resonator. Their mutual excitation would be highly increased in the strong-coupling regime.

Light propagation in optical fibers

The reason for the light guiding abilities of optical fibers can be found in the total internal reflection of the light at the boundary layer from core to cladding, where the refractive index shows an abrupt jump for step-index fibers. Because the size of the core is of the same order as the wavelength of the transmitted light, the theory of ray optics is not sufficient for the description of the propagating light and the wave equations have to be taken into account. The derivation presented here is mainly oriented on [121], but other detailed derivations of the light guiding properties of standard optical glass fibers can be found elsewhere in literature [122–124]. For calculating the field distribution within a step-index fiber, Maxwell equations for an isotropic, charge and current-free medium have to be solved:

$$\nabla \times \mathbf{H} = \varepsilon \frac{\partial \mathbf{E}}{\partial t} \quad (\text{A.1})$$

$$\nabla \times \mathbf{E} = -\mu \frac{\partial \mathbf{H}}{\partial t} \quad (\text{A.2})$$

$$\nabla \cdot (\varepsilon \mathbf{E}) = 0 \quad (\text{A.3})$$

$$\nabla \cdot (\mu \mathbf{H}) = 0 \quad (\text{A.4})$$

where \mathbf{E} and \mathbf{H} denote the electric respectively magnetic field, ∇ is the nabla operator, t is the time and $\varepsilon = \varepsilon_0 \varepsilon_r$ is the permittivity. It is composed of the vacuum permittivity ε_0 and the material dependent relative permittivity ε_r . Similarly, the magnetic permeability $\mu = \mu_0 \mu_r$ describes the influence of the material on the magnetic field. In a diamagnetic solid, the relative permeability μ_r can be assumed to be almost equal to the vacuum permeability μ_0 . Solutions describing an electromagnetic wave with a propagation direction along the z -axis of the fiber take the following form:

$$\begin{bmatrix} \mathbf{E}(\mathbf{r}, t) \\ \mathbf{H}(\mathbf{r}, t) \end{bmatrix} = \begin{bmatrix} \mathbf{E}(r, \phi) \\ \mathbf{H}(r, \phi) \end{bmatrix} \exp[i(\omega t - \beta z)] \quad (\text{A.5})$$

where β denotes the propagation constant along the fiber and $\omega = 2\pi f$ the angular frequency with the frequency of the light field f . The use of cylindrical coordinates comes naturally due

to the geometry of the fiber. Taking the curl of eqn. A.2 and substituting eqn. A.1 in leads to

$$\nabla^2 \mathbf{E} - \mu\epsilon \frac{\partial^2 \mathbf{E}}{\partial t^2} = -\nabla \left(\frac{\mathbf{E}}{\epsilon} \cdot \nabla \epsilon \right) \quad (\text{A.6})$$

∇^2 denotes the delta operator. With eqn. A.3 and considering only real parts of \mathbf{E} , this leads to

$$\nabla^2 \mathbf{E} + k^2(\mathbf{r})\mathbf{E} = 0 \quad (\text{A.7})$$

Here, $k = \omega n/c_0$ is the wavenumber of the propagating field in the medium with the refractive index n and $c_0 = 1/\sqrt{\epsilon_0\mu_0}$ is the vacuum speed of light. Although the wave equation is rather complicated for cylindrical components, the z-components of the electric and magnetic field remain simple:

$$(\nabla^2 + k^2) \begin{Bmatrix} E_z \\ H_z \end{Bmatrix} = 0 \quad (\text{A.8})$$

By means of the Maxwell equations, solutions for E_r , E_ϕ , H_r and H_ϕ can be deduced from the solutions of E_z and H_z . Thereto, eqn. A.5 is inserted into eqn. A.8, leading to the Helmholtz equation for E_z and H_z in cylindrical coordinates:

$$\left(\frac{\partial^2}{\partial r^2} + \frac{1}{r} \frac{\partial}{\partial r} + \frac{1}{r^2} \frac{\partial^2}{\partial \phi^2} + (k^2 + \beta^2) \right) \begin{Bmatrix} E_z \\ H_z \end{Bmatrix} = 0 \quad (\text{A.9})$$

This equation is separable into angular and radial components and is reduced with the ansatz

$$\begin{Bmatrix} E_z \\ H_z \end{Bmatrix} = \psi(r) \exp(\pm il\phi) \quad (\text{A.10})$$

to a Bessel differential equation:

$$\left[\frac{\partial^2}{\partial r^2} + \frac{1}{r} \frac{\partial}{\partial r} + \left(k^2 - \beta^2 - \frac{l^2}{r^2} \right) \right] \begin{Bmatrix} E_z \\ H_z \end{Bmatrix} = 0 \quad (\text{A.11})$$

The solutions for the Bessel equation are linear combinations of Bessel functions of the order $l = 0, 1, 2, 3, \dots$. If Bessel functions with only imaginary variables are allowed as solutions as well, thus considering positive and negative signs for $(k^2 - \beta^2)$, possible solutions are:

$$(k^2 - \beta^2) > 0 : \begin{Bmatrix} E_z \\ H_z \end{Bmatrix} = c_1 J_l(hr) + c_2 Y_l(hr) \quad (\text{A.12})$$

$$(k^2 - \beta^2) < 0 : \begin{Bmatrix} E_z \\ H_z \end{Bmatrix} = c_1 I_l(qr) + c_2 K_l(qr) \quad (\text{A.13})$$

These set of solutions represents the radial dependency of the fields E_z and H_z . Here, c_1 and c_2 are constants depending on the boundary conditions and $h^2 = k^2 - \beta^2$ and $q^2 = \beta^2 - k^2$. The Bessel functions of first and second kind are represented by J_l and Y_l , respectively, while I_l and K_l represent the modified Bessel functions of first and second kind, respectively. The Bessel functions are plotted in fig. A.1.

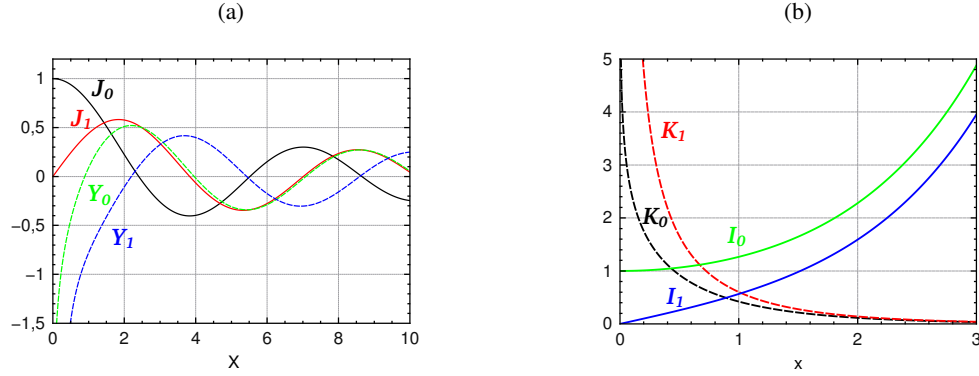


Figure A.1: Plot of (a) Bessel functions of first and second kind and (b) modified Bessel functions of first and second kind.

In an optical glass fiber, the light field is guided by the core and decays rapidly within the cladding so that no power loss via radiation is possible. This transversal confinement requires the propagation constant to be between the one in the cladding and the one in the core:

$$n_{\text{core}}k_0 > \beta > n_{\text{cladding}}k_0 \quad (\text{A.14})$$

As this ensures that the wave is evanescent in the cladding, in the solution (eqn. A.13) c_1 must be zero. Thus for a confined mode the fields in the cladding are:

$\mathbf{r} > \mathbf{a}$:

$$E_z(\mathbf{r}, t) = CK_l(qr) \exp[i(\omega t + l\phi - \beta z)] \quad (\text{A.15})$$

$$H_z(\mathbf{r}, t) = DK_l(qr) \exp[i(\omega t + l\phi - \beta z)] \quad (\text{A.16})$$

with two arbitrary constants C and D , where

$$q^2 = \beta^2 - n_2^2 k_0^2 > 0 \quad (\text{A.17})$$

with $k_0 = \omega/c_0$ and $n_{\text{cladding}} = n_2$. Inside the core the field has to stay finite as $r \rightarrow 0$. Additionally, at $r = a$ the tangential components of the fields \mathbf{E} and \mathbf{H} inside the core have to match the ones inside the cladding. As evident from fig. A.1, this means in eqn. A.12, $c_2 = 0$. Hence the fields inside the core are:

$\mathbf{r} < \mathbf{a}$:

$$E_z(\mathbf{r}, t) = AJ_l(hr) \exp[i(\omega t + l\phi - \beta z)] \quad (\text{A.18})$$

$$H_z(\mathbf{r}, t) = BJ_l(hr) \exp[i(\omega t + l\phi - \beta z)] \quad (\text{A.19})$$

where A and B are two arbitrary constants with

$$h^2 = n_1^2 k_0^2 - \beta^2 > 0 \quad (\text{A.20})$$

where $n_1 = n_{\text{core}}$. With these solutions for the z-components of the fields of core and cladding, the other field components E_r , E_ϕ , H_r and H_ϕ can be determined using eqn. A.1 and A.2. These components and a more detailed way of calculating them can be found in [121] and will not be given here. The continuity of the tangential parts of the field vectors \mathbf{E} and \mathbf{H} at the interface between core and cladding $r = a$ leads to a eigenvalue equation that determines β :

$$\left(\frac{J'_l(ha)}{haJ_l(ha)} + \frac{K'_l(qa)}{qaK_l(qa)} \right) \left(\frac{n_1^2 J'_l(ha)}{haJ_l(ha)} + \frac{n_2^2 K'_l(qa)}{qaK_l(qa)} \right) = \left(\frac{l\beta}{k_0} \right)^2 \left[\left(\frac{1}{ha} \right)^2 + \left(\frac{1}{qa} \right)^2 \right]^2 \quad (\text{A.21})$$

Here, $J'_l(ha) = dJ_l(ha)/d(ha)$ and $K'_l(qa) = dK_l(qa)/d(qa)$ denote the derivative with respect to their arguments ha and qa . By taking into account ha and qa , for every k_0 and each value of l , a set of discrete solutions for the propagation constant β_{lm} (with $m = 1, 2, 3 \dots$) can be found numerically. Therefore, the propagation constant is representing all possible propagating modes within the fiber. The eqn. A.21 is quadratic in $J'_l(ha)/haJ_l(ha)$ and can be separated:

$$\begin{aligned} \frac{J'_l(ha)}{haJ_l(ha)} = & - \left(\frac{n_1^2 + n_2^2}{2n_1^2} \right) \frac{K'_l(qa)}{qaK_l(qa)} \\ & \pm \sqrt{\left(\frac{n_1^2 - n_2^2}{2n_1^2} \right)^2 \left(\frac{K'_l(qa)}{qaK_l(qa)} \right)^2 + \frac{l^2}{n_1^2} \left(\frac{\beta}{k_0} \right)^2 \left(\frac{1}{q^2 a^2} + \frac{1}{h^2 a^2} \right)^2} \quad (\text{A.22}) \end{aligned}$$

In generally, the solutions of the this equation correspond to two sets of modes, which are named EH and HE modes. These are so-called hybrid modes, because they exhibit non-vanishing parts for E_z and H_z . While for the EH modes E_z is larger than H_z , for HE modes it is the other way round. Since E_z and H_z are non-vanishing for both families of modes, these modes have to be imagined as skew rays propagating helical in the fiber. At each reflection of such a helical ray, both polarizations are mixed, resulting in hybrid modes with non-vanishing E_z and H_z . The solutions for the equation above can be obtained by using the relations between the Bessel functions [125] which leads to:

$$\textbf{EH modes:} \quad \frac{J_{l+1}(ha)}{haJ_l(ha)} = \frac{n_1^2 + n_2^2}{2n_1^2} \frac{K'_l(qa)}{qaK_l(qa)} + \left(\frac{l}{(ha)^2} - R \right) \quad (\text{A.23})$$

$$\textbf{HE modes:} \quad \frac{J_{l-1}(ha)}{haJ_l(ha)} = - \left(\frac{n_1^2 + n_2^2}{2n_1^2} \right) \frac{K'_l(qa)}{qaK_l(qa)} + \left(\frac{l}{(ha)^2} - R \right) \quad (\text{A.24})$$

with the abbreviation

$$R = \sqrt{\left(\frac{n_1^2 - n_2^2}{2n_1^2} \right)^2 \left(\frac{K'_l(qa)}{qaK_l(qa)} \right)^2 + \left(\frac{l\beta}{n_1 k_0} \right)^2 \left(\frac{1}{q^2 a^2} + \frac{1}{h^2 a^2} \right)^2} \quad (\text{A.25})$$

For every propagation constant β_{lm} , depending on the combination of the indices l and m , two modes exist. In the special case $l = 0$, according to eqn. A.15 to A.19, the fields are independent of the angular variable ϕ . That means $\partial/\partial\phi = 0$ and the field components are radially symmetric leaving E_r , E_z and H_ϕ as the non-vanishing field components for the EH_{0m} modes (with $l = 0$

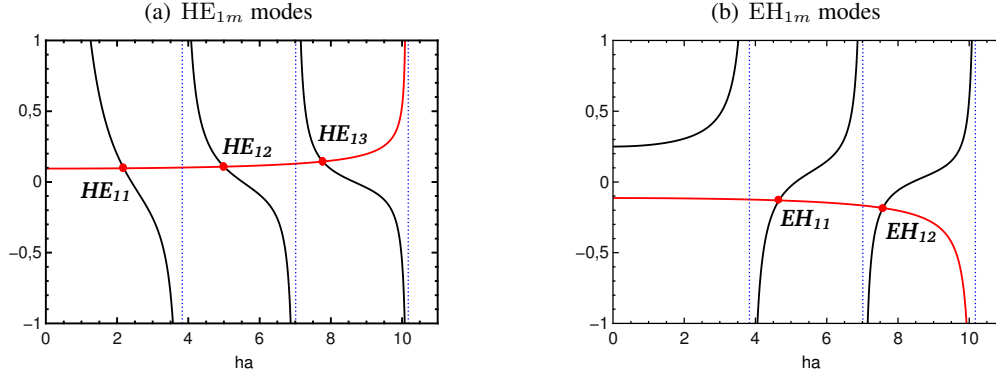


Figure A.2: Graphical solution for (a) HE and (b) EH modes. The black graph is the left and the red graph the right side of the according equation respectively. The intersection marked with red dots are the solutions for the according modes. The dotted lines correspond to the cut-off frequencies of each mode.

and $m = 0, 1, 2, 3, \dots$). Since only the magnetic component is perpendicular to the propagation direction z , and in z -direction, only electric components exist, these modes are designated as transversal magnetic modes TM_{0m} . The other way round can be found for HE_{0m} modes (with $l = 0$ and $m = 0, 1, 2, 3, \dots$): the non-vanishing components are H_r , H_z and E_ϕ . Here, only the electric component is perpendicular to the propagation direction z , while in z -direction, only magnetic components exist. Thus, these modes are designated as transversal electric modes TE_{0m} . As both TM and TE modes, have to preserve their vanishing z -component at every reflection, they have to pass the fiber axis and can be imagined as meridional rays [123]. Since the possible solutions in eqn. A.23 and A.24 are transcendental, to find the propagation constants for the different modes, a graphical or numerical solution can be used. It is useful to express the equations solely in terms of ha :

$$qa = \sqrt{V^2 - (ha)^2} \quad (A.26)$$

The normalized frequency V is a fundamental parameter describing the system:

$$V = k_0 a \sqrt{n_1^2 - n_2^2} = k_0 a \text{NA} \quad (A.27)$$

It considers the properties of a step-index fiber (refractive indices n_1 and n_2 and the core radius a) for each wave number k_0 . The normalized frequency gives information about the number of modes guided by the fiber. NA denominates the numerical aperture of the glass fiber and characterizes the angle of the conical light field leaving the fiber core.

In fig. A.2, the graphical solutions for the EH- and HE-modes are implemented by plotting the left and the right side of eqn. A.23 and A.24 in dependence of ha . Clearly visible are the intersections marked with red points, where both sides of an equation have the same value, representing the solutions of the equation. By taking eqn. A.20, extending it with a^2 , the propagation constant β_{lm} can be directly calculated:

$$\beta_{lm} = \sqrt{n_1^2 k_0^2 - \frac{h^2 a^2}{a^2}} \quad (A.28)$$

with l labeling the mode number and m counting the solution with increasing ha and a specified value for V and thus characterizing the modes, which are named accordingly. Since the left side of each equation diverges at $V = ha$, the normalized frequency V commits the number of modes propagating in a fiber. The vertical asymptotes arise from the roots of the Bessel function J_1 . They denote the lower limit for the normalized frequency V , for which the according mode can exist. This lower limit is called the cut-off frequency V_c . It is important to note, that for arbitrary small values of V , an intersection for the HE_{11} mode always exists. Therefore, HE_{11} is the fundamental mode without a cut-off frequency, it is present for each fiber configuration. This allows to define the single-mode condition for a fiber, where only the fundamental mode can be guided by the fiber. Calculating the roots of the Bessel functions J_0 for the TE and TM modes gives a value of $ha = 2.405$. According to the graphical solution shown here, it can be demonstrated that below this value no TE or TM mode exists. Therefore, making $V < 2.405$ the single-mode condition, where only the fundamental mode HE_{11} is guided.

As mentioned before, the propagation constant β serves as a characteristic of the propagating mode inside a cylindrical waveguide. The effective refractive index can be written in terms of β as

$$n_{\text{eff}} = \frac{\beta}{k_0} \quad (\text{A.29})$$

where k_0 is related to the normalized frequency V , according to eqn. A.27. With eqn. A.14 it applies:

$$n_{\text{core}} > n_{\text{eff}} > n_{\text{cladding}} \quad (\text{A.30})$$

In fig. A.3 n_{eff} is plotted as a function of V for the lowest modes of a step-index optical fiber. It can be seen, that for every mode it applies $n_{\text{eff}}(V_c) = \frac{\beta}{k_0} = n_{\text{cladding}}$. The reason for this is, that by approaching the cut-off frequency V_c the light field spreads out more and more into the cladding. For $n \rightarrow n_{\text{cladding}}$ the confinement of the modes to the core becomes smaller and the main part of the energy propagates within the cladding. The reverse situation can be found for normalized frequencies far away from cut-off $V \gg V_c$: the modes are more and more confined to the core leading to $n \rightarrow n_{\text{core}}$.

A.1 Linearly polarized modes

Although the solutions of the characteristic equation A.21 are exact for arbitrary configurations of step-index fibers and wavelengths, solving is difficult for HE- and EH-modes where all six field components are nonzero. Since the refractive indices of core and cladding are very similar

$$n_{\text{core}}/n_{\text{cladding}} \approx 1 \quad (\text{A.31})$$

eqn. A.21 is reduced to new linear characteristic equation

$$h \frac{J_{l-1}(ha)}{J_l(ha)} = -q \frac{K_{l-1}(qa)}{K_l(qa)} \quad (\text{A.32})$$

The resulting modes are simplified in a way, that the transversal field is mainly polarized in one direction, thus introducing linear polarized modes, which are called LP-modes [126]. Solving the characteristic equation for LP-modes A.32 leads again to the propagation constant β_{lm} .

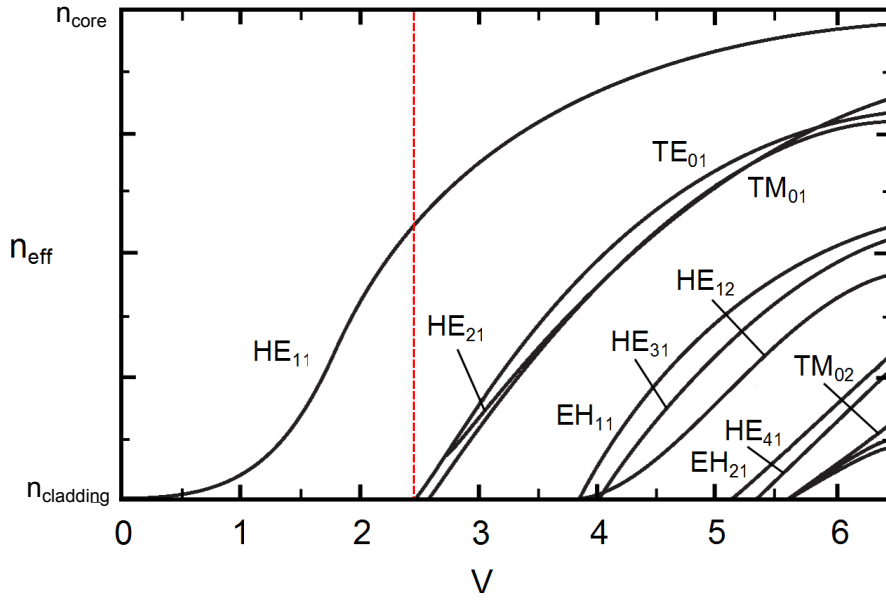


Figure A.3: $n_{\text{eff}}(V)$ for some modes of lower order, adopted from [121]. The red dashed line assigns $V_c = 2,405$, the single mode condition, below only the fundamental mode HE_{11} can propagate.

For the borderline case $n_{\text{core}} \rightarrow n_{\text{cladding}}$ the propagation constant is the same for the modes $\text{HE}_{l+1,m}$ and $\text{EH}_{l-1,m}$, the modes are degenerated and commonly expressed via the LP-modes. The former mode of lowest order HE_{11} has now the propagation constant β_{01} and is named LP_{01} -mode.

Bibliography

- [1] H. J. Kimble, “The quantum internet,” *Nature*, vol. 453, pp. 1023–1030, 2008.
- [2] G. Binning, H. Rohrer, C. Gerber, and E. Weibel, “Surface Studies by Scanning Tunneling Microscopy,” *Phys. Rev. Lett.*, vol. 49, no. 1, pp. 57–61, 1982.
- [3] G. Binning and C. F. Quate, “Atomic Force Microscope,” *Phys. Rev. Lett.*, vol. 56, no. 9, pp. 930–933, 1986.
- [4] W. Itano, J. Bergquist, and D. Wineland, “Laser Spectroscopy of Trapped Atomic Ions,” *Science*, vol. 237, pp. 612–617, 1987.
- [5] W. E. Moerner and L. Kador, “Finding a single molecule in a haystack: Optical detection and spectroscopy of single absorbers in solids,” *Anal. Chem.*, vol. 64, pp. A1217–A1223, 1989.
- [6] M. Orrit and J. Bernard, “Single Pentacene Molecules Detected by Fluorescence Excitation in a p-Terphenyl Crystal,” *Phys. Rev. Lett.*, vol. 65, no. 21, pp. 2716–2719, 1990.
- [7] T. Plakhotnik, E. A. Donley, and U. P. Wild, “Single-Molecule Spectroscopy,” *Annu. Rev. Phys. Chem.*, vol. 48, pp. 181–212, 1997.
- [8] J. Hwang and E. A. Hinds, “Dye molecules as single-photon sources and large nonlinearities on a chip,” *New J. Phys.*, vol. 13, p. 085009, 2011.
- [9] F. Kulzer, R. Matzke, C. Bräuchle, and T. Basché, “Nonphotochemical Hole burning Investigated at the Single-Molecule Level: Stark Effect Measurements on the Original and Photoproduct State,” *J. Phys. Chem. A*, vol. 103, pp. 2408–2411, 1999.
- [10] S. Nie, D. Chiu, and R. Zare, “Probing Individual Molecules with Confocal Fluorescence Microscopy,” *Science*, vol. 266, pp. 1018–1021, 1994.
- [11] W. E. Moerner, E. J. G. Peterman, S. Brasselet, S. Kummer, and R. M. Dickson, “Optical Methods for Exploring Dynamics of Single Copies of Green Fluorescent Protein,” *Cytometry*, vol. 36, pp. 232–238, 1999.
- [12] W. Ambrose, P. Goodwin, and J. Nolan, “Single-Molecule Detection With Total Internal Reflection Excitation: Comparing Signal-To-Background and Total Signals in Different Geometries,” *Cytometry*, vol. 36, pp. 241–231, 1999.

- [13] E. Betzig and R. Chichester, "Single Molecules Observed by Near-Field Scanning Optical Microscopy," *Science*, vol. 262, pp. 1422–1425, 1993.
- [14] J. Villatoro and D. Monzón-Hernández, "Fast detection of hydrogen with nano fiber tapers coated with ultra thin palladium layers," *Opt. Express*, vol. 13, no. 13, pp. 5087–5092, 2005.
- [15] K. Q. Kieu and M. Mansuripur, "Biconical Fiber Taper Sensors," *IEEE Photonic Tech. L.*, vol. 18, no. 21, pp. 2239–2241, 2006.
- [16] Y. Tian, W. Wang, N. Wu, X. Zou, and X. Wang, "Tapered Optical Fiber Sensor for Label-Free Detection of Biomolecules," *Sensors*, vol. 11, pp. 3780–3790, 2011.
- [17] G. Sagué, E. Vetsch, W. Alt, D. Meschede, and A. Raschenbeutel, "Cold-Atom Physics Using Ultrathin Optical Fibers: Light-Induced Dipole Forces and Surface Interactions," *Phys. Rev. Lett.*, vol. 99, p. 163602, 2007.
- [18] K. P. Nayak and K. Hakuta, "Single atoms on an optical nanofibre," *New J. Phys.*, vol. 10, p. 053003, 2008.
- [19] M. J. Morrissey, K. Deasy, Y. Wu, S. Chakrabarti, and S. N. Chormaic, "Tapered optical fibers as tools for probing magneto-optical trap characteristics," *Rev. Sci. Instrum.*, vol. 80, p. 053102, 2009.
- [20] J. C. Knight, G. Cheung, F. Jacques, and T. A. Birks, "Phase-matched excitation of whispering-gallery-mode resonances by a fiber taper," *Opt. Lett.*, vol. 22, no. 15, pp. 1129–1131, 1997.
- [21] S. M. Spillane, T. J. Kippenberg, O. J. Painter, and K. J. Vahala, "Ideality in a Fiber-Taper-Coupled Microresonator System for Application to Cavity Quantum Electrodynamics," *Phys. Rev. Lett.*, vol. 91, no. 4, p. 043902, 2003.
- [22] T. A. Birks, W. J. Wadsworth, and P. S. J. Russel, "Supercontinuum generation in tapered fibers," *Opt. Lett.*, vol. 25, no. 19, pp. 1415–1417, 2000.
- [23] U. Wiedemann, K. Karapetyan, C. Dan, D. Pritzkau, W. Alt, S. Irsen, and D. Meschede, "Measurement of submicrometre diameters of tapered optical fibres using harmonic generation," *Opt. Express*, vol. 18, no. 8, pp. 7693–7704, 2010.
- [24] F. Warken, E. Vetsch, D. Meschede, M. Sokolowski, and A. Rauschenbeutel, "Ultra-sensitive surface absorption spectroscopy using sub-wavelength diameter optical fibers," *Opt. Express*, vol. 15, no. 19, pp. 11952–11958, 2007.
- [25] R. Yalla, F. Le Kien, M. Morinaga, and K. Hakuta, "Efficient Channeling of Fluorescence Photons from Single Quantum Dots into Guided Modes of Optical Nanofiber," *Phys. Rev. Lett.*, vol. 109, p. 063602, 2012.

- [26] T. Schröder, M. Fujiwara, T. Noda, H. Zhao, O. Benson, and S. Takeuchi, "A nanodiamond-tapered fiber system with high single-mode coupling efficiency," *Opt. Express*, vol. 20, no. 10, pp. 10490–10497, 2012.
- [27] J. Hwang, M. Pototschnig, R. Lettow, G. Zumofen, A. Renn, S. Götzinger, and V. Sandoghdar, "A single-molecule optical transistor," *Nature*, vol. 460, pp. 76–80, 2009.
- [28] F. Kapron, D. Keck, and R. Maurer, "Radiation losses in glass optical waveguides," *App. Phys. Lett.*, vol. 17, no. 10, pp. 423–425, 1970.
- [29] J. Edmonson, "History of the instruments for gastrointestinal endoscopy," *Gastrointest. Endosc.*, vol. 37, no. 2, pp. S27–S56, 1991.
- [30] J. Stone and C. Burrus, "Neodymium-doped silica lasers in end-pumped geometry," *App. Phys. Lett.*, vol. 23, no. 7, pp. 388–389, 1973.
- [31] J. D. Love, W. M. Henry, W. J. Stewart, R. J. Black, S. Lacroix, and F. Gonthier, "Tapered single-mode fibres and devices , Part 1: Adiabaticity criteria," *IEE Proc-J*, vol. 138, no. 5, pp. 343–354, 1991.
- [32] J. Bures and R. Ghosh, "Power density of the evanescent field in the vicinity of a tapered fiber," *J. Opt. Soc. Am. A*, vol. 16, no. 8, pp. 1992–1996, 1999.
- [33] G. Brambilla, "Optical fibre nanowires and microwires: a review," *J. Opt.*, vol. 12, pp. 043001, pp. 1–19, 2010.
- [34] F. Le Kien, J. Q. Liang, K. Hakuta, and V. I. Balykin, "Field intensity distributions and polarization orientations in a vacuum-clad subwavelength-diameter optical fiber," *Optics Comm.*, vol. 242, pp. 445–455, 2004.
- [35] A. Stiebeiner, R. Garcia-Fernandez, and A. Rauschenbeutel, "Design and optimization of broadband tapered optical fibers with a nanofiber waist," *Opt. Express*, vol. 18, pp. 22677–22685, 2010.
- [36] F. Warken, *Ultradünne Glasfasern als Werkzeug zur Kopplung von Licht und Materie*. PhD thesis, Rheinische Friedrich-Wilhelms Universität Bonn, 2007.
- [37] T. A. Birks and Y. W. Li, "The shape of fiber tapers," *Journal of lightwave technology*, vol. 10, no. 4, pp. 432–438, 1992.
- [38] M. Numrich, "Nanofaser-basierte Spektroskopie von Molekülen in organischen," Diplomarbeit, Johannes Gutenberg-Universität Mainz, 2012.
- [39] J. D. Love and W. M. Henry, "Quantifying loss minimisation in single-mode fibre tapers," *Electron. Lett.*, vol. 22, no. 17, pp. 912–914, 1986.
- [40] F. Le Kien, S. D. Gupta, V. I. Balykin, and K. Hakuta, "Spontaneous emission of a cesium atom near a nanofiber: Efficient coupling of light to guided modes," *Phys. Rev. A*, vol. 72, p. 032509, 2005.

- [41] P. Bordat and R. Brown, "Elucidation of optical switching of single guest molecules in terrylene/p-terphenyl mixed crystals," *Chem. Phys. Lett.*, vol. 331, pp. 439–445, 2000.
- [42] S. Kummer, F. Kulzer, R. Kettner, T. Basché, C. Tietz, C. Glowatz, and C. Kryschi, "Absorption, excitation, and emission spectroscopy of terrylene in p-terphenyl: Bulk measurements and single molecule studies," *J. Chem. Phys.*, vol. 107, no. 19, pp. 7673–7684, 1997.
- [43] A. Simon and R. Ulrich, "Evolution of polarization along a single-mode fiber," *App. Phys. Lett.*, vol. 31, no. 8, pp. 517–520, 1977.
- [44] E. B. Shera, N. K. Seitzinger, L. M. Davis, R. A. Keller, and S. A. Soper, "Detection of single fluorescent molecules," *Chem. Phys. Lett.*, vol. 174, no. 6, pp. 553–557, 1990.
- [45] S. Weiss, "Fluorescence Spectroscopy of Single Biomolecules," *Science*, vol. 283, pp. 1676–1683, 1999.
- [46] Andrews, David L., *Encyclopedia of Applied Spectroscopy*. VCH, 2009.
- [47] Basché, Th. and Moerner, W. E. and Orrit, M. and Wild, U. P., *Single-Molecule Optical Detection, Imaging and Spectroscopy*. VCH, 1997.
- [48] C. Kittel and H. Krömer, *Thermodynamik*. Oldenbourg, 5. ed., 2001.
- [49] F. Kulzer, *Untersuchungen zum nichtphotochemischen Lochbrennen auf Einzelmolekülebene am Modellsystem Terrylen in p-Terphenyl*. PhD thesis, Johannes Gutenberg-Universität Mainz, 2000.
- [50] Demtröder, W., *Experimentalphysik 3*. Springer Verlag, 2. ed., 2000.
- [51] M. Born and R. Oppenheimer, "Zur Quantentheorie der Molekeln.," *Annalen der Physik*, vol. 389, no. 20, pp. 457–484, 1927.
- [52] Demtröder, W., *Molekülphysik*. Oldenbourg Verlag, 2003.
- [53] C. Cohen-Tannoudji, B. Diu, and F. Laloë, *Quantenmechanik Teil 1*. de Gruyter, 2. ed., 1999.
- [54] J. Bernard, L. Fleury, H. Talon, and M. Orrit, "Photon bunching in the fluorescence from single molecules: A probe for intersystem crossing," *J. Chem. Phys.*, vol. 98, no. 2, pp. 850–859, 1993.
- [55] H. de Vries and D. A. Wiersma, "Photophysical and photochemical molecular hole burning theory," *J. Chem. Phys.*, vol. 72, no. 3, pp. 1851–1863, 1980.
- [56] W. P. Ambrose, T. Basché, and W. E. Moerner, "Detection and spectroscopy of single pentacene molecules in a p-terphenyl crystal by means of fluorescence excitation," *J. Chem. Phys.*, vol. 95, no. 10, pp. 7150–7163, 1991.

- [57] W. A. Hesselink and D. A. Wiersma, "Optical dephasing and vibronic relaxation in molecular mixed crystals: A picosecond photon echo and optical study of pentacene in naphthalene and p-terphenyl," *J. Chem. Phys.*, vol. 73, no. 2, pp. 648–663, 1980.
- [58] D. A. Steck, "Quantum and Atom Optics." <http://steck.us/teaching>. (revision 0.10.0, 3. September 2014).
- [59] A. M. Stoneham, "Shapes of Inhomogeneously Broadened Resonance Lines in Solids," *Rev. Mod. Phys.*, vol. 41, no. 1, pp. 82–108, 1969.
- [60] D. L. Orth, R. J. Mashl, and J. L. Skinner, "Optical lineshapes of impurities in crystals: a lattice model of inhomogeneous broadening by point defects," *J. Phys.: Condens. Matter*, vol. 5, pp. 2533–2544, 1993.
- [61] S. Karotke, *Stark-shift microscopy: interaction of a confined electric field with single emitters*. PhD thesis, Universität Basel, 2006.
- [62] V. Sandoghdar, J. Michaelis, C. Hettich, C. Schmitt, J. Zitzmann, and S. Kühn, "Results and Thoughts on Optical Microscopy Using a Single-molecule Probe," *Single Mol.*, vol. 4, pp. 277–281, 2001.
- [63] W. E. Moerner and T. P. Carter, "Statistical Fine Structure of Inhomogeneously Broadened Absorption Lines," *Phys. Rev. Lett.*, vol. 59, no. 23, pp. 2705–2708, 1987.
- [64] W. E. Moerner and T. Basché, "Optical Spectroscopy of Single Impurity Molecules in Solids," *Angew. Chem. Int. Ed. Engl.*, vol. 32, no. 4, pp. 457–476, 1993.
- [65] C. Gerry and P. Knight, *Introductory Quantum Optics*. Cambridge University Press, 2005.
- [66] R. Brown, J. Wrachtrup, M. Orrit, J. Bernard, and C. von Borczyskowski, "Kinetics of optically detected magnetic resonance of single molecules," *J. Chem. Phys.*, vol. 100, no. 10, pp. 7182–7191, 1994.
- [67] S. Kummer, S. Mais, and T. Basché, "Measurement of Optical Dephasing of a Single Terrylene Molecule with Nanosecond Time Resolution," *J. Phys. Chem.*, vol. 99, no. 47, pp. 17078–17081, 1995.
- [68] C. A. Hutchison and B. W. Magnum, "Paramagnetic Resonance Absorption in Naphthalene in Its Phosphorescent State," *J. Chem. Phys.*, vol. 29, pp. 952–953, 1958.
- [69] M. Białkowska, A. Makarewicz, M. Banasiewicz, and B. Kozankiewicz, "Spin-lattice relaxation and intersystem crossing in single molecules of terrylene embedded in a p-terphenyl crystal," *Chem. Phys. Lett.*, vol. 555, pp. 131–134, 2013.
- [70] B. Kozankiewicz and M. Orrit, "Single-molecule photophysics, from cryogenic to ambient conditions," *Chem. Soc. Rev.*, vol. 43, no. 4, pp. 1029–1043, 2014.
- [71] A.-M. Boiron, B. Lounis, and M. Orrit, "Single molecules of dibenzanthanthrene in n-hexadecane," *J. Chem. Phys.*, vol. 105, no. 10, pp. 3969–3974, 1996.

- [72] H. J. Kimble, M. Dagenais, and L. Mandel, "Photon Antibunching in Resonance Fluorescence," *Phys. Rev. Lett.*, vol. 39, no. 11, pp. 691–695, 1977.
- [73] T. Basché, W. E. Moerner, M. Orrit, and H. Talon, "Photon Antibunching in Fluorescence of a Single Dye Molecule Trapped in a Solid," *Phys. Rev. Lett.*, vol. 69, no. 10, pp. 1516–1519, 1992.
- [74] J. L. Richards and S. A. Rice, "Study of Impurity-Host Coupling in Shpolskii Matrices," *J. Chem. Phys.*, vol. 54, no. 5, pp. 2014–2023, 1971.
- [75] T. Basché, W. P. Ambrose, and W. E. Moerner, "Optical spectra and kinetics of single impurity molecules in a polymer: spectral diffusion and persistent spectral hole burning," *J. Opt. Soc. Am. B*, vol. 9, no. 5, pp. 829–836, 1992.
- [76] J. Tittel, R. Kettner, T. Basché, C. Bräuchle, H. Quante, and K. Müllen, "Spectral diffusion in an amorphous polymer probed by single molecule spectroscopy," *J. Lumin.*, vol. 64, pp. 1–11, 1995.
- [77] A. Müller, W. Richter, and L. Kador, "Pressure effects on single molecules of terrylene in p-terphenyl," *Chem. Phys. Lett.*, vol. 241, pp. 547–554, 1995.
- [78] C. A. Werley and W. E. Moerner, "Single-Molecule Nanoprobes Explore Defects in Spin-Grown Crystals," *J. Phys. Chem. B*, vol. 110, pp. 18939–18944, 2006.
- [79] G. S. Harms, T. Irngartinger, D. Reiss, A. Renn, and U. P. Wild, "Fluorescence lifetimes of terrylene in solid matrices," *Chem. Phys. Lett.*, vol. 313, pp. 533–538, 1999.
- [80] F. Kulzer, S. Kummer, R. Matzke, C. Bräuchle, and T. Basché, "Single-molecule optical switching of terrylene in p-terphenyl," *Nature*, vol. 387, pp. 688–691, 1997.
- [81] A. Müller, W. Richter, and L. Kador, "Persistent spectral hole burning in the few-molecule limit: terrylene in p-terphenyl," *Chem. Phys. Lett.*, vol. 285, pp. 92–98, 1998.
- [82] M. Vogel, A. Gruber, W. J., and C. von Borczykowski, "Determination of Intersystem Crossing Parameters via Observation of Quantum Jumps on Molecules," *J. Phys. Lett.*, vol. 99, pp. 14914–14917, 1995.
- [83] J. Sepioł, J. Jasny, J. Keller, and U. P. Wild, "Single molecules observed by immersion mirror objective. The orientation of terrylene molecules via the direction of its transition dipole moment," *Chem. Phys. Lett.*, vol. 273, pp. 444–448, 1997.
- [84] A. Bohnen, K.-H. Koch, W. Lüttke, and K. Müllen, "Oligorylene as a Model for "Poly(perinaphthalene)"", *Angew. Chem. Int. Ed.*, vol. 29, no. 5, pp. 525–527, 1990.
- [85] A. Drechsler, *Hochaufgelöste optische Spektroskopie einzelner Terrylen-Moleküle bei kryogenen Temperaturen mit einem Parabolspiegelmikroskop*. PhD thesis, Universität Siegen, 2002.

- [86] N. Konken, "Faserbasierte Spektroskopie von organischen Molekülen in Festkörpermatrizen bei kryogenen Temperaturen," Diplomarbeit, Johannes Gutenberg-Universität Mainz, 2010.
- [87] S. Kummer, T. Basché, and C. Bräuchle, "Terrylene in p-terphenyl: a novel single crystalline system for single molecule spectroscopy at low temperatures," *Chem. Phys. Lett.*, vol. 229, pp. 309–316, 1994.
- [88] S. Kummer, T. Basché, and C. Bräuchle, "Terrylene in p-terphenyl: a novel single crystalline system for single molecule spectroscopy at low temperatures (Erratum)," *Chem. Phys. Lett.*, vol. 232, p. 414, 1995.
- [89] R. J. Pfab, J. Zimmermann, C. Hettich, C. Gerhardt, I. Renn, and V. Sandoghdar, "Aligned terrylene molecules in a spin-coated ultrathin crystalline film of p-terphenyl," *Chem. Phys. Lett.*, vol. 387, pp. 490–495, 2004.
- [90] T. Kobayashi, "Conformational Analysis of Terphenyls by Photoelectron Spectroscopy," *Bull. Chem. Soc. Jpn.*, vol. 56, no. 11, pp. 3224–3229, 1983.
- [91] J. Baudour, "Structural Phase Transition in Polyphenyls. X. Potential Barrier Heights in Crystalline Polyphenyls and in Gaseous Biphenyl Determined Uniquely from Diffraction Data," *Acta Cryst.*, vol. B47, pp. 935–949, 1991.
- [92] H. M. Rietveld, E. N. Maslen, and C. J. B. Clews, "An X-ray and Neutron Diffraction Refinement of the Structure of p-Terphenyl," *Acta Cryst.*, vol. B26, pp. 693–706, 1970.
- [93] J. L. Baudour, Y. Delugeard, and H. Cailleau, "Transition Structurale dans les Polyphényles. I. Structure Cristalline de la Phase Basse Température du p-Terphényle à 113 K," *Acta Cryst.*, vol. B32, pp. 150–154, 1976.
- [94] P. Bordat and R. Brown, "A molecular model of p-terphenyl and its disorder-order transition," *Chem. Phys.*, vol. 246, pp. 323–334, 1999.
- [95] I. Rebane, "Difference values of spontaneous emission rate of a single-impurity molecule of pentacene in biaxial p-terphenyl crystal," *J. Lumin.*, vol. 122-123, pp. 359–361, 2007.
- [96] P. Bordat and R. Brown, "Molecular mechanisms of photo-induced spectral diffusion of single terrylene molecules in p terphenyl," *J. Chem. Phys.*, vol. 116, no. 1, pp. 229–236, 2002.
- [97] T. Pavlopoulos and P. Hammond, "Spectroscopic Studies of Some Laser Dyes," *J. Am. Chem. Soc.*, vol. 96, pp. 6568–6579, 1974.
- [98] G. Wright, "Fluorescence Excitation Spectra and Quantum Efficiencies of Organic Crystals," *Proc. Phys. Soc. B*, vol. 68, pp. 701–712, 1955.
- [99] A. Amorim da Costa and A. Amado, "Doping effects in p-terphenyl molecular crystals: a study by Raman spectroscopy," *Solid State Ionics*, vol. 125, pp. 263–269, 1999.

- [100] F. Kulzer, F. Koberling, T. Christ, and T. Basché, "Terrylene in p-terphenyl: single-molecule experiments at room temperature," *Chem. Phys.*, vol. 247, pp. 23–34, 1999.
- [101] T. Plakhotnik, W. E. Moerner, T. Irngartinger, and U. P. Wild, "Single Molecule Spectroscopy in Shpol'skii Matrices," *Chimia*, vol. 48, no. 1/2, pp. 31–31, 1994.
- [102] T. Plakhotnik, W. E. Moerner, V. Palm, and U. P. Wild, "Single molecule spectroscopy: maximum emission rate and saturation intensity," *Optics Comm.*, vol. 114, pp. 83–88, 1995.
- [103] S. Kummer, *Fluoreszenzspektroskopische Untersuchung einzelner Farbstoffmoleküle in kristallinen Festkörpern*. PhD thesis, Universität München, 1996.
- [104] Sirah Laser- und Plasmatechnik GmbH, *Datasheet Matisse DS*, 2012.
- [105] Andor, *Andor Shamrock 303i specifications*.
- [106] A. Stiebeiner, *Nanofiber-based spectroscopy of organic molecules*. PhD thesis, Johannes Gutenberg-Universität Mainz, 2014.
- [107] Excelitas Technologies, *Datasheet SPCM-AQRH*, 2014-06.
- [108] G. K. White, "Thermal expansion of reference materials: copper, silica and silicon," *Journal of Physics D*, vol. 6, pp. 2070–2078, 1973.
- [109] G. K. White, "Thermal expansion of vitreous silica at low temperatures," *Phys. Rev. Lett.*, vol. 34, no. 4, pp. 204–205, 1975.
- [110] G. K. White, "Thermal expansion of magnetic metals at low temperatures," *Proceedings of the Physical Society*, vol. 86, pp. 159–169, 1965.
- [111] J. Michaelis, *Mikroskopie mit einem einzelnen Molekül als Lichtquelle*. PhD thesis, Universität Konstanz, 2000.
- [112] W. Demtröder, *Laserspektroskopie*. Springer Verlag, 2. ed., 1991.
- [113] K. Newrkla, "Untersuchung der Auswirkung unterschiedlicher Wachstumsbedingungen bei der Herstellung Terrylen dotierter p-Terphenyl Kristalle," Bachelorarbeit, Technische Universität Wien, 2014.
- [114] A. Stiebeiner, O. Rehband, R. Garcia-Fernandez, and A. Rauschenbeutel, "Ultra-sensitive fluorescence spectroscopy of isolated surface-adsorbed molecules using an optical nanofiber," *Opt. Express*, vol. 17, no. 24, pp. 21704–21711, 2009.
- [115] A. B. Myers, P. Tchénio, M. Z. Zgierski, and W. E. Moerner, "Vibronic Spectroscopy of individual Molecules in Solids," *J. Phys. Chem.*, vol. 98, no. 41, pp. 10377–10390, 1994.
- [116] A. C. Brouwer, J. Köler, E. J. J. Groenen, and J. Schmidt, "¹³C isotope effects for pentacene in p-terphenyl: High-resolution spectroscopy and single-spin detection," *J. Chem. Phys.*, vol. 105, no. 6, pp. 2212–2222, 1996.

- [117] R. Hanbury Brown and R. Q. Twiss, “Interferometry of the Intensity Fluctuations in Light II. An Experimental Test of the Theory for Partially Coherent Light,” *Proc. R. Soc. A.*, vol. 243, no. 1234, pp. 291–319, 1958.
- [118] M. Orrit, J. Bernard, A. Zumbusch, and R. I. Personov, “Stark effect on single molecules in a polymer matrix,” *Chem. Phys. Lett.*, vol. 196, no. 6, pp. 595–600, 1992.
- [119] T. Irngartinger, A. Renn, and U. P. Wild, “Fluorescence microscopy: Spectral jumps of single molecules,” *J. Lumin.*, vol. 66&67, pp. 232–235, 1996.
- [120] V. Palm and K. Rebane, “On the role of spectral diffusion in single-molecule spectroscopy,” *J. Lumin.*, vol. 86, pp. 207–209, 2000.
- [121] A. Yariv, *Optical Electronics in Modern Communications*. Oxford University Press, 5. ed., 1997.
- [122] D. Meschede, *Optik, Licht und Laser*. Teubner Verlag, 2. ed., 2005.
- [123] W. Snyder, A. and D. Love, J. *Optical Waveguide Theory*. Chapman and Hall, 1. ed., 1983.
- [124] A. Ghatak and K. Thyagarajan, *Introduction to fiber optics*. Cambridge University Press, 1998.
- [125] Bronstein et al., *Taschenbuch der Mathematik*. Harri Deutsch Verlag, 5. ed., 2001.
- [126] D. Gloge, “Weakly guiding fibers,” *Appl. Opt.*, vol. 10, no. 10, pp. 2252–2258, 1971.

Danksagung

Zu allererst möchte ich mich bei Prof. Arno Rauschenbeutel für die Möglichkeit bedanken, in seiner Arbeitsgruppe an einem spannenden und vielseitigen Projekt arbeiten zu dürfen sowie für seine Unterstützung während der gesamten Zeit.

Viele der präsentierten Messungen und Ergebnisse wären nicht möglich gewesen ohne die Hilfe des alten und neuen Molekül-Teams: Ariane Stiebeiner und Moritz Numrich, die in der ersten Zeit in Wien dem Experiment in seiner Anfangsphase geholfen haben. Besonderer Dank gebührt Dr. Sarah Skoff für das unermüdliche Korrekturlesen meiner Arbeit. Auch im Labor hat sie zusammen mit Hardy Schaufert gerade im letzten Jahr einige neue Impulse gesetzt.

Allen Mitgliedern der Arbeitsgruppe gebührt mein Dank für ein angenehmes Arbeitsklima. Auch abseits der Physik war es angenehm mit Euch!

Bei mechanische Problemen kleiner und größerer Art, die mit dem verwendeten Kryostaten leider häufiger auftraten, waren die Mitarbeiter der mechanischen Werkstatt immer hilfsbereit und haben auch kurzfristig Arbeiten erledigt. Besonderer Dank gilt hierbei Herbert Hartmann, der nicht nur ständig optimale Ideen für technische Probleme hatte, sondern, zusammen mit Barbara Fertl auch stets die Versorgung mit kryogenen Flüssigkeiten sichergestellt hat. Bei Arbeiten im Chemielabor konnte ich mich immer auf die hilfsbereite Unterstützung von Michaela Foster verlassen.

Meiner Familie möchte ich an dieser Stelle für den Rückhalt danken, den sie mir die ganze Zeit gegeben hat.

Meiner guten Freundin Conni danke ich für so manchen Ratschlag und dafür, dass sie einfach eine Konstante in meinem Leben ist.

Nicht zuletzt möchte ich mich bei meiner Izabela bedanken, die all die Jahre immer für mich da war und mich immer wieder aufgebaut hat: Bardzo dziękuję!

LEBENS LAUF

David C. Papencordt
Juchgasse 20/24
1030 Wien
Österreich

Persönliche Daten

Geburtsdatum: 25. November 1980
Geburtsort: Wickede
Staatsangehörigkeit: deutsch

Ausbildung

seit 12/2008	Technische Universität Wien und Johannes Gutenberg-Universität Mainz Doktorand in Physik
10/2001 – 09/2008	Universität Hamburg Diplom-Physiker
08/1990 – 05/2000	Walburgis-Gymnasium, Menden
08/1986 – 06/1990	Westschule, Menden